

Water Activation in Solar-Powered Vapor Generation

Dan Wei, Chengbing Wang,* Jing Zhang, Heng Zhao, Yusuke Asakura, Miharuru Eguchi, Xingtao Xu,* and Yusuke Yamauchi*

Solar-powered vapor evaporation (SVG), based on the liquid-gas phase conversion concept using solar energy, has been given close attention as a promising technology to address the global water shortage. At molecular level, water molecules escaping from liquid water should overcome the attraction of the molecules on the liquid surface layer to evaporate. For this reason, it is better to reduce the energy required for evaporation by breaking a smaller number of hydrogen bonds or forming weak hydrogen bonds to ensure efficient and convenient vapor production. Many novel evaporator materials and effective water activation strategies have been proposed to stimulate rapid steam production and surpass the theoretical thermal limit. However, an in-depth understanding of the phase/enthalpy change process of water evaporation is unclear. In this review, a summary of theoretical analyses of vaporization enthalpy, general calculations, and characterization methods is provided. Various water activation mechanisms are also outlined to reduce evaporation enthalpy in evaporators. Moreover, unsolved issues associated with water activation are critically discussed to provide a direction for future research. Meanwhile, significant pioneering developments made in SVG are highlighted, hoping to provide a relatively entire chain for more scholars who are just stepping into this field.

to clean water has become a major global issue that requires to be solved urgently.^[1,2] The common methods to obtain clean water from non-potable water involve many technologies based on electrical energy, which is inconvenient, pollutes the environment, and costly, thus unsuitable for underdeveloped and remote decentralized areas. Recently, the emergence of solar-powered clean water generation technology, as an environmentally friendly, low-cost, and operational approach, has been given great attention as a dependable strategy to address global water shortage.^[3,4] Therefore, research on solar steam generation is climbing up year by year (Figure 1). Solar steam generation is based on two common phenomena—evaporation and condensation, which are widespread in nature. Several studies have investigated the complex interfacial conditions of water evaporation.^[5–7] During water evaporation, for the transfer of molecules and energy across the interface, liquid water molecules absorb extra energy to increase kinetic energy, which intensifies the movement


1. Introduction

Water, one of the most abundant compounds on the planet, is a vital resource for all living organisms. Along with population growth, climate change, and accelerated industrialization, access

of water molecules; water molecules escape from the water body and dissipate into the atmosphere when their kinetic energy (molecular motion) is higher than the cohesion energy between them. Then, the water vapor cools to form the condensate. Interface temperature, pressure, and vapor/liquid density are

D. Wei, C. Wang, J. Zhang, H. Zhao
 School of Materials Science and Engineering
 Shaanxi Key Laboratory of Green Preparation and Functionalization for Inorganic Materials
 Shaanxi University of Science and Technology
 Xi'an, Shaanxi 710021, China
 E-mail: wangcb@sust.edu.cn
 Y. Asakura, X. Xu, Y. Yamauchi
 Department of Materials Process Engineering
 Graduate School of Engineering
 Nagoya University
 Nagoya 464-8603, Japan
 E-mail: xingtao.xu@zjou.edu.cn; y.yamauchi@uq.edu.au

M. Eguchi, Y. Yamauchi
 Faculty of Science and Engineering
 Waseda University
 3-4-1 Okubo, Shinjuku, Tokyo 169-8555, Japan
 M. Eguchi, Y. Yamauchi
 Australian Institute for Bioengineering and Nanotechnology (AIBN)
 The University of Queensland
 Brisbane, Queensland 4072, Australia
 X. Xu
 Marine Science and Technology College
 Zhejiang Ocean University
 Zhoushan, Zhejiang 316022, China

 The ORCID identification number(s) for the author(s) of this article can be found under <https://doi.org/10.1002/adma.202212100>

© 2023 The Authors. Advanced Materials published by Wiley-VCH GmbH. This is an open access article under the terms of the Creative Commons Attribution License, which permits use, distribution and reproduction in any medium, provided the original work is properly cited.

DOI: 10.1002/adma.202212100

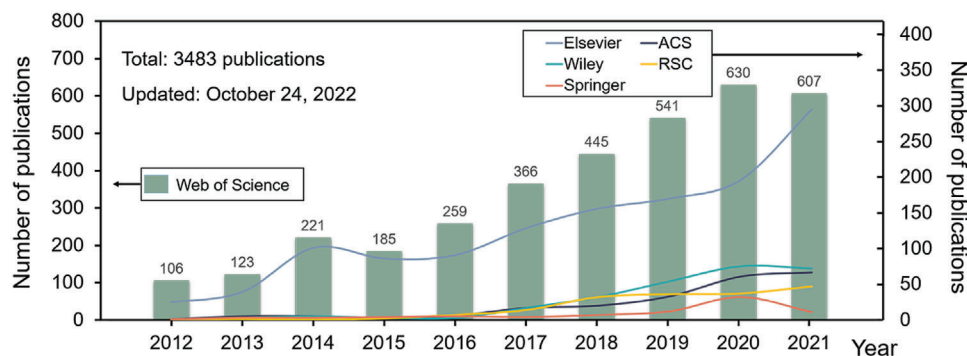


Figure 1. Number of publications per year from 2012 to 2021 that have used as the only hashtag. The data is updated to 2022.

discontinuous during water evaporation.^[8] Random molecular distribution and interaction forces of a liquid make the process of heat and mass transfer complex. Moreover, water and heat sources, saturation deficiency, and wind speed will all affect the water evaporation process.

In the solar-powered vapor generation (SVG) system, also known as solar steam generation or solar-driven interfacial evaporation, maximum proportion of the solar energy absorbed by the photothermal material is converted into the total enthalpy of liquid-gas phase change, and the remaining energy is utilized in managing losses, such as optical (reflection and transmission) and heat (radiation, conduction, and convection) losses.^[9] To improve the interfacial solar-to-thermal conversion ability of an SVG system for the enhancement of evaporation rate and efficient exploitation of solar energy, researchers have proposed various strategies. These strategies mainly involve the light-absorbing design of the system, heat regulation, and salt mitigation. Materials with high light absorption ability enhance absorbance in full spectrum range through continuous adjustment of their photothermal structure. However, the absorbance of the currently available light-absorbing materials can achieve the limited theoretical value of 100%, with little scope for optimization. Thermal management is another crucial part of the SVG system, which directly determines its photothermal conversion ability; it is indispensable for maximizing the utilization of solar power and minimizing heat loss (especially heat loss due to conduction). For example, reducing the thermal conductivity of materials,^[10,11] adding a thermal insulation layer for 2D evaporators,^[12] and limiting the area of water transportation^[13] can efficiently reduce heat loss. Design optimization of evaporators for heat loss reduction is another essential parameter. Water supply regulation is also particularly important for salt resistance. Salt crystal deposition can be effectively prevented by liquid pumping. In addition, studies on the development of self-cleaning/gravity-assisted cleaning surface,^[14,15] anti-clogging layer,^[16] Janus membranes,^[17] zero liquid discharge,^[18] and salt ion diffusion reflux^[19,20] are being extensively performed. These methods have been proven to be efficient in alleviating the damage of salt crystals to solar evaporators and even collecting salt crystals. While tremendous and continuous attempts are being explored to heighten evaporation rate (ER) and photothermal conversion efficiency (η), it is found that ER and η seem to reach the threshold, and the current technologies have not been able to improve these parameters any further.

We assessed that the following issues have not been paid required attention with respect to water evaporation: essence of water evaporation, different states of water during evaporation, and the type of energy supplied in each state of water. Therefore, water evaporation requires in-depth investigation. Specifically, water evaporation refers to the transition of water from a liquid state to a gaseous state. In the process of steam generation, the water molecules escaping from the liquid water should overcome the attraction of the molecules on the liquid surface layer. This attraction is mainly the intermolecular force of the hydrogen bonds, and their cleavage is the only way to change the state of water. Therefore, models should be developed to reduce the amount of energy required for evaporation by cleaving a smaller number of hydrogen bonds or by forming weak hydrogen bonds to ensure efficient and convenient vapor production. Yu et al. were the first to investigate this aspect of water evaporation, and they proposed that the energy required during water evaporation (i.e., evaporation enthalpy described in detail later) could be significantly reduced based on the idea of increasing the content of intermediate water (IW) and forming water clusters in a molecular network.^[21] They prepared hierarchically nanostructured polymer gel (HNG) and reported high evaporation rate under 1 sun radiation ($3.2 \text{ kg m}^{-2} \text{ h}^{-1}$), which was much higher than that reported by other studies during the same period. This provided a new direction for understanding the underlying mechanisms of water evaporation and new methods to optimize seawater desalination systems; this study also enhanced the interest of other researchers in investigating methods to reduce vaporization enthalpy of evaporators. Recently, He et al. defined the maximum evaporation rate as “Bulk Water Cap” when assuming 100% photothermal conversion efficiency.^[22] This value was $1.7 \text{ kg m}^{-2} \text{ h}^{-1}$ based on conservative calculations, which was far below the real energy demand during evaporation. Therefore, the fundamental way to dispose of low evaporation rate is to regulate the state of water such that the “Bulk Water Cap” can be increased, thus the energy used for evaporation can be reduced. However, as of today there is neither detailed research about water state management nor systematic characterization tests for expounding the whole process, let alone the discussion on the mechanism of lowering evaporation enthalpy.

In this review, innovations in SVG systems have been discussed to provide a comprehensive database for beginners in the field. To further understand the importance of decreased energy

requirement during steam production, we have summarized theoretical analyses of vaporization enthalpy, calculation methods in terms of complete and incomplete dehydration evaporation, and characterization of different states of water. Moreover, we outline the underlying mechanisms responsible for water activation to lower evaporation enthalpy reduction with respect to the formation of IW, clustered water, and capillary water. Finally, the challenges and perspectives related to vaporization enthalpy are highlighted to elucidate the future perspectives of SVG.

2. Breakthrough Research on SVG Systems

In the last decade, SVG systems have attracted attention as they use green and cost-friendly thermal desalination technology. In the study of water vapor generation from seawater driven by solar, the heating mode of water has undergone three substantial changes: from the initial direct bottom heating of the c to integral heating using nanofluids and finally the currently used interfacial heating; this evolution has serially minimized innocent heat loss energy. The continuous emergence of light absorbers such as plasma metal nanoparticles, degradable biomass, and spectrally selective absorbers, as well as design optimization of photothermal structures, have immensely improved the sunlight-absorbing capacity of SVG systems. In the rapid development of SVG systems, we have been fortunate to witness many popular scientific studies, and it is these pioneering researches that have propelled the prosperity of SVG. In this section, we summarize milestone research in the field of SVG based on four parameters, namely heat management, mass control, water state adjustment, and multifunctional applications, aiming to provide a relatively complete SVG development chain for more scholars who are just stepping into this field (Figure 2).

2.1. Heat Management

Scientists are continuously investigating effective heat management systems to minimize unnecessary energy loss during the process of water evaporation. The first study on this topic was published in 2012 by Halas et al. who proposed a thermal separation model using plasmon absorbers dispersed in bulk water during evaporation.^[23] They pointed out the disadvantages of the traditional model, which considered direct heating between the nanoparticles and the surrounding water. Moreover, they argued that in the traditional model, the energy absorbed by the nanoparticles was separated from the surrounding water. Steam appeared a few seconds after heating, and the surrounding liquid did not exhibit obvious signs of being heated. To our best knowledge, it was one of the first studies that proposed that metal nanoparticles could be efficiently applied in steam generation without substantial heat loss. Specifically, only a small part of absorbed sunlight is used for heating liquid water, and most of the remaining energy is used for steam generation. Subsequently, inspired by the transpiration and sweating of plants and animals, Deng et al. invented a thin film composed of gold nanoparticles floating at the air–liquid interface,^[24] which enlightened the concept of thermal localization. Nevertheless, metal

nanofluids often require high optical density or electromagnetic wave radiation to achieve local heating, which makes the equipment complex and expensive, thus difficult to fabricate. Moreover, the nanofluid heating method leads to marginal enhancement in photothermal conversion efficiency, which is not tailored for the rapid generation of steam and goes against water evaporation. Therefore, high photothermal conversion efficiency is a challenge even at low optical density. The principal solution is to maximize the utilization of solar power by reducing energy loss in the photothermal conversion process. Chen et al. fabricated a brand-new carbon-based double-layer structure (DLS) composed of a sunlight-absorbing layer and a thermal insulating layer,^[25] which could produce vapor in nonvacuum and low optical density conditions without heating bulk water. This structure confined the absorbed thermal energy to the evaporating surface and minimized dissipated energy, which was represented by “heat localization”. Therefore, an unprecedented performance was achieved, with energy efficiency as high as 85% under 10 sun radiations. This study not only introduced the concept of heat localization to the general public, but also broadened the application of DLS to SVG. Since then, several scientists have exploited the interfacial-heating structure to obtain higher efficiency than that obtained earlier. Moreover, to maintain the interfacial heating capacity, Wang’s team designed a hydrophobic self-healing membrane, which could restore the hydrophobic surface in 1 h at 1 kW m^{−2} because of the self-migration of fluorosilanes.^[26] The membrane maintained the local temperature of the interfacial water, and therefore, a relatively high evaporation rate could be obtained. Unlike the DLS, which uses carbon foam as the insulation layer, Deng et al. selected air-laid paper as an alternative^[27] because of its high mechanical stability, low thermal conductivity, enhanced surface roughness, and microporosity.^[28] Not only that, air-laid paper could serve as transferable support for AuNPs film, which enabled large-scale production; they transitioned from a thin 2D film to a 3D layout of the evaporator because gold nanoparticle-based film was coated on the surface of the air-laid paper. The 3D porous architecture inside air-laid paper could heighten multiple scattering of light to enhance light absorption. Apart from the air-laid paper matrix, researchers also adopted porous anodic aluminum oxide (AAO) as templates fabricated by the traditional two-step anodization method^[29] because of their reduced surface reflection and enhanced internal light scattering.^[30] For example, black gold membranes were developed by sputtering a thin film of gold on AAO templates by Kim et al. AAO could be used as a scaffold, and it reduced light reflection and improved light absorption capacity.^[31] In order to further obtain high-efficiency broadband light absorption, they adopted the adiabatic plasma nano-focusing technology to excite surface plasmon modes. Zhu et al. also deposited gold nanoparticles on a porous AAO host;^[32] the nanoparticles were tightly packed within the AAO nanopores, providing high optical density, increased multiple scattering effect, and low effective refractive index, so that a significantly enhanced absorption effect was obtained. They further revealed that aluminum, as a substitute for precious metals, had higher plasma frequency than gold, silver, and other metals, and thus exhibited noteworthy light response in the ultraviolet region. To achieve resonance over a wide wavelength range, they deposited aluminum nanoparticles on AAO supports.^[33] The natural oxidation of metallic aluminum



Figure 2. Pioneering developments in SVG systems. Volumetric heating. Reproduced with permission.^[23] Copyright 2013, American Chemical Society. Self-floating gold nanoparticle-based thin film. Reproduced with permission.^[24] Copyright 2014, Wiley-VCH. Double-layered structure: heat localization. Reproduced with permission.^[25] Copyright 2014, Springer Nature. Heat management. Reproduced with permission.^[26] Copyright 2015, Wiley-VCH. Reproduced with permission.^[31] Copyright 2015, Springer Nature. Reproduced with permission.^[27] Copyright 2015, Wiley-VCH. Reproduced with permission.^[32] Copyright 2016, AAAS. Reproduced with permission.^[33] Copyright 2016, Springer Nature. Reproduced with permission.^[36] Copyright 2016, Springer Nature. Reproduced with permission.^[40] Copyright 2016, Springer Nature. Reproduced with permission.^[9] Copyright 2017, Oxford University Press. Reproduced with permission.^[13] Copyright 2017, Wiley-VCH. Reproduced with permission.^[34] Copyright 2018, Wiley-VCH. Reproduced with permission.^[35] Copyright 2018, Elsevier. Reproduced with permission.^[37] Copyright 2020, Springer Nature. Reproduced with permission.^[38] Copyright 2022, Springer Nature. Mass control. Reproduced with permission.^[41] Copyright 2015, American Chemical Society. Reproduced with permission.^[42] Copyright 2018, Wiley-VCH. Reproduced with permission.^[43] Copyright 2018, Springer Nature. Reproduced with permission.^[44] Copyright 2018, Springer Nature. Reproduced with permission.^[45] Copyright 2019, Royal Society of Chemistry. Reproduced with permission.^[47] Copyright 2019, Royal Society of Chemistry. Reproduced with permission.^[48] Copyright 2019, Wiley-VCH. Reproduced with permission.^[18] Copyright 2020, Springer Nature. Reproduced with permission.^[49] Copyright 2020, Royal Society of Chemistry. Reproduced with permission.^[46] Copyright 2021, Wiley-VCH. Reproduced with permission.^[50] Copyright 2022, Wiley-VCH. Water state adjustment. Reproduced with permission.^[21] Copyright 2018, Springer Nature. Reproduced with permission.^[51] Copyright 2018, Royal Society of Chemistry. Reproduced with permission.^[54] Copyright 2019, Wiley-VCH. Reproduced with permission.^[58] Copyright 2020, Springer Nature. Reproduced with permission.^[59] Copyright 2020, Elsevier. Reproduced with permission.^[52] Copyright 2020, Royal Society of Chemistry. Reproduced with permission.^[60] Copyright 2021, Elsevier. Reproduced with permission.^[61] Copyright 2021, Springer Nature. Reproduced with permission.^[62] Copyright 2021, Royal Society of Chemistry. Reproduced from “Photomolecular Effect Leading to Water Evaporation Exceeding Thermal Limit.”^[55] Copyright form Yaodong Tu, Jiawei Zhou, Shaoting Lin, Mohammed AlShrah, Xuanhe Zhao, and Gang Chen. Reproduced from “Photomolecular Effect: Visible Light Absorption at Water-Vapor Interface.”^[56] Copyright form Yaodong Tu and Gang Chen. Reproduced with permission.^[53] Copyright 2022, Wiley-VCH. Multifunctional application is reproduced with permission.^[66] Copyright 2017, Royal Society of Chemistry. Reproduced with permission.^[77] Copyright 2018, Wiley-VCH. Reproduced with permission.^[73] Copyright 2018, Haomin Song et al. Reproduced with permission.^[74] Copyright 2018, Elsevier. Reproduced with permission.^[64] Copyright 2018, Wiley-VCH. Reproduced with permission.^[67] Copyright 2019, Springer Nature. Reproduced with permission.^[70] Copyright 2018, Wiley-VCH. Reproduced with permission.^[71] Copyright 2020, Royal Society of Chemistry. Reproduced with permission.^[72] Copyright 2019, American Chemical Society. Reproduced with permission.^[65] Copyright 2020, Royal Society of Chemistry. Reproduced with permission.^[78] Copyright 2021, Wiley-VCH. Reproduced with permission.^[57] Copyright 2021, Elsevier. Reproduced with permission.^[80] Copyright 2022, Royal Society of Chemistry. Reproduced with permission.^[76] Copyright 2022, Elsevier. Reproduced with permission.^[79] Copyright 2022, Wiley-VCH.

increased the optical absorption bandwidth in the infrared region, enhancing the absorptivity of metal nanoparticles across the solar spectrum and achieving low-expense plasma-enhanced photothermal performance. Moreover, AAO nano-porous templates could synergize with metal particles to achieve efficient desalination. However, the AAO matrix is fragile and costly, which limits its practicality and wide diffusion. Based on this, Hu's team chose the low-expenditure, salt-resistant, and good mechanical properties of basswood as the 3D host of metal particles and prepared a 3D aligned porous plasmonic wood-based SVG system, achieving a light-thermal conversion of 85% under 10 kW m^{-2} radiation.^[34] Their work exhibits the potential of plasmonic wood-based SVG systems, thus providing a new direction for research on biomass matrix. In fact, these evaporators using different porous substrates are still essentially 2D struc-

tured evaporation devices, whereas 3D evaporators have superior evaporation performance due to their larger evaporation surface, lower surface evaporation temperature, reduced heat loss, and additional energy input. The umbrella structure designed by Zhu et al. and the cylindrical structure designed by Wang et al. have led to the wide acceptance of 3D evaporators. The 3D artificial transpiration device proposed by Zhu et al. minimized the heat loss and the dependence of the light-absorbing angle without additional optical and heat management systems, further facilitating evaporation.^[9] The 3D cup structure designed by Wang et al. could recover the energy reflected by the bottom of the 2D cup and absorb the thermal energy from ambient air, enhancing the vaporization efficiency to approximately 100%.^[35] As a result, several 3D evaporators are being developed. In addition to extensive research on the structure of evaporators, various absorbers

with high light-absorbing capacity have been exploited. Selective absorbers have been used as a special class of light absorption materials. A spectrally selective absorber (SSA) is a material with high photothermal conversion efficiency. It has high absorption rate in the visible and near-infrared regions, but low emissivity in the far-infrared region. Therefore, it can improve the absorption ability of heat absorbers for solar radiation energy and reduce the scattering ability of heat absorbers. For the first time, Chen's team applied SSA for SVG, with sunlight absorptance of 0.93 and emissivity of 0.07 at 100 °C.^[36] They generated 100 °C vapor without high optical density at room temperature using in-plane thermal concentration (evaporating region < absorbing region) and thermal localization concepts. This study expanded the field of solar absorbers and offers more possibilities for solar energy accumulation. Prasher et al. combined SSA and blackbody emitter to develop the solar umbrella structure that exhibited radiation coupling of a photothermal conversion device.^[37] The device shifted light radiation to the mid-infrared or larger wavelengths so that higher surface temperatures could be obtained along with increased evaporation rates. Moreover, the non-contact feature of the structure is expected to be applied in treatment of wastewater without pollutants. Recently, Qu et al. developed a deformable conical evaporator array, which can reconfigure itself by responding to a magnetic field.^[38] This magnetically responsive dynamic evaporator could enhance the evaporation rate to 5.9 kg m⁻² h⁻¹ under 1 kW m⁻² radiation, which is far superior to that of other static evaporators. This concept of dynamic recombination structure further promotes the development of high-speed water evaporation systems. Xu et al. selectively removed the middle part of the evaporation surface, which strengthened the air convection above the whole evaporation surface and further accelerated the escape of steam.^[39] Therefore, the strategy "more from less" was put forward, which meant utilizing fewer materials to obtain higher evaporation rate. These strategies provide new directions to determine suitable heat and mass management systems for high-speed evaporation using the SVG technology.

In a water evaporation system, in addition to ensuring outstanding thermal management capabilities, the focus should be on the quality of water delivery to ensure continuous steam generation. The delivery step inevitably causes heating of the water body; therefore, the water quantity should be confirmed while minimizing heat loss caused by the delivery path. In the traditional design, the direct contact of energy with bulk water provides effective transfer of solar energy, but it leads to substantial intrinsic heat loss to bulk water. Therefore, various groups of scientists, especially Zhu's team, have successively designed different water delivery paths to avoid energy loss due to direct contact. In 2016, they successfully developed a 2D water path using polystyrene foam as the insulation layer and hydrophilic cellulose wrapped outside the insulation layer as the water delivery path.^[40] Owing to the reduced heat loss of the water delivery path, the evaporator exhibited efficient and stable energy transfer efficiency, independent of bulk water quantity, without extra thermal-isolation supporting systems. This paper is one of the first to introduce the concept of using a confined 2D water delivery pathway to lower the energy loss to bulk water. In 2017, inspired by water transport in plants, they continued to improve the design of their 3D evaporator and proposed the 1D water

transport channel.^[9] This channel greatly reduced heat loss by conduction, convection, and radiation without the aid of an insulator. Moreover, 3D evaporators had larger evaporation surface, lower surface evaporation temperature, and reduced heat loss, achieving superior evaporation performance. Furthermore, it could be used to manage water pollution. They also directly used carbonized mushrooms with umbrella-shaped black caps and porous fibrous stalks as solar evaporators because their inherent 1D water delivery path can substantially reduce heat loss.^[13] This paper was one of the first to demonstrate the benefits of 1D water delivery path for utilizing the harvested solar energy for steam generation with minimal thermal loss. Collectively, these studies outline a critical role of heat management in improving the performance of SVG systems. By simultaneously regulating light absorption, water transportation, and heat regulation, a high-efficiency solar evaporator can be developed for clean water production.

2.2. Mass Control

During the desalination process, clean water vapor is produced from brine and is accompanied with the deposition of salt crystals. With time, the salt particles accumulated on the surface of the evaporator not only block the light-absorbing material leading to decreased absorption performance, but also affect the life of the water evaporator, thus influence evaporation stability. As a result, inhibiting salt crystal accumulation while synchronously retaining thermal localization is a challenge. Salt resistance management should be considered an essential parameter for the development of solar evaporators, which is often realized through unique structural design and wettability regulation. Jiang et al. designed superhydrophobic self-floating carbon black membranes.^[41] Due to their superhydrophobic property and low adhesion to water, the membrane surface did not capture liquid droplets and thus exhibited self-cleaning ability. However, the contact angle of this superhydrophobic black gauze becomes smaller after long-term exposure to high-intensity light; therefore, the membrane needs further research. The flexible Janus membrane (CB/PMMA-PAN) fabricated by Zhu's team through electrospinning exhibited long-term stability for salt mitigation.^[42] This study demonstrates that the Janus structure, consisting of an upper hydrophobic skeleton and a lower hydrophilic network of deposited carbon black nanoparticles, can dissolve salt ions during continuous water delivery to effectively prevent solid salt deposition. Based on the property of salt reflux, Chen's team developed a salt-rejecting vaporization structure, capable of seawater desalination at an evaporation rate of 2.5 L m⁻² day⁻¹.^[43] However, these methods produce a large amount of waste brine as the byproduct, which is harmful to the ecological environment. Therefore, the concept of zero liquid discharge (ZLD) was invented, which promotes zero production of waste-products. Wang's group fabricated a low-cost 3D cup-shaped steam generator.^[44] This water evaporator used solar power as the single source of energy, and the main light-absorbing layer was placed at the bottom of the cup to separate the salt deposition surface from the optical absorption surface. Consequently, salt particles were only deposited on the sidewalls when water evaporated without affecting the light-absorbing

surface, and the resulting salt crystals could be easily collected. Their results elucidated that the evaporator could consistently adhere to the green ZLD concept as long as the salt in the solution was at a concentration <15 wt%. This emerging solar steam design concept provides a feasible idea for desalination of high-salinity seawater. Similarly, using a 1D water delivery path, Zhang et al. spatially isolated salt crystals, which were present only at the edge of the salt disk.^[45] This was the only study to report a solar evaporator at the time that continuously generated vapor for up to 600 h without salt particle accumulation. In addition to the disc-shaped structure, the spherical evaporator designed by Xu et al. was susceptible to weight imbalance under the action of gravity, thus realizing the self-cleaning function.^[46] Hu's team used simple fabrication methods and low-cost raw materials to demonstrate the important role of bimodal pore channels as salt barriers.^[47] They chose natural balsa wood with bimodal pores as the salt-resistant evaporator. The comparatively large vessel channels (about 180–390 μm) in the bimodal pores were employed for fast capillary pumping, while water diffusion and convection could be allowed between the small channels (about 18–39 μm). Therefore, the evaporated brine on the surface was quickly replenished, avoiding salt buildup, thus ensuring rapid clean water vapor generation. Similarly, Liu et al. proposed a hanging photothermal fabric structure,^[48] in which, the two sides of the photothermal material were immersed in seawater, whereas the other parts were suspended in air without direct contact with water, which obviously minimized heat loss to water and produced a higher surface temperature (40 °C). Moreover, solid salt was not accumulated, as the concentrated brine dripped from the bottom of the curved fabric. This design enhanced the effective evaporation area of the system, leading to an evaporation rate of 1.94 $\text{kg m}^{-2} \text{h}^{-1}$ due to the presence of two reaction surfaces, i.e., at the top and bottom. Song et al. designed an evaporator with a 3D gradient water path that could spontaneously form a water film with thickness inhomogeneity and temperature gradient; this was based on the superfluid transport properties of bionic structure surface.^[18] Furthermore, drawing on insights from the Marangoni effect, this solar evaporator fully utilized the input energy and only crystallized salt locally, without affecting the overall performance of the evaporator. Similarly, Asinari et al. combined the Marangoni effect with the passive desalination technology of multi-stage distillation^[49] systems and elucidated that salt-tolerance performance could be enhanced by focusing on the correlation between the desalination process and the theoretical effect. They described the salt accumulation phenomenon and concluded that the Marangoni effect was responsible for the enhanced salt resistance of this evaporator. This study investigated the application of the Marangoni theory to the brine desalination process, which was never put to use before to discuss passive desalination techniques. Recently, Caruso et al. achieved efficient selective crystallization of salt by wrapping and fixing hydrophilic nylon threads on a photothermal sponge, which allowed salt crystals to remain oriented on the wrapped threads.^[50] These studies and strategies of salt depression undertaken here, have expanded and enhanced our understanding regarding various methods that can be used for desalination during interfacial solar steam generation, thus promoting the development and popularization of newer and more effective salt resistance strategies.

2.3. Water State Adjustment

Recently, several studies have reported that the behavior of water during evaporation can be changed and the energy needed for evaporation can be reduced by regulating the state of water in the porous network. As per the present research, three main types of water can reduce evaporation energy requirements: IW, capillary water, and clustered water. In this part, we will summarize pioneering studies on changing the state of water in evaporators (other advanced themes will be elaborated in Section 4). In 2018, Yu's team proposed a hierarchically nanostructured gel (HNG) evaporator, and the evaporation rate reached 3.2 $\text{kg m}^{-2} \text{h}^{-1}$ under one solar illumination, which was twice that of the reported rate at that time.^[21] The self-floating hydrogel greatly enhanced the evaporation performance because of the increased IW and clustered water levels with low energy requirements. For the first time, they proposed that water molecules in a hydrogel molecular mesh possess reduced latent heat of evaporation, which surpasses the thermal vaporization limit and leads to higher evaporation rate. Furthermore, they successfully designed capillary water pathway hydrogel^[51] and patch-surface hydrogel (PSH),^[52] both exhibited high evaporation performance. In 2022, they prepared polyelectrolyte gel for high-salinity solar seawater purification.^[53] High SVG performance was reported by virtue of the significantly reduced evaporation enthalpy of the hydrogel (817.4 J g^{-1}). In 2019, analogous to the classification of water in the soil, Qu and co-workers demonstrated that the capillary water content in carbon-based photothermal materials could be controlled by a self-invented injection control technique (ICT).^[54] Capillary water did not obstruct the pore channels, thus increasing its content would expose larger evaporation area and create low evaporation enthalpy. The ICT facilitated the transportation of capillary water to maximize the utilization of solar energy and attained 100% thermal efficiency in SVG systems. This research provides another feasible method using carbon-based materials to enhance SVG performance, suggesting that capillary water should be further investigated. Recently, Chen's team investigated the causes of evaporation beyond the thermal limit at the water-steam interface when sunlight drove water evaporation.^[55,56] They proposed the photomolecular effect in solar-driven interfacial evaporation, which refers to the action of photons that can cause water clusters to cleave from the absorber surface. This induces vapor generation from porous hydrogels under normal sunlight or visible-light radiation, surpassing the theoretical vaporization limit. This study reported the photomolecular effect of clustered water for the first time, which provides an innovative direction and platform for theoretical research on interfacial water evaporation. Together these studies^[21,51,57–62] provide important insights into the regulation of water movement in SVG systems, which is expected to improve their evaporation performance.

It is worth pointing out that although pioneer work in the field of SVG is divided into four categories, all studies have the same goal, i.e., to obtain higher evaporation rate and achieve long-term stable high-speed evaporation. Specifically, mass/heat management is an essential foundation to ensure liquid pumping and energy utilization; and salt resistance is the main obstacle for long-term high stability applications; multifunctionality is an important way to achieve efficient and integrated energy use; and

reducing evaporation enthalpy is a key theoretical breakthrough to achieve high-speed evaporation. Regardless of material selection or structural design, all aspects provide a new platform for water treatment. However, SVG technologies require further research with respect to clean-water yield, cold steam collection, and high-salinity seawater desalination. The water state adjustment method, theoretical basis, material system, and characterization methods of the system also require further elucidation. Moreover, structural design should be continuously explored because designing new structures and devices using existing materials to meet different application scenarios will promote the multifunctional application of these materials in interdisciplinary fields.

2.4. Multifunctional Applications

The SVG technology uses ubiquitous solar energy and non-potable water (e.g., lake water, salt water, rainfalls, waste water, etc.) as the resources, and it has a vital function in motivating diversiform applications.^[63] Several studies have investigated potentially multifunctional applications of SVG, such as water purification, latent heat circulation, electric-thermal cooperation, power generation, waste heat utilization, agricultural irrigation, sterilization, and cooling. These applications enhance the practicability of SVG and possibilities for the application of solar energy and non-potable water. In a conventional steam generator, absorption and evaporation are performed at the same interface, which causes heat losses. A multi-stage distillation device built on the concept of recycling latent heat decouples the absorption and interfacial heating functions of the evaporator on two separate surfaces, thus leading to the development of a steam output device with low energy consumption. Moreover, this device only requires a combination of materials with different functions, instead of searching for specific materials with supporting both processes (heat absorption and evaporation), making the selection of materials more flexible and extending its range of applications. Asinari et al. designed a passively heated solar multi-stage distiller (MD) with a parallel structure that exhibited latent heat circulation without any mechanical device;^[64] the device only required non-intensive solar power as the energy input; and successfully demonstrated the feasibility of a latent heat recycling device with an evaporation rate of $3 \text{ kg m}^{-2} \text{ h}^{-1}$ and a clean water productivity of $2.95 \pm 0.02 \text{ kg m}^{-2} \text{ h}^{-1}$ in a 10-stage MD under >1 sun radiation. To reduce the contact surface area of the parallel structure MD device with saltwater, Wang et al. further developed a vertically aligned MD with an adjustable tilt angle,^[65] which could significantly lower the parasitic heat loss because of the negligible contact area of the thin film evaporator with a large amount of bulk water; an ultra-high water production rate of $5.78 \text{ L m}^{-2} \text{ h}^{-1}$ was obtained under 1 sun radiation. The vertical installation can be operated universally for different solar positions according to geographical and seasonal changes. Solar-powered desalination methods produce clean water while using the resulting salt gradient to generate electricity. Zhou's team prepared a solar-driven device for synchronous steam and electricity generation, which could generate electricity of 12.5 W m^{-2} under 1 sun illumination by exploiting the salinity difference between the surface water of

the absorption layer and the saline water.^[66] During steam generation, a region of high salt concentration was formed along with the appearance of saturated brine on the absorber surface. This led to a salt concentration gradient, which is directly responsible for the electricity generated by salinity. In previous studies, researchers have ignored the role of differences in salinity, but in this work, the potential of solar desalination systems was demonstrated by converting the salt concentration gradient into electricity through commercial Nafion membranes. Wang et al. then added solar panel modules on the basis of a solar interface evaporation system.^[67] The solar cell utilized short-wavelength sunlight to generate electricity through the photovoltaic effect, thus ensuring vapor production and high solar power generation efficiency. The electrical energy produced by solar cells can also be continuously applied for steam generation. Wang et al. reported efficient photo- and electro-thermal energy conversion and storage using self-assembled graphite nanosheets and synthesized high thermal/electrical conductivity composite phase change materials.^[68] Yu et al. also proposed a high thermal conductivity phase change material based on graphene aerogel with a concentric ring structure and reported high-efficiency solar-thermal-electrical energy conversion.^[69] Considering the lower water production rate of solar interfacial evaporation systems, Qu's team exploited the light-electricity-thermal relationship, and the synergy between solar cells and porous graphene-based evaporators led to the production of vapor simultaneously.^[70] The introduction of solar panels offered an additional source of heat energy (by electro-heat effect) for water evaporation, thus increasing the amount of steam produced. In addition, the solar panels ensured all-weather steam production. Yang et al. coupled the photothermal effect of MXene-based aerogel evaporator with the electrothermal function of solar cells to achieve all-weather, non-stop, and efficient steam generation.^[71] Besides latent heat recycling, hybrid energy harvesting could also recover free heat energy from the surface, the waste heat of laboratory facilities, and building walls, which is beneficial for the evaporation process. Tan et al. developed a tri-layered evaporator with the ability to synchronize the accumulation of free energy other than solar radiant energy.^[72] The evaporator not only exhibited an evaporation rate of $>2.4 \text{ kg m}^{-2} \text{ h}^{-1}$, but it captured other hybrid energies, relieving the liquid evaporation process from the intermittent influence of solar energy. This design had important reference significance for the development of mobile and all-weather water purification devices. The steam generation systems described above are based on the water evaporation caused by high-temperature surfaces. However, Gan's team reported an evaporator generating cold steam with near-ideal energy conversion efficiency, and the measured evaporation rate approached $2.20 \text{ kg m}^{-2} \text{ h}^{-1}$ under 1 sun illumination.^[73] Furthermore, the system could harness additional energy from warm surroundings when the working temperature was lower than the ambient temperature; at this time, the total steam generation rate of the system was higher than the theoretical limit value of input solar power. This paper outlined the key roles of cold-vapor generation systems (below room temperature) as an emerging platform for environmental energy utilization. Moreover, Zhu's team demonstrated for the first time that enhanced ambient energy-based steam generation could be achieved through optimized structural designs.^[74] The structure reported in this paper reduced the temperature of the absorber

surface, which was lower than the ambient temperature; the temperature of the side walls of the evaporator was also below the ambient temperature due to evaporative cooling. Therefore, due to lower than ambient temperature of both surfaces, they could absorb energy from the environment to increase evaporation rate above the theoretical limit. This structural design concept provides a new method for utilizing additional environmental energy. In addition to absorbing environmental energy, evaporators that obtain additional energy from bulk water are being developed. Xu et al. developed a 3D evaporator supported by highly thermally conductive materials that could harness energy from the environment and water body.^[75] However, in 3D interfacial evaporation systems, a thermal insulation layer that completely isolated the energy transfer between bulk water and the evaporation surface would hinder the process of obtaining energy from water and thus unfavorable to maximize evaporation. This article by Xu et al. jumped out of the inertia thinking and reported a novel 2D evaporator thermal management design. In contrast, high thermal conductivity material instead of an insulator was used to connect the evaporation surface in a 3D evaporator. Moreover, the energy stored in water could be effectively drawn to the gas-water interface when the evaporation surface was supported using a high thermal conductivity substrate material, which increased the total energy intake and further enhanced evaporation performance. This discovery offered a new idea for the research of 3D optical-thermal evaporators. At the same time, we can use water as an excellent energy source to accelerate photothermal evaporation. Based on these breakthroughs, interfacial solar evaporation technology has made important advances in acquiring other types of energy for water treatment. However, the absorption of environmental energy presupposes that the evaporation device is in an open environment, but the collection of fresh water is usually done in a closed environment. Therefore, the application of this strategy is challenging in freshwater acquisition. Besides, water evaporation can be used to harness water for repairing saline soil and simultaneously enhancing agricultural sustainability. Owens et al. designed a combined system of SVG and agricultural planting, and used treated seawater for saline-alkali land mitigation and agricultural irrigation.^[76] This evaporator was three times more efficient in soil washing than conventional distillation units and had a significant freshwater yield of up to $10.95 \text{ kg m}^{-2} \text{ day}^{-1}$ in outdoor experiments. The system extended the application of water evaporator to saline soil remediation, and it provided a potential and feasible solution to alleviate agricultural issues related to freshwater shortage and soil salinization. Besides agricultural applications, solar steam sterilization has become one of the main sterilization methods for public health and safety. Zhu et al. built a low-cost, easy-to-operate solar steam sterilization setup based on biochar that exhibited rapid response and high-efficiency steam generation up to a temperature of 121°C .^[77] This device was especially useful in off-grid areas lacking operational sterilization technologies. This was the first report on dynamic advantages of interfacial SVG for sterilization. In 2021, Yu et al. proposed an anti-bacterial hydrogel (ABH), which not only had excellent biological disinfection effect (nearly 100% sterilization efficiency), but also exhibited outstanding photothermal activity.^[78] As a result, ABHs could provide efficient and stable purification of bacteria-containing water. Yu's team also designed a hydrogel that could directly remove

volatile organic compounds (VOCs) from water via SVG (details in Section 4.1.1).^[79] These multifunctional applications demonstrated that SVG technology can be effective for saline soil repair, sterilization, and VOC removal, which promotes the interdisciplinary application of the SVG technology. In 2022, Wang et al. proposed a design that could achieve sustainable cooling effect without electrical energy.^[80] This system exerted the cooling effect via the endothermic process during the dissolution of a solute with considerably positive solution enthalpy. Then, the 3D solute regenerator generated cooling solute by SVG. The results revealed that this system could attain a cooling power of 190 W m^{-2} under 1 sun radiation. This passive cooling design not only expands the application of solar energy storage and conversion in cooling, but also broadens the potential of SVG in solute regeneration. These innovations provide a glimpse of the versatility and producibility of solar-powered interfacial water evaporators in different applications. The substantial progress made in the past decade makes it imperative to summarize and predict the future development trends in this multidisciplinary field.

The evaporation and condensation processes in the SVG system make it possible to achieve pure water acquisition by using clean and renewable solar energy. For desalination of water using SVG systems, in addition to ensuring high evaporation rates, condensate collection is critical in advancing the practical application of the SVG system, which is the ultimate goal for achieving water purification. Although several efforts have been made to boost the evaporation rate of SVG systems using photothermal materials and efficient structural designs, the water production rate falls far short of the current requirements. Moreover, the water collection step has not been sufficiently investigated. Water collection, as an essential part of solar clean water generation, should be deeply concerned as a meaningful direction to fresh water acquisition. Typically, temperature difference between hot steam and the condensing wall of SVG system is needed to drive water condensation and realize water harvesting. In our opinion, two main methods are used to efficiently collect clean water in a solar desalination system. Mismatch strategy in position to separate evaporation surface and condensation surface from solar absorption surface is a promising method to realize enhanced high-efficiency water collection. For instance, Zhu et al. elaborately fabricated a single-stage inverted solar water purifier (Figure 3a) that successfully separated absorption and condensation surfaces. Moreover, the purifier exhibited an excellent water collection rate of $1.063 \text{ kg m}^{-2} \text{ h}^{-1}$, which was the highest among all single-stage solar purification systems.^[81] Qu et al. reported a Janus-interface solar-steam generator (Figure 3b), which decoupled the water evaporation and the solar-thermal conversion processes and obtained a record high water productivity of $1.95 \text{ kg m}^{-2} \text{ h}^{-1}$.^[62] Ideally, decoupling the evaporation and absorption processes may enhance the water collection efficiency. Therefore, it is essential to further investigate this approach to meet the water collection targets. Moreover, it can be an important and promising strategy to guarantee efficient water-harvesting by integrating solar steam generation technology with passive radiative condensation and fog collection technology. Although the traditional vapor condensation technique is effective, it cannot collect water in warm- or room-temperature environments. It depends on the temperature difference and convective/conductive heat-exchange with ambient environments.^[82] Passive radiative

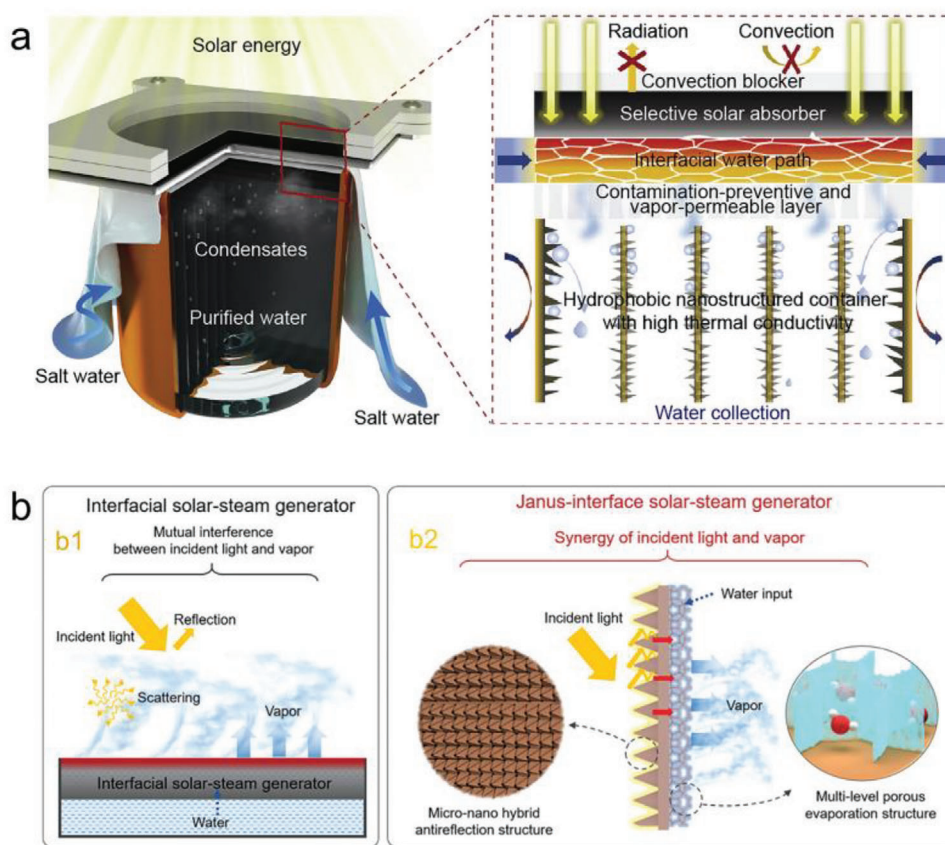


Figure 3. Designs of efficient water collection systems: a) one-stage inverted solar steam device for purified water collection, b) traditional in situ solar evaporator (b1), and Janus-interface solar vapor generator for enhancing water harvest (b2). Reproduced with permission.^[81] Copyright 2021, Elsevier. Reproduced with permission.^[62] Copyright 2021, Royal Society of Chemistry.

condensation is being widely explored as an effective water collection and purification technology.^[83,84] Depending on high solar reflectance and long-wave infrared emittance, this method can be used for water collection during the daytime. Besides, due to the enhanced transportation of harvested water, the hydrophobic/hydrophilic cooperative Janus system can improve fog collection significantly.^[85,86] We believe that efficient and continuous water collectors should be designed and fabricated on the basis of the decoupling strategy and cooperative system for water collection and preservation.

3. Mechanisms of Water Activation in SVG Systems and Their General Characteristics

Water is a polar molecule. The lone pair of the oxygen atom (with the negative charge) and the hydrogen atom (with the partial positive charge) in the water molecule establishes the donor-ligand coordination bond, i.e., the hydrogen bond. From the perspective of the hybridization orbital theory, the oxygen atom in a water molecule is sp^3 hybridized; therefore, one water molecule is surrounded by four water molecules, exhibiting a tetrahedral 3D spatial hydrogen-bonded network structure.^[87–90] In liquid water, the hydrogen bonds around the water molecules are constantly broken and reorganized due to continuous thermal motion, eventually reaching a state of equilibrium. In nature, water exists widely

in the form of free water (FW), bound water (BW), and IW, which are classified according to the association of water with a substance and the different strengths of interactions between them. FW, similar to bulk water, is free in the network, whereas BW and IW exhibit strong and weak hydrogen bond interactions, respectively. A few materials exhibit strong interactions with water molecules to form BW, which gives birth to weak hydrogen bonds between the surrounding water and other adjacent water molecules. It breaks the original hydrogen-bonded network between water molecules and produces abundant IW, thus altering the state of water and phase-transition behavior. The energy required to disrupt multiple hydrogen bonds gives rise to the elevated latent heat of water vaporization. IW possesses weak hydrogen bonds; therefore, the abundance of activated IW can reduce the evaporation energy, thus accelerating the water evaporation process. In order to measure and compare the degree of energy reduction of different materials, equivalent evaporation enthalpy has been introduced as an exact measurement in the water evaporation enthalpy reduction (WEER) system.

Several studies have investigated methods to reduce the equivalent enthalpy of evaporation to increase the evaporation rate, which is an important breakthrough in the production of water steam using SVG systems. However, a systematic summary on the fundamental mechanisms and characterization of enthalpy reduction is unavailable. Therefore, in this section, we

analyze and summarize the principles of evaporation enthalpy reduction from the perspective of thermodynamics theory and formula derivation. Moreover, we outline three common mechanisms of water activation in line with the three states of water in nature: 1) increasing the content of IW, with low energy demand, in the network; 2) adjusting the porous structure to obtain wider water clusters for reducing vaporization enthalpy; and 3) constructing a larger effective evaporation area by forming more capillary water that does not fill the pore structure to promote rapid water evaporation. Finally, we summarize two methods of calculating the equivalent enthalpy of evaporation and general characterization tools.

3.1. Theoretical Analysis of Vaporization Enthalpy

To theoretically prove that evaporation enthalpy is inextricably linked with the intermolecular potential energy (PE) of water, we analyze evaporation enthalpy based on thermodynamics in this section. Considering the influence of additional pressure caused by surface tension on the enthalpy of evaporation, we integrated the work of Yu et al.^[21,91] and Hu et al.^[92] for a comprehensive understanding of the topic. For the derivation of specific thermodynamic formulas, researchers can refer to the detailed deduction process in the original text (ref.[21]: “S2.14.5 Thermodynamic Analysis” in the supplementary information of the paper written by Yu; and ref. [92]: “Equation 3” in the paper written by Hu et al.).

The solar conversion efficiency (η) is defined as the ratio of the thermal energy stored in steam to the overall solar flux input, which can be expressed using the following equation (Equation 1):

$$\eta = (m \cdot h_{lv}) / (C_{opt} \cdot q_0) \quad (1)$$

m represents the mass flux of the evaporated water due to solar irradiation per unit of projected area, per unit time; h_{lv} is the total enthalpy vaporization; C_{opt} is the optical concentration of sunlight irradiance; and q_0 is the power of 1 sun irradiance per unit area (1 kW m^{-2}).

The total heat (h_{lv}) required for transition of water to vapor state includes sensible heat and latent heat in SVG systems.^[93] Sensible heat (ΔH_{sen}) changes the temperature of water without phase change when heat is added or removed. It can be calculated as follows:

$$\Delta H_{sen} = C \times (T - T_0) \quad (2)$$

C is the specific heat of water ($4.18 \text{ J g}^{-1} \text{ K}^{-1}$); T_0 is the original temperature of water (K); and T is the stable surface temperature of the sample evaluated using infrared camera (K). The latent heat of phase change (ΔH_{hiv}) refers to the heat absorbed or released by a unit mass of a substance from one phase to another under isothermal and isobaric conditions. We also use the word “enthalpy” (ΔH_{vap}), synonymous with it, which is the required energy for liquid water at the steady-state evaporation temperature to form the gaseous phase. This process is attributed to the cleavage of intermolecular interactions between water molecules, especially the hydrogen bonds (a detailed theoretical analysis is presented in the next paragraph). Considering that sensible heat is

less intense than latent heat, a reduction in energy demand suggests lowering the evaporation enthalpy of water. The enthalpy of evaporation is not only associated with the nature of the substance, such as the matrix and absorber, but also with the function of heated surface temperature (T), which is closely associated with the vapor pressure of the substance. Therefore, these parameters should be considered when regulating the state of water in an SVG system to obtain low evaporation enthalpy.

The evaporation enthalpy (H) depends on the cleavage of hydrogen bonds. Enthalpy can be calculated as follows:

$$H = E + pV \quad (3)$$

H is the enthalpy; E is the internal energy; p is the pressure; and V is the volume. The enthalpy of the gas phase can be calculated as follows:

$$H_{gas} = E_{gas} + pV_{gas} \quad (4)$$

The enthalpy for the liquid-water phase can be calculated as follows:

$$H_{l-water} = E_{l-water} + pV_{l-water} \quad (5)$$

The internal energy formula is a summation of PE U and kinetic energy K , which can be calculated as follows:

$$E = K + U \quad (6)$$

U can be further classified into intermolecular potential U^{inter} (i.e., the PE between different water molecules) and the intramolecular potential U^{intra} (i.e., the PE of the bonds within each water molecule). This can be calculated as follows:

$$U = U^{inter} + U^{intra} \quad (7)$$

After combining Equation 7 into Equation 6, the internal energy formulas for the gas and liquid-water phases are as follows:

$$E_{gas} = K_{gas} + U_{gas} = K_{gas} + U_{gas}^{intra} + U_{gas}^{inter} \quad (8)$$

$$E_{l-water} = K_{l-water} + U_{l-water} = K_{l-water} + U_{l-water}^{intra} + U_{l-water}^{inter} \quad (9)$$

U_{gas}^{inter} and $U_{l-water}^{inter}$ are the intermolecular PE between different water molecules, and U_{gas}^{intra} and $U_{l-water}^{intra}$ are the intramolecular PE of the bonds within each water molecule in the vapor and liquid water phase, respectively.

Substituting Equation 8 into Equation 4, we obtain:

$$H_{gas} = K_{gas} + U_{gas}^{intra} + U_{gas}^{inter} + pV_{gas} \quad (10)$$

For water vapor at room temperature at 1 atm, the intermolecular potential is negligible, and we can consider water vapor as an ideal gas, thus

$$pV_{gas} = Nk_B T \quad (11)$$

N is the number of water molecules; k_B is the Boltzmann constant; and T is the temperature.^[94]

Equation 10 could therefore be written as follows:

$$H_{\text{gas}} = K_{\text{gas}} + U_{\text{gas}}^{\text{intra}} + Nk_{\text{B}}T \quad (12)$$

By combining Equation 5 and Equation 9, the enthalpy of liquid water can be calculated as follows:

$$H_{\text{l-water}} = K_{\text{l-water}} + U_{\text{l-water}}^{\text{intra}} + U_{\text{l-water}}^{\text{inter}} + pV_{\text{l-water}} \quad (13)$$

By definition, the latent heat of water vaporization is the difference in enthalpy between the liquid phase and the gas phase:

$$\Delta H_{\text{vap}} = H_{\text{gas}} - H_{\text{l-water}} \quad (14)$$

Substituting Equation 12 and Equation 13 into Equation 14, the vaporization enthalpy is therefore as follows:

$$\begin{aligned} \Delta H_{\text{vap}} = & (K_{\text{gas}} - K_{\text{l-water}}) - U_{\text{l-water}}^{\text{inter}} \\ & + (U_{\text{gas}}^{\text{intra}} - U_{\text{l-water}}^{\text{intra}}) + (Nk_{\text{B}}T - pV_{\text{l-water}}) \end{aligned} \quad (15)$$

At the same temperature, the kinetic energy of water molecules in the liquid phase and gas phase is identical. Therefore, $K_{\text{gas}} - K_{\text{l-water}} = 0$. The vibrational energy of bonds in each water molecule should also be the same, irrespective of its phase; therefore, $U_{\text{gas}}^{\text{intra}} - U_{\text{l-water}}^{\text{intra}} = 0$.

For the same number of molecules, the volume of liquid water should be lower than that of water vapor. Therefore, $Nk_{\text{B}}T = pV_{\text{gas}} \gg pV_{\text{l-water}}$.

Equation 15 can therefore be simplified to obtain the final formula expressed as follows:^[21]

$$\Delta H_{\text{vap}} = -U_{\text{l-water}}^{\text{inter}} + Nk_{\text{B}}T \quad (16)$$

However, considering the influence of additional pressure caused by surface tension on the enthalpy of evaporation, the surface tension-driven pressure (ΔP) is expressed using the following equation:^[92]

$$\Delta P = 4\sigma \frac{\cos\theta}{r} \quad (17)$$

σ is the water gas-liquid surface tension; θ is the contact angle; and r is the pore radius. Using Equation 11, Equation 16 can be presented as follows:

$$\Delta H_{\text{vap}} = -U_{\text{l-water}}^{\text{inter}} + \left[Nk_{\text{B}}T - \left(p + 4\sigma \frac{\cos\theta}{r} \right) V_{\text{l-water}} \right] \quad (18)$$

Equations 16 and 18 theoretically prove that evaporation enthalpy is linked with the intermolecular PE of water. Therefore, the binding PE between water molecules should be reduced to reduce the evaporation enthalpy. This is an effective way to form weak hydrogen or non-hydrogen bonds, which can be easily broken (partially or completely) during the water evaporation process. Therefore, we propose the following strategies: increasing IW content, constructing abundant large-sized water clusters, or promoting the formation of capillary water that does not entirely occupy pore space, which are schematically shown in Figure 4a–c.

3.2. Increasing IW Content

In SVG systems, the most common evaporation structure is a hydrophilic polymer network; therefore, in this section, we begin with a hydrophilic polymer as an example. According to the interaction between water molecules and hydrophilic polymers or hydratable fibers, water is categorized as follows: FW, BW, and IW (Figure 4a). Based on this principle, FW is combined with the surrounding four water molecules whose structure is the closest to that of pure water, and its interaction with polymer chains or fibers can be neglected. On the contrary, BW contains strong interactions with the polar functional groups of polymer networks or fibers, presenting a stable structure. IW exists between FW and BW, and connects to less than four water molecules, exhibiting weak interactions with polymers and adjacent water molecules.^[95–97] Therefore, in consideration of the difficulty in breaking hydrogen bonds, it is easier to evaporate IW by harnessing less energy. The evaporation rate of IW is ca. 86 times faster than FW.^[98] This can be attributed to the following two reasons. The surface tension of IW is low due to the smaller number of hydrogen bonds and the presence of weak hydrogen bonds, which could be partially or completely broken during evaporation. Moreover, IW may have a higher localized temperature and larger evaporation surface area than FW because it is closer to the surface of the absorber, where it forms a confined nanospace and provides abundant thermal energy continually.^[99] Therefore, it is an important strategy to lessen energy consumption (less than that required for bulk water) for vapor generation by increasing IW content, thus reducing evaporation enthalpy of water.

3.3. Formation of Water Clusters

In nature, water does not exist as a single water molecule, but several water molecules aggregate by hydrogen bonding to form clusters. Water clusters are aggregates with specific configurations and topological patterns formed by the inconsecutive hydrogen-bonded structure of water molecules, and they can appear in ice, crystal lattice, and liquid water. To assess the number and size of water clusters in steam generation, according to the water cluster theory, it was reported that water can evaporate in the form of a single water molecule or entire water clusters.^[100,101] The structure of a water cluster is dynamic, i.e., water molecules are constantly joining or leaving a water cluster, and the size of the water cluster is not constant. A water cluster usually consists of more than two water molecules, which only break their hydrogen bonding with the surface when evaporating, whereas individual water molecules break all hydrogen bonds resulting in higher energy demand (Figure 4b). Besides, the monomers (or smaller clusters) of water molecules have comparatively higher velocity than large-sized clusters,^[100,101] according to velocity map imaging and mass spectroscopy, which directly shows the requirement of more energy to convert liquid-water to monomer-water-vapor than that for conversion of liquid-water to water-vapor clusters.

Moreover, we can calculate the enthalpy of vaporization from the absorber surface where water clusters are present in the vapor phase. Enthalpy of liquid-vapor with water clusters can be written

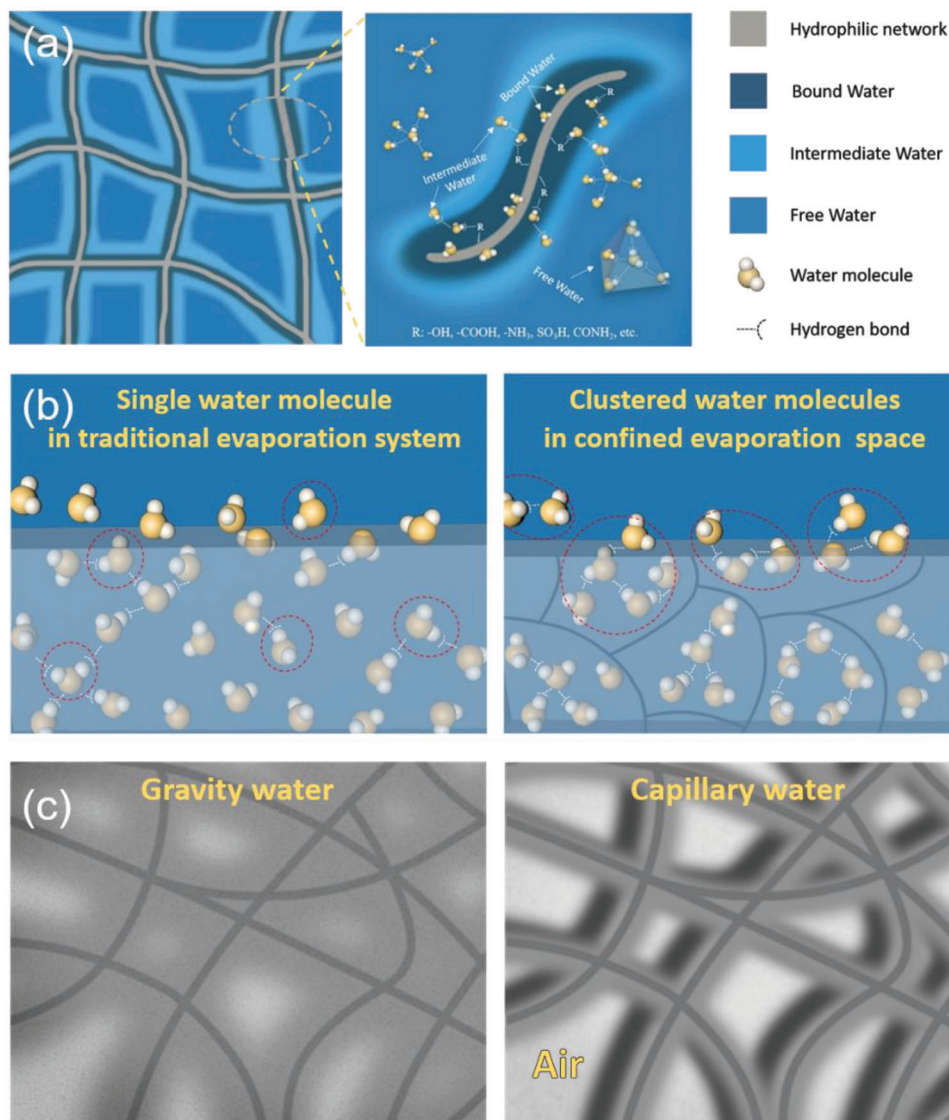


Figure 4. Diagram of water activation system: intermediate water, clustered water, and capillary water. a) Intermediate water possesses weaker hydrogen bonds, b) clustered water evaporates integrally with multiple water molecules, and c) capillary water exposes more evaporation space.

as follows (ref. [21]: “S2.14.5 Thermodynamic Analysis” in the supplementary information of the paper written by Yu et al.):^[21]

$$H_{\text{vap-cluster}} = \chi H_{\text{gas}} + (1 - \chi) H_{\text{cluster}} \quad (19)$$

χ , vapor quality, is the population of water molecules in the vapor phase, and H_{gas} and H_{cluster} are enthalpies of water vapor with single molecules and clusters, respectively.

Furthermore, Equation 14 for water clusters can be expressed as follows:

$$\Delta H_{\text{vap-cluster}} = H_{\text{vap-cluster}} - H_{\text{l-water}} \quad (20)$$

Combining Equation 19, Equation 14 can be written in terms of enthalpy change as follows:

$$\Delta H_{\text{vap-cluster}} = \chi H_{\text{vap}} + (1 - \chi) \Delta H_{\text{cluster}} \quad (21)$$

which includes two parts: ΔH_{vap} , already defined in Equation 14, represents the enthalpy change for water to be fully vaporized to gas phase, and $\Delta H_{\text{cluster}}$ is the enthalpy change for a cluster to escape from the network. Analogizing the derivation of Equation 16, the enthalpy of water clusters to vaporize from the surrounding water molecules can be presented as follows:

$$\Delta H_{\text{cluster}} = -U_{\text{cluster-water}} + Nk_{\text{B}}T \quad (22)$$

$-U_{\text{cluster-water}}$ is the energy required for clusters to escape from water.

Combining Equations 20, 21, and 19, we obtained the following formula for calculating evaporation enthalpy:

$$\Delta H_{\text{vap-cluster}} = -[\chi U_{\text{l-water}}^{\text{inter}} + (1 - \chi) U_{\text{cluster-water}}^{\text{inter}}] + Nk_{\text{B}}T \quad (23)$$

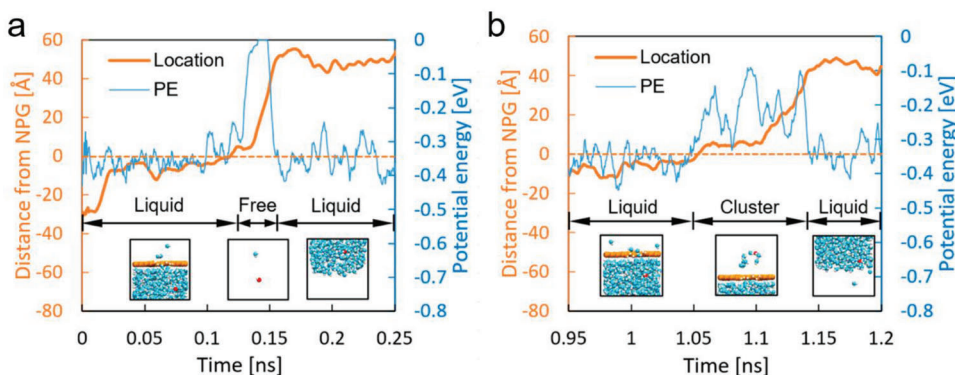


Figure 5. Evaluation of position and potential energy of water molecules during movement: a) one water molecule is completely evaporated, and b) one water molecule presented in 10-water-clusters is vaporized. Reproduced with permission.^[102] Copyright 2020, American Chemical Society.

Subtracting Equation 23 from 16, the following equation for calculating the change in evaporation enthalpy is obtained:

$$\Delta H_{\text{vap-cluster}} - \Delta H_{\text{vap}} = (1 - \chi) [(-U_{\text{cluster-water}}^{\text{inter}}) - (-U_{\text{l-water}}^{\text{inter}})] \quad (24)$$

Equation 24 exhibits that the evaporation enthalpy varies because of water clusters. Due to the difficulty in breaking hydrogen bonds, a water cluster needs lesser energy per molecule to escape from the neighboring liquid water than that required by a single molecule. Therefore, $-U_{\text{cluster-water}}^{\text{inter}} < -U_{\text{l-water}}^{\text{inter}}$, and $\Delta H_{\text{vap-cluster}} < \Delta H_{\text{vap}}$.

Through the derivation of the above formulas reported by Yu et al.,^[21] we can draw the conclusion that the evaporation of water clusters can reduce enthalpy change compared to that of the evaporation of an individual water molecule. Liu's group computed the PE and location evolutions of water clusters in a reverse thermo-osmosis system; they also investigated the unstable state of a water cluster.^[102] The results elucidated that the PE of water clusters was lower than that of FW molecules (Figure 5). Therefore, cluster evaporation consumes lower heat energy than the evaporation of a single water molecule at the same mass, thus reducing the enthalpy of evaporation.

Therefore, water clusters are evaporated to a state with lower enthalpy change than conventional latent heat.^[21] Furthermore, the activation of large-sized water clusters reduces the enthalpy of vaporization because the escape of water molecules in the form of clusters requires lower energy per unit mass than that required by monomers.

3.4. Enhancement of Capillary Water Content

Based on the existing states of water in soil, we can classify water in an evaporator system as follows: hygroscopic, film, capillary, and gravitational water (Figure 4c).^[54] When the water content is low, large amount of capillary water and a spot of hygroscopic/film water are present in the system, but gravitational water is absent. Hygroscopic water is closely adsorbed on the surface of the material, and the water film is a thin layer of water attached around the hygroscopic water, which hardly interacts with the material. However, when the water content is continuously increased to its saturation or supersaturation point, the

content of capillary water and hygroscopic/film water decreases and low amount of gravitational water can be observed. Gravitational water almost completely fills the pore channels, limiting the permeability and evaporation rate of water. Moreover, high water content not only wastes solar thermal energy, but also causes a decrease in surface temperature due to excess water retention on the sample surface, which hinders the rapid evaporation of water at the interface. In contrast, high content of capillary water is observed when the water content and hygroscopic/film water in the system are delicately controlled. The presence of capillary water prevents the micropores from being completely blocked, thus exposing a larger space for effective evaporation. The energy required to evaporate capillary water is lower than that of pure water, thus assisting in decreasing vaporization enthalpy. Moreover, capillary water content is not only affected by water content, but also closely related to the ratio of hygroscopic water to water film and the size of the capillary channel. Thus, a dynamic equilibrium could be achieved between the water supply rate and the evaporation rate by controlling the water feed. Based on these advantages, increase in the content of capillary water with low evaporation energy requirement should be targeted in the capillary channel, which can reduce the latent heat of evaporation and lead to more effective evaporation area.

Therefore, to achieve higher steam yields, the effective methods can be described as follows: First, IW content should be increased in hydrophilic structures (such as gels and fibers) because it has higher number of weak hydrogen bonds or non-hydrogen bonds and escapes from hydrophilic networks with less evaporation energy requirements. Second, liquid water molecules should be assisted to vaporize in the form of clusters by means of optimizing the structural design (details discussed in Section 4.2), which lowers the enthalpy of vaporization. Finally, capillary water content in the pore structure should be enhanced to form an unimpeded water evaporation process, which will reduce obstruction in evaporation. It is worth mentioning that the mechanisms mentioned above often appear in the same system and work in coordination to reduce the latent heat of evaporation.^[103] Taking advantage of IW and clustered water, Sun et al. proposed a double-layered hydrogel evaporator, called the Ag-PSS-AG/AG device, which was based on the hierarchical component of plasmon absorber and agarose (AG)

gel.^[104] The identical AG skeleton consisted of an Ag–PSS–AG layer on the top and a pure AG layer on the bottom. AG is rich in hydrophilic hydroxyl groups, which can weaken the hydrogen bonds between water molecules, thus increasing IW content (specific reason will be analyzed later in Section 4.1). Moreover, the AG network provided a continuous mesh structure and could form water clusters in the molecular mesh. The device exhibited an outstanding water management performance, which not only increased the content of IW, but also produced water clusters in the AG mesh, leading to an ultralow vaporization enthalpy of 1591.12 kJ kg^{−1} in the dark experiment tests. In terms of scale, the IW and clustered water mechanisms are based on molecular scale, whereas those involving capillary water are on a macroscopic scale. In terms of material synthesis, each mechanism has its own advantages and disadvantages. The IW mechanism is commonly used for water activation and several subsequent studies have been conducted based on this mechanism. It focuses on the synthesis and preparation of materials. Capillary water was proposed on the basis of the capillary water found in soil. Specifically, capillary water is formed by the surface tension at the interface between water and air. The formation of capillary water requires precise control of the water supply, therefore, a device fabricated based on the capillary water mechanism may be relatively complex and expensive. However, capillary water can be obtained without extra modulation of hydrophilic groups, making material synthesis easy and increasing the available material options. The characteristics of clustered water and its evaporation mechanism have not been extensively investigated, whereas capillary water can be observed using an optical microscope, and IW can be characterized qualitatively and quantitatively using advanced technologies, such as Raman spectroscopy and Fourier transform infrared spectroscopy (FTIR). However, there are few studies about capillary water mechanism at present, which is also worth exploring. Compared to that of traditional freshwater acquisition technologies, the advantage of interfacial water evaporation is completely passive evaporation, i.e., additional energy supply and mechanical moving parts are not required. Therefore, it is imperative to find a more convenient and competitive water activation mechanism.

3.5. General Calculation Methods and Characterization Analyses

3.5.1. Calculation of Equivalent Evaporation Enthalpy

Currently, two methods are used to calculate the equivalent enthalpy of evaporation, namely, the dark evaporation experiment and differential scanning calorimetry (DSC) method. However, the equivalent enthalpy obtained by these two methods is not the same, which could be attributed to both work on different principles. The dark evaporation experiment assumes constant energy input to establish an equivalence between pure water evaporation and WEER system; the method is simple and allows preliminary determination of the equivalent evaporation enthalpy. However, its value reflects the non-complete dehydration of the WEER system. The DSC test, which requires the use of an integral area, reflects complete dehydration of the steam as it is generated. In the following paragraphs, we briefly explain the calculation methods of these two tests.

For the dark evaporation experimental conditions, the energy input is assumed to be constant. Pure water is taken as the standard sample, and the evaporation enthalpy of pure water is fixed under specific temperature and pressure conditions. Only the dark evaporation rates of pure water and samples need to be measured, i.e., the equivalent evaporation enthalpy of samples can be obtained by one-step division. Specifically, the equivalent evaporation enthalpy (E_{equ}) of water in the sample can be estimated using Equation 25 when vaporizing the water with identical power input (U_{in}),

$$U_{\text{in}} = E_0 \cdot m_0 = E_{\text{equ}} \cdot m_g \quad (25)$$

E_0 and m_0 refer to the evaporation enthalpy and mass change of bulk water, respectively; m_g is the mass change of a sample under dark evaporation experiment conditions.

It is worth emphasizing that this calculation is based on idealized assumptions. In fact, the energy input between two systems in the estimation of evaporation enthalpy from Equation 25 has not been proven to be equivalent. The evaporation mass transfer process mainly depends on the solar flux and vapor pressure difference.^[105] In particular, unsaturated ambient humidity is an important factor for evaporation under dark conditions, in which case evaporation is a kinetically driven process. This process is driven by the vapor pressure difference between the evaporation surface and far-field ambient air. Specifically, in the dark evaporation experiment, the vapor pressure of the evaporation surface is saturated, which is higher than that of the far-field environment, and this vapor pressure difference drives the evaporation. Therefore, we believe that the evaporation in this case originates from the difference of vapor pressure between the evaporation surface and the far-field ambient air. Moreover, the evaporation surface uptakes heat energy from the atmosphere and bulk water when the surface of the material is at a lower temperature. Therefore, for two systems to possess identical energy input, it is a prerequisite that they have identical surface temperature and the thermal conductivity of the sample should be close to that of pure water. However, it cannot be guaranteed that the two systems can ensure equivalent energy input through natural evaporation. Therefore, the calculation method is not accurate enough and needs further improvement.

Dark evaporation experiments can roughly demonstrate the difference in evaporation enthalpies between a WEER system and pure water, as per detailed DSC thermodynamic analysis. The DSC method is applied for the measurement of evaporation energy of water; Figure 6a–f presents the thermograms of different systems and pure water where the DSC signal magnitudes are proportional to the heat flow during the measurements.^[21,22,91,103,104,106–108] DSC measurements are performed by investigating the evaporation process of water from T_1 to T_2 for a certain scan rate, under set nitrogen flow flux. During enthalpy tests, the sample is placed in an aluminum crucible with a perforated lid. The changes in the heat flow signal of the sample as a function of temperature are recorded. Bulk water is represented in the curve by a sharp peak (Figure 6), and the heat flow signal exhibits a downward trend dramatically after reaching the maximum value due to the exhaustion of water for the evaporation process. This indicates that the evaporation process of water is instantaneous. Nevertheless, the peak of the sample with

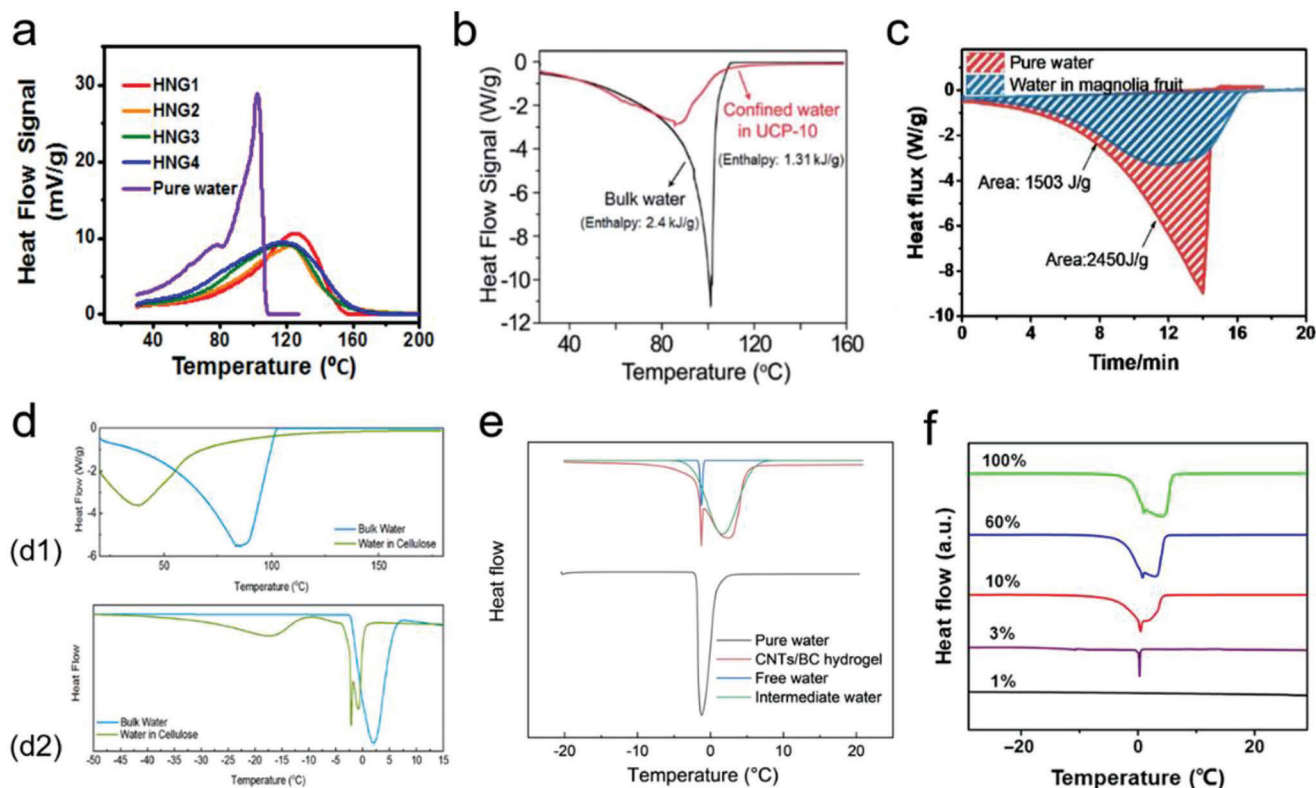


Figure 6. Thermograms of different evaporation systems and pure water exhibiting exothermic and endothermic peaks, where the DSC signals are proportional to the heat flow during the measurements. a) Exothermic signals in hierarchically nanostructured polymer gels (HNGs) as per DSC. Reproduced with permission.^[21] Copyright 2018, Springer Nature. b) Endothermic signals in UCP-10 with confined water as per DSC. Reproduced with permission.^[106] Copyright 2020, Royal Society of Chemistry. c) DSC test curves of water in magnolia fruit. Heat flow is recorded as a function of time, and the vaporization enthalpy can be calculated by accumulative area of heat flow and time. Reproduced with permission.^[107] Copyright 2019, WILEY-VCH. d) DSC curves of d1) evaporation and d2) melting behavior in cellulose. Reproduced with permission.^[22] Copyright 2020, Elsevier. e, f) DSC curves exhibit the melting behavior of water in carbon nanotubes (CNTs)/bacterial cellulose (BC) hydrogel and highly hydratable light-absorbing hydrogel (h-LAH) with varying water contents. Reproduced with permission.^[108] Copyright 2020, American Chemical Society. Reproduced with permission.^[91] Copyright 2019, American Association for the Advancement of Science.

reduced vaporization enthalpy is broader than that of pure water, and the heat flow signal exhibits a gradual decay, demonstrating that the liquid evaporation in the sample is distinct from that of pure water. The equivalent vaporization enthalpy can be estimated by integrating the heat flux in the time range; in Figure 6c, the straight line is chosen as the baseline for normalization.^[107]

It should be emphasized that the enthalpy obtained by the integral area of DSC curves is higher than that calculated via the dark evaporation experiment, which is because they represent complete and slight dehydration from the swelled state, respectively. In fact, the test results of the dark experiment are more in line with practical desalination applications because water molecules with weak hydrogen bonds continuously diffuse to the liquid-vapor interface from the water reservoir. Therefore, the dark experiment calculation value should be used instead of the DSC measurement value when using Equation 25 to calculate the solar-thermal efficiency (if efficiency must be calculated). However, the inaccuracy of the results obtained through this formula cannot be ignored. Moreover, m_0 and m_g vary with sample types and experimental conditions. To some extent, the measured equivalent evaporation enthalpy is not comparable.

3.5.2. Qualitative Analysis of IW Using the DSC Method

As mentioned above, the DSC method can be used to exhibit that the state of water in an evaporation system with low evaporation enthalpy is different from that in pure water. Moreover, the DSC method simultaneously records heat flow as a function of time, and the enthalpy of evaporation is calculated by the accumulative area of normalized heat flow and evaporation time. Actually, DSC measurement can also reflect the water/ice behavior of crystallization and melting, and obtain the vaporization exothermic (or endothermic) curve of water. Combining the FW/IW/BW water model with the crystallinity of water, the crosslinked hydrophilic polymer network (e.g., polyvinyl alcohol (PVA), sodium alginate (SA), chitosan.) exhibits different water states, namely non-crystalline bound water, crystalline bound water, and bulk-like water; this is in pace with the change in matrix types and water content with different swelling degrees. They exhibit different thermodynamic properties. First, water forms a “hydrated layer” around the polymer, which is called noncrystalline water and is assigned to the BW.^[109,110] Due to the strong interaction between polar groups of hydrophilic polymers and water molecules, well-oriented hydrogen bonds are generated between polymers

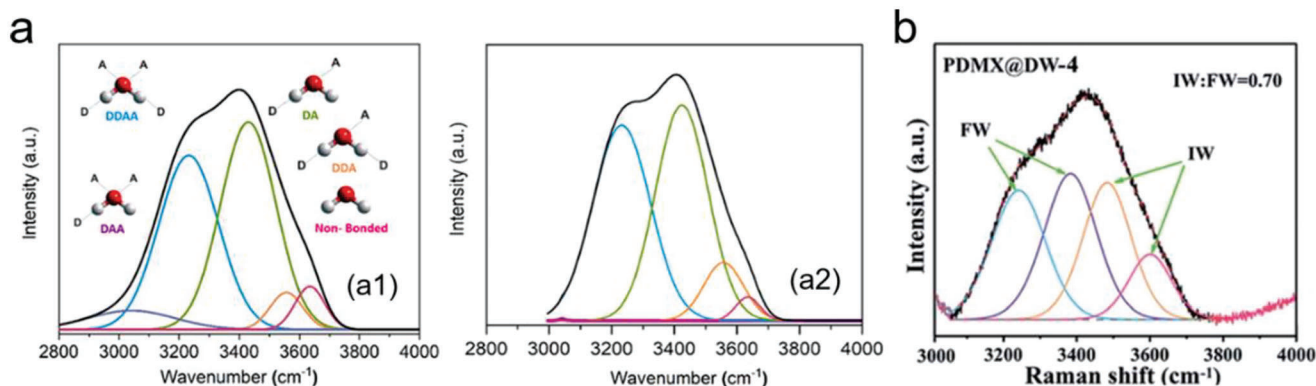


Figure 7. a) Deconvoluted vibrational band of a1) Raman spectrum of pure water and a2) normalized water in cellulose. Reproduced with permission.^[22] Copyright 2020, Elsevier. b) The O—H stretching modes of Raman spectra in PDMX@DW-4. Reproduced with permission.^[111] Copyright 2021, Royal Society of Chemistry.

and water molecules. Noncrystalline water cannot freeze even if the temperature is extremely low because this prevents water from moving to produce ice crystals during the cooling step. As a consequence, the melting point cannot be detected in DSC signals. The amount of non-crystalline water directly depends on the chemical characteristics of polar group sites. When the water content is continuously raised to the threshold of crystalline water, the content of non-crystalline water remains constant, and crystalline bound water with a melting point $>0^{\circ}\text{C}$ will appear in the matrix, corresponding to IW. Bulk-like water, which is closely connected with surrounding water molecules, presents higher water content. Water molecules cluster to form small ice crystals at 0°C , and two exothermic peaks are observed in the DSC scan. The two peaks merge to form a wider peak when the water content is further improved to a supreme swelling degree. As illustrated in Figure 6e, the BW molecules that strongly interact with polymer chains form non-crystalline water. Therefore, an endothermic peak is not observed during the test. The main endothermic peaks in the curves are categorized into the melting peaks of IW and FW.

3.5.3. Qualitative Analysis of IW Using Raman spectroscopy

Raman spectroscopy is extensively used for investigating the O—H stretching of water molecules in the hydrogen bond region and for characterizing different types of hydrogen bonds (Figure 7a,b). The vibrational band centered around 3300 cm^{-1} of water is fitted into four sub-peaks based on the Gaussian function, which can be used to analyze the change in the contents of IW and FW. These peaks are classified as follows: 1) water molecules with four hydrogen bonds, i.e., two protons and two-electron pairs, involved in hydrogen bonding, assigned to FW; 2) weakly or non-hydrogen-bonded water molecules, with cleaved hydrogen bonds in part or entirely, corresponding to IW (details from refs. 21 and 51 in the supplementary information of the paper written by Yu et al.).^[21,51] Among them, the peaks around 3200 and 3400 cm^{-1} are equivalent to in-phase bending vibration and out-of-phase vibration of FW collective aggregates, respectively. The peaks at 3500 and 3600 cm^{-1} are similar to the symmetric stretching and antisymmetric vibrations of hydro-

gen bonds formed by IW, respectively (Figure 7b).^[111] Therefore, the density percentage of water molecules in different hydrogen bonding states can be obtained by calculating the area ratio of each deconvoluted peak in the Raman spectrum.

As such, the vibrational band can be deconvoluted into five vibrational bands related to different hydrogen bond networks. Figure 7a shows the deconvolution of the Raman spectral band for cellulose.^[22] Guo's team also verified that the five peaks of the vibrational band correspond to DAA—OH (one donor and two acceptor hydrogen bonds), DDAA—OH (two donor and two acceptor hydrogen bonds), DA—OH (one donor and one acceptor hydrogen bond), DDA—OH (two donor and one acceptor hydrogen bond), and FW molecules in a super-light-absorbing system.^[58] They can form zero, three, two, four, and two hydrogen bonds, respectively. In bulk water, mainly DDAA—OH and DA—OH bonds exist, and the DA—OH bond has lower energy than DDAA—OH. Therefore, it can be transformed into other states with more hydrogen bonds.

Moreover, using both the redshift of FTIR and the decrease in the average response time of O_{17} spin-lattice as per nuclear magnetic resonance (NMR), the formation of weak hydrogen bonds can also be detected roughly (Figure 8).^[112,113]

3.5.4. Quantitative Analysis of IW

Previous studies have evaluated the quality of water in different states in water-swelling samples^[114,115] by combining the process of water steam absorption with vacuum filtration. The specific process is described in detail as follows. The quality of FW is evaluated based on the vacuum suction filtration process using a microfiltration device that specifically filters the swollen polymer saturated with liquid water, and the quality change before and after filtration is recorded as the quality of FW. The mass of hydrophilic polymer-BW is evaluated based on a water-vapor absorption experiment. Briefly, the dried polymer sample is placed in a chamber filled with water vapor, without direct contact with liquid water, so that the sample only absorbs water vapor to form polymer-BW. After the mass change reaches a steady state, the mass of BW is evaluated by increase in the sample mass. Finally, IW content is determined by evaluating the difference between

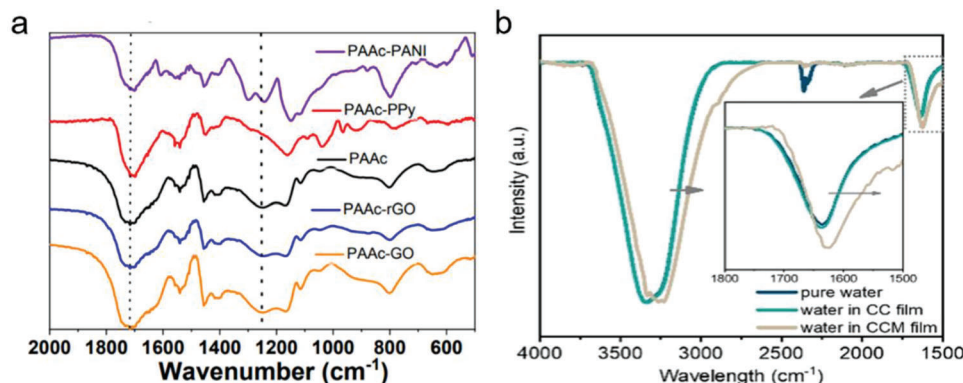


Figure 8. FTIR spectrum of a) polyacrylic acid-polypyrrole cryogels and the redshift of C=O stretching vibration. Reproduced with permission.^[112] Copyright 2021, Royal Society of Chemistry. b) Water in cellulose nanofiber and conductive metal-organic framework (CCM) film. Reproduced with permission.^[113] Copyright 2021, Royal Society of Chemistry.

the mass of the samples after water-vapor absorption and filtration processes. It is because the initial mass of the sample is the sum of the dry sample, IW, and BW masses after vacuum suction filtration, whereas the final mass is the total mass of the dry sample and BW after the water-vapor absorption experiment. Therefore, the mass of IW can be recorded by subtracting the two mass values. It is worth noting that FW is not considered in this calculation, for that BW and IW are unconnected water, whereas FW is considered connected water.^[116]

Moreover, DSC can be used to determine the ratio of IW to FW. The following formulas are summarized in order to calculate the ratio of different water types. For detailed formulas, please refer to the original text (ref. 91: “S2.2.1. DSC measurement of bound water content in h-LAHs” in the supplementary information of the paper written by Yu et al.).^[91] The vaporization enthalpy ΔH if supercooled water with melt-down temperature T is expressed as follows:

$$\Delta H(T) = \Delta H(273) - \int_T^{273} \Delta C_p dT \quad (26)$$

$\Delta H(273)$ represents the melting enthalpy of pure water, and ΔC_p is the difference in heat capacity between subcooled water and ice. Vaporization enthalpy $\Delta H(T)$ (J/g) can be estimated as follows:

$$\Delta H(T) = \Delta H(273) + 2.119 \cdot \Delta T - 0.00783 \cdot \Delta T^2 \quad (27)$$

ΔT is the temperature difference between the melt-down temperature of subcooled water (T) and the freezing point of normal water (T_{273}). Therefore, BW content (Q_B) can be calculated as follows:

$$Q_B = \left(W - \frac{\Delta Q_i^{\text{obs}}}{\Delta H(T)} \right) / W_d \quad (28)$$

W and W_d refer to the weight of water in the sample with reduced enthalpy and the corresponding dried sample, respectively, and ΔQ_i^{obs} is the experimental value of IW calculated using DSC method.

The weight of IW (w_I) fraction can be estimated as follows:

$$w_I = \Delta Q_i^{\text{obs}} / (\Delta H(T) \times w_{\text{water}}) \quad (29)$$

w_{water} represents the overall water weight.

The weight of FW (w_F) fraction can be estimated by a similar formula:

$$w_F = \Delta Q_F^{\text{obs}} / (\Delta H(T) \times w_{\text{water}}) \quad (30)$$

ΔQ_F^{obs} is the experimental value of FW.

Therefore, the weight of BW (w_B) fraction can be calculated as follows:^[91]

$$w_B = 1 - w_F - w_I \quad (31)$$

Therefore, the content of IW in the evaporation system can be roughly calculated based on water-vapor absorption and filtration processes. The ratio of different states of water can also be obtained using DSC and corresponding equations (Equations 29–31).

3.5.5. Qualitative Analysis of Water Clusters Using Nonvolatile Electrolyte Lithium Chloride (LiCl)

DSC and Raman spectroscopy qualitatively and quantitatively analyze the obvious changes in IW in the activation system, respectively. Moreover, these methods have revealed that the state of water in a WEER system is different from that of pure water. However, it is impossible to determine whether water clusters are involved in the process of water vaporization from a more microscopic point of view. To further verify the state of water (in the network) during evaporation (i.e., single water molecule or water cluster), inductively coupled plasma mass spectrometry (ICP-MS) can be used to evaluate the concentrations of ions collected from the steam in condensed water. Clustered water can capture non-volatile electrolyte LiCl;^[117–119] thus, it is added to the initial bulk water to indicate the amount of steam escaping from liquid water. In the traditional desalination system (Figure 9a),^[21] with the addition of LiCl, the concentration of Li ions in condensed

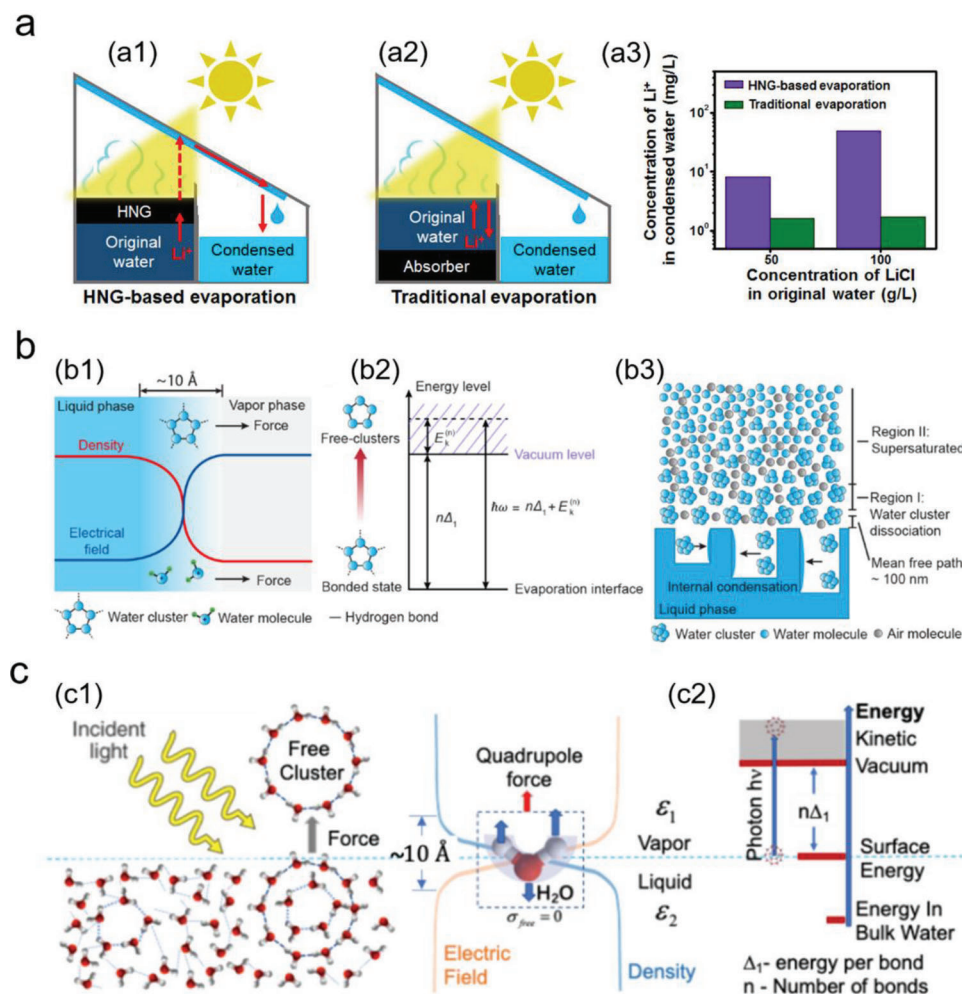


Figure 9. Schematic diagram of a1) (HNG-based evaporator and a2) traditional evaporator. a3) Concentration of Li ions in condensate obtained from LiCl solutions with different concentrations. Reproduced with permission.^[21] Copyright 2018, Springer Nature. b) Conceptual schematic of the photomolecular effect. Reproduced from "Photomolecular Effect Leading to Water Evaporation Exceeding Thermal Limit."^[55] Copyright from Yaodong Tu, Jiawei Zhou, Shaoting Lin, Mohammed AlShrah, Xuanhe Zhao, and Gang Chen. c) The photomolecular effect: c1) process and c2) energy conservation. Reproduced from "Photomolecular Effect: Visible Light Absorption at Water-Vapor Interface."^[56] Copyright from Yaodong Tu, and Gang Chen.

water did not change obviously, indicating the movement of individual water molecules. In contrast, the concentration of Li ions increased significantly in the WEER system due to the presence of several water clusters. In brief, the addition of non-volatile electrolyte LiCl to bulk water followed by ICP-MS analysis is an effective method to demonstrate the existence of water clusters.

To sum up, by integrating theoretical calculations, thermodynamic analysis, and vibration spectrum, we can obtain relevant information about water in different states and the value of equivalent evaporation enthalpy in the WEER system. However, the current research does not provide suitable methods to quantitatively analyze the influence of polar groups of various polymers on the water content in each state; hence, this should be investigated in future studies.

Chen et al. introduced a new concept related to the evaporation of water clusters. They put forward the use of the photomolecular effect in order to interpret the mechanism of water evaporation exceeding the theoretical thermal limit (Figure 9b, c).^[55] In

detail, they hypothesized that photons could cleave water clusters from the surface of the hydrogel material, which can evaporate into vapor. They further categorized the photomolecular effect into internal and external photomolecular effects, and emphasized the influence of the external photomolecular effect on the improvement of evaporation rate, whereas the internal photomolecular effect referred to the recondensation of steam when water clusters present deep in the gel were cleaved. Moreover, they suggested that the photomolecular effect depended on the wavelength of sunlight, especially at a certain wavelength in the visible-light region, as the largest water cluster could be excited at this wavelength. Therefore, high evaporation rate even beyond the theoretical thermal limit could be achieved through this system. Although the reason behind this effect has only been qualitatively explained, the effect provides another direction for investigating the thermal limit of evaporation. Based on the discovery of the photomolecular effect, Chen further introduced the concept of thermodynamic pressure into the Flory free energy theory and

re-derived the thermodynamic equilibrium conditions for the hydrogel/solution interface.^[120] The study reported that the reason behind reduction in evaporation enthalpy in the hydrogel system was due to the higher thermodynamic pressure and enthalpy of the water molecules inside it compared to that in pure water. Thus, the evaporation of the hydrogel system would be higher than the thermodynamic limit of pure water evaporation. This thermodynamic theory was another avenue that should be explored for elucidating various methods for reducing the evaporation enthalpy of hydrogel systems and encouraged the simultaneous investigation of theoretical processes and microscopic mechanisms behind the evaporation process.

In addition to focusing of the enthalpy of evaporation, Zhu's team considered optical power, evaporation rate, and enthalpy in SVG systems as important parameters.^[63] Evaporation rate is an important index to judge the evaporation performance of SVG systems. However, limited studies have established a set of standards for accurately and systematically calculating evaporation rate. We propose two main parameters for the calculation of evaporation rate. First, the evaporation area, i.e., whether the actual evaporation area or the projected area is used to calculate the evaporation rate. For 2D planar evaporators without side evaporation, the projected area of evaporator is equal to the actual evaporation area, thus excluding any scope of error in the calculation. For 3D evaporators, light absorption occurs only by the top 2D plane, whereas the actual evaporation area is not confined to just the upper surface. When the temperature of the side (vertical surface) of the evaporator is lower than the ambient temperature, additional evaporation through the side occurs absorbing by energy from the environment. In this case, the actual evaporation area is larger than the projected area of the evaporator. This suggests that the evaporation rate is inaccurate using either area; because the side of the evaporator does not absorb solar energy, the calculated evaporation rate will be lower than the actual evaporation rate. Therefore, to compare the evaporation rates of various materials, we have listed the evaporation rates calculated using two different areas in **Table 1** for reference. Among them, "ER" represents the calculated rate according to the projected area, whereas "ER" is the re-estimated rate according to the actual evaporation area. Second, whether the evaporation rate measured under light radiation conditions should be subtracted from the dark rate. This could depend on whether the temperature of the evaporation surface is lower than the ambient temperature. For photothermal absorption surfaces where the surface temperature is higher than the ambient temperature, the evaporation rate should not be subtracted from the dark evaporation rate. Conversely, for the side (vertical surface) where the surface temperature is lower than the ambient temperature, additional energy input is obtained from the environment during evaporation, so the actual evaporation rate should be calibrated by subtracting the dark evaporation rate. Therefore, we use two symbols "(+)" and "(-)" in **Table 1** to represent the evaporation rate of subtracted and un-subtracted dark evaporation rates reported in the literature, respectively.

4. Water State Adjustment

The WEER system exhibits higher steam production with low energy consumption in interfacial freshwater generation. Further-

more, the intermolecular forces and hydrogen bond network of water can be changed^[121–127] to alter its state and phase transition behavior (**Table 1**) by optimizing material selection, preparation strategy, structural regulation, and other factors, to obtain first-rank evaporation rate. In this section, we expand on the discussion of the previous section, and outline the research progress in the field of formation of IW, clustered water, and capillary water, as well as some unique structural designs of evaporators.

4.1. IW Content

Appropriate materials (including matrix and photothermal materials), elaborate structural design, and outstanding wettability properties (such as inhomogeneous wetting surface and super-hydrophilic surface) are important determinants of an SVG system, and increased IW content and lower vaporization enthalpy of the evaporation system are the two other parameters. IW content can be directly increased by using a matrix with inherent hydrophilic groups or photothermal materials, which can introduce additional hydrophilic sites to make the system hydrophilic as a whole. The polar groups of these materials form weak hydrogen bonds with the surrounding and adjacent water molecules, thus increasing the IW content. Alcohols (ROH), carboxylic acids (RCOOH), amides (RCONH₂), ketones (R₂C=O), and other materials (note: R represents other groups) are rich in hydrophilic groups, such as hydroxyl (—OH), carboxylic acid (—COOH), amine (—NH₂), sulfonic acid (—SO₃H), carbonyl (C=O), epoxy (—CH(O)CH—), and aldehyde groups (—CHO). In this section, we discuss the following five categories of materials that are equipped with a hydrophilic skeleton: polymer hydrogel/foam, cellulose hydrated membrane, carbon-involved material, biomass-based material, and other emerging skeletal materials. We also summarize the effect of the structural design of Janus/non-uniform wetted surfaces on the evaporation enthalpy. Only some representative materials/structures and their performances are listed.

4.1.1. Polymer Hydrogel/Foam

Polymer and copolymer hydrogels (**Figure 10a–g**) are potential candidates for matrix materials in seawater desalination systems ascribed to their inherent characteristics of porosity, low density, and super-hydrophilicity. Moreover, their excellent swelling property makes it possible to regulate the water state. PVA gel, which has a large number of —OH hydrophilic groups for water activation, has been widely investigated as a popular crosslinking polymer.^[12,61,62,128–133] Yu's team designed a series of SVG systems with excellent performance based on PVA and different absorbers. Owing to the interaction between —OH of PVA and water molecules, the hydrogen bond of surrounding water molecules was weakened to generate the IW, thus lowering the latent heat of water evaporation. In 2018,^[21] they added a polypyrrole (PPy) absorber into the PVA matrix to form an HNG network and reported that upon changing the weight ratio of PVA to water, the state of water in the porous hydrogel could be regulated. Ultimately, the optimal HNG-3 exhibited an unprecedented vapor generation rate of 3.2 kg m⁻² h⁻¹. Furthermore, considering

Table 1. Summary of water activation materials/structures (Notes: “IW clusters” represent the system combining mechanism I (IW) and mechanism II (clustered water). Two symbols “(+)” and “(-)” in represent the evaporation rate of subtracted and un-subtracted dark evaporation, respectively).

Structure/materials of evaporator	Enthalpy [J g^{-1}]	DSC measurement vs Selected theoretical value	Equivalent enthalpy [J g^{-1}]	ER [$\text{kg m}^{-2} \text{h}^{-1}$]	ER' [$\text{kg m}^{-2} \text{h}^{-1}$]	η	Water activation	Refs.
Hybrid hydrogel evaporators (HHE) based on KGM and PVA	2401/2450		1548.3 \pm 39.2	1015.1 \pm 57.3	3.200 ⁽⁺⁾	90.0%	IW	[134]
Corn stalk-based solar steam generators	/ \approx 2400		—	930.00	2.480 ⁽⁺⁾	68.2%	IW	[164]
Fe ₃ O ₄ /PVA decorated delignified wood evaporator	—		—	—	1.300 ⁽⁻⁾	73.0%	IW	[159]
Highly hydratable light-absorbing hydrogel (h-LAH) consisting of PVA, chitosan, PPy	2432/2450		1659.93	—	3.600 ⁽⁺⁾	92.0%	IW	[91]
Hydrated cellulose network	2436/2440		2096.00	1915.00	2.080 ⁽⁺⁾	93.6%	IW	[111]
Chitosan (CS)/cuttlefish ink (CI) hydrogel evaporation device	/2398.8		—	640.480	3.685 ⁽⁻⁾	72.9%	IW	[137]
Fallen-leaf photothermal film prepared by dehydration (FLPD)	2273/		1211.00	—	1.355 ⁽⁻⁾	—	IW	[165]
Hierarchical photothermal fabrics as heliotropic evaporators	2432.4/2406.17		1827.16	1956.32	2.270 ⁽⁻⁾	90.2%	IW	[174]
Ni-based plasmonic/magnetic nanostructures evaporator	—		—	1884.00	2.250 ⁽⁺⁾	95.0%	IW	[12]
Hydrophilic hydrogel evaporators with hydrophobic island-shaped patches	—		—	<1000.00	4.000 ⁽⁻⁾	93.0%	IW	[52]
MoS ₂ /SA@MF hybrid sponge	/2441.7		—	1618.00	1.920 ⁽⁺⁾	90.0%	IW	[57]
Biowaste-derived carbonized bone	—		—	—	1.820 ⁽⁻⁾	80.0%	IW	[110]
Cu _{2-x} S NRs-PVA gel	—		—	—	1.270 ⁻	87.0%	IW	[128]
Reduced graphene oxide/Ti ₃ C ₂ T _x MXene hybrid hydrogel	2363/2260		1921.00	1791.00	2.090 ⁽⁻⁾	93.5%	IW	[150]
Squid ink-starch hydrogel	—		—	\approx 1750.00	2.070 ⁽⁺⁾	93.7%	IW	[167]
Vertically aligned acetate fibers (VAAFs)@CDs-T	—		—	1301.00	2.600 ⁽⁻⁾	93.9%	IW	[156]
Bacterial cellulose (BC) nanocomposites coating on wood	/2450		—	1810.00	2.900 ⁽⁻⁾	80.0%	IW	[108]
H _x MoO ₃ /PNIPAM hydrogel	—		1873.53	—	1.050 ⁽⁻⁾	85.9%	IW	[140]
Hybrid hydrogels with capillarity facilitated water transport (CTH)	—		—	\approx 1400.00	2.500 ⁽⁺⁾	95.0%	IW	[51]
(3D) tree-shaped PVA/PPy hydrogel membrane	2424/2450		1735.00	\approx 1000.00	3.640 ⁽⁺⁾	96.0%	IW	[61]
Ion activated hierarchically porous polyion complex hydrogels	/2440		—	1783.00	2.790 ⁽⁺⁾	96.3%	IW	[145]
Tree-inspired MXene-PVA hydrogel (TIH)	2403/2450		1624.00	1205 \pm 35	2.710 ⁽⁺⁾	90.7%	IW	[130]
Light-absorbing sponge-like hydrogel (LASH)	2422/2450		1553.00	924 \pm 106	3.600 ⁽⁻⁾	89.0%	IW	[131]
UIO-66-COOH/CNTs@PCMVIM (UCP-x) membranes	2407/		1309.00	1329.00	2.560 ⁽⁺⁾	80.2%	IW	[106]
Nanofibrous hydrogel-RCO (NH ₂ C) membrane	2310/		1967.00	—	1.850 ⁽⁺⁾	95.4%	IW	[99]
BNC-based bilayer photothermal foam (PTFb)	2307/		1870.00	—	1.710 ⁽⁻⁾	84.3%	IW	[157]
Dimpled surface PVA hydrogel	—		—	\approx 1250.00	2.600 ⁽⁻⁾	91.0%	IW	[179]
Ag@PDA NPs on the wood flower	/2411.83		—	1678.09	2.080 ⁽⁻⁾	97.0%	IW	[141]
ACET/PAM/SA-LN hydrogel	2997/		2300.00	—	1.640 ⁽⁺⁾	93.0%	IW	[139]
3D-printed hydratable plastics	2450/2420.3		1850.00	710.00	3.010 ⁽⁺⁾	—	IW	[22]
Nanoink-stained PVA evaporator	—		—	—	2.150 ⁽⁻⁾	—	IW	[224]
Assembly of carbon dots within processed wood	—		—	—	2.270 ⁽⁻⁾	92.5%	IW	[155]

(Continued)

Table 1. (Continued).

Structure/materials of evaporator	Enthalpy [J g ⁻¹]	Equivalent enthalpy [J g ⁻¹]		ER [kg m ⁻² h ⁻¹]	η	Water activation	Refs.
		DSC measurement	Dark experiment				
PPy-Fe ₃ O ₄ -CTS nanostructured gel membrane	—	—	—	1.930 ⁽ⁱ⁾	—	IW	[135]
COF/graphene dual-region hydrogel	2362/2450	1043.1±27.1	1043.00	3.690 ⁽⁺⁾	92.0%	IW	[178]
Bionic solar evaporator	/2487	—	1541.00	2.300 ⁽⁺⁾	93.0%	IW	[121]
Feather-like MXene aerogels	—	—	1732.00	0.920 ⁽ⁱ⁾	88.5% (0.5 sun)	IW	[129]
Hierarchically porous radiation-absorbing hydrogel film (hp-RAH)	—	—	—	1.983 ⁽⁺⁾	95.0%	IW	[122]
PPy/PVA-F Janus aerogel	2460/	2110.00	2030.00	1.680 ⁽⁺⁾	94.7%	IW	[132]
Interpenetrating polymer networks gel (IPNG)	2435/2450	1571.00	860.00	3.860 ⁽⁺⁾	92.0%	IW	[143]
PVA/SLS-CNT hydrogel	2375/2432	1525.00	1654.00	2.090 ⁽⁺⁾	—	IW	[125]
Coconut husk photothermal material	/2450	—	1441.00	1.830 ⁽ⁱ⁾	73.2%	IW	[170]
Candle-derived carbon nanoparticle/wood hybrid	/2434	—	1696.00	2.060 ⁽⁺⁾	90.0%	IW	[163]
Anionic polyelectrolyte-based hydrogel (APH)	/2420.49	—	1624.14	2.500 ⁽⁺⁾	90.7%	IW	[126]
MOF-functionalized-wood solar evaporator	/2260	—	1146.00	2.700 ⁽⁺⁾	—	IW	[173]
Lignin hydrogel-based solar-driven evaporator	/2450	—	<1500.00	2.250 ⁽ⁱ⁾	91.6%	IW	[225]
Ti ₃ C ₂ T _x MXene/rGO hydrogels (MRHs)	2450/	≈1100.00	—	3.620 ⁽ⁱ⁾	91.0%	IW	[133]
Graphene oxides on MS sponge	2450/	1032.00	—	3.470 ⁽ⁱ⁾	97.4%	IW	[127]
In-air calcinated melamine sponges (AMS)	/2256	—	1846.00	1.980 ⁽⁺⁾	92.0%	Clusters	[180]
Super-wicking and super-light-absorbing (SWSA) aluminum solar panel	/2440	—	1220±19	1.260 ⁽⁺⁾	—	Clusters	[58]
Sandwich membrane structure with confined hierarchical carbon cells	—	—	—	1.870 ⁽⁺⁾	81.8%	Clusters	[217]
All-day solar-driven vapor generator based on metal foam (CuO/Cu-CB foam)	2320.9–2417/	1991.81	—	1.650 ⁽⁺⁾	96.7%	Clusters	[185]
Hybrid semiconductor confined in mesoporous glass	2160/2260	1670.00	—	1.750 ⁽⁺⁾	80.0%	Clusters	[197]
Hydrophobic Ni-C-WO _{3-x} solar-driven interfacial evaporator	—	—	—	2.120 ⁽⁺⁾	85.0%	Clusters	[184]
Lotus morphology-inspired biomimetic evaporator (MBE)	2487/2444	1846.00	1643.00	1.597 ⁽⁺⁾	74.2%	Clusters	[59]
MoS ₂ nanosheet-carbon foam composites	/2260	889.00	—	1.490 ⁽ⁱ⁾	88.3%	Clusters	[188]
Cellulose nanofiber@conductive metal-organic framework (CCM) film	—	—	—	2.420 ⁽ⁱ⁾	—	Clusters	[113]
Nanoconfined water molecule channels (NCWMCs)	2329/2423	1562.00	1246.00	2.500 ⁽⁺⁾	89.6%	Clusters	[213]
AuNPs@C-silica/filter fiber paper (FFP) (GSP) membrane	/2432	—	2151.00	1.500 ⁽ⁱ⁾	94.6%	Clusters	[192]
PCL/CNTs and PCL/CNPs composite thin film	—	—	—	1.950 ⁽ⁱ⁾	81.2%	Clusters	[193]
Carbonized corn-cob-based 3D solar vapor steam generator	2406/	1774.00	—	4.160 ⁽ⁱ⁾	> 100.0%	Clusters	[189]
Copper foam (CF)-supported 3D nanosheets array composed of ternary Ni-Co-Cu chalcogenides	/2430	—	1376.00	2.480 ⁽ⁱ⁾	99.0%	Clusters	[186]

(Continued)

Table 1. (Continued).

Structure/materials of evaporator	Enthalpy [J g^{-1}]	DSC measurement vs Selected theoretical value	Equivalent enthalpy [J g^{-1}]		ER [$\text{kg m}^{-2} \text{h}^{-1}$]	ER' [$\text{kg m}^{-2} \text{h}^{-1}$]	η	Water activation	Refs.
			DSC measurement	Dark experiment					
Paper-based CuCAT-1 MOF nanorod arrays/gelatin (PCG) membrane	2283/2257		1912.00	—	1.510 ⁽⁺⁾	1.510	80.2%	Clusters	[194]
Manure-derived photothermal evaporator	—		—	1276.00	2.810 ⁽⁺⁾	2.810	94.7%	Clusters	[60]
Laser-induced photothermal generation of monolithic bilayer membranes	—		—	1845.00	1.330 ⁽⁺⁾	1.330	68.2%	Clusters	[183]
TiO ₂ @TiN hyperbranched nanowires-carbonized wood	2355/2355		2148.00	2156.78	1.520 ⁽⁺⁾	1.240	94.0%	Clusters	[214]
Ag NPs within 3D carbonized melamine foams (CMF)	/2256		1964.30	—	2.120 ⁽⁺⁾	2.120	103.0%	Clusters	[181]
Laser-processed cotton paper	—		—	—	1.711 ⁽⁺⁾	1.711	83.0%	Clusters	[191]
Double-layer cellulose hydrogel	—		1935.00	—	1.582 ⁽⁺⁾	1.582	91.4%	Clusters	[198]
Hollow multishelled structure (HoMS)	2328/		1491.00	—	4.020 ⁽⁺⁾	—	—	Clusters	[201]
Fe–Mo ₂ S ₃ based evaporation system	—		—	1370.00	2.400 ⁽⁺⁾	—	91.4%	Clusters	[199]
Rice husk biochar-based porous hydrogel (RHB-PH)	/2441.7		—	1981.00	1.770 ⁽⁺⁾	1.770	94.0%	Clusters	[208]
Zwitterionic hydrogel on porous PU fabric	—		—	≈1500.00	2.200 ⁽⁺⁾	2.20	93.5%	Clusters	[200]
3D origami solar steam generator	—		—	—	1.590 ⁽⁺⁾	1.370	≈100.0%	Clusters	[209]
3D dyed cotton towel foam	—		—	—	1.400 ⁽⁺⁾	0.720	96.7%	Clusters	[215]
Multilayer polypyrrole nanosheets	2452/		2403.00	—	1.380 ⁽⁺⁾	1.380	95.3%	Clusters	[212]
Carbonized bamboos	2477/2444		1519.00	—	3.130 ⁽⁺⁾	—	132.0%	Clusters	[211]
Carbonized tree-like furry magnolia fruit-based evaporator	2450/2444		1503.00	—	2.280 ⁽⁺⁾	—	90.1%	Clusters	[107]
Zr(Ti)O ₂ nanotube membranes with aligned channels	—		—	1555.00	1.040 ⁽⁺⁾	1.040	70.8%	Clusters	[216]
Black sponge treated nitric acid	/2444		—	1081.00	2.720 ⁽⁺⁾	—	—	Clusters	[218]
3D dual-functional solar-thermal evaporators	—		—	800.00	6.800 ⁽⁺⁾	2.040	—	Clusters	[205]
CNT–PAAm–conical aerogel	/2444		—	683.00	2.230 ⁽⁺⁾	0.720	—	Clusters	[202]
Green moss evaporator	/2442		—	1957.00	2.610 ⁽⁺⁾	2.610	69.0%	Clusters	[190]
Three-Level pore structure hydrogels (TLPSHs)	2397/2440		—	1923.00	1.650 ⁽⁺⁾	1.650	≈80.0%	Clusters	[206]
Pico-second laser treated aluminum (PLAL) surface	/2440		—	541.25±0.07	1.240 ⁽⁺⁾	1.240	67.0%	Clusters	[203]
Carbonized willow catkins films	2163/2257		1422.00	—	2.170 ⁽⁺⁾	—	136.0%	Clusters	[210]
3D evaporator improved by solar-induced air-flow updraft	/2450		—	1806.80	3.540 ⁽⁺⁾	3.040	95.9%	Clusters	[204]
Hierarchically nanostructured gel (HNG) based on PVA and PPY	2417 vs 2444		1919.00	≈1300.00	3.200 ⁽⁺⁾	3.200	94.0%	IW clusters	[21]
MnO ₂ nanowires/chitosan hydrogels (SPM–CH)	—		—	—	1.780 ⁽⁺⁾	—	90.6%	IW clusters	[136]
CFs@CDs hydrogel-stabilized solar evaporator	2401/2440		1501.00	1453.00	2.320 ⁽⁺⁾	2.320	93.6%	IW clusters	[169]
PCMVImTf ₂ N/CNT/UiO-66-COOH membrane	/2400		—	1330.00	2.300 ⁽⁺⁾	—	—	IW clusters	[171]
GO/CNT@PIL (GCP) membrane	/2390		1910.00	1990.00	1.870 ⁽⁺⁾	1.870	79.2%	IW clusters	[151]
PAN/CNTs nanofiber based aerogels	/2256		—	1819.50	2.130 ⁽⁺⁾	2.130	94.5%	IW clusters	[138]
Reduced graphene oxide hydrogel membrane (rGOHM)	—		—	—	2.330 ⁽⁺⁾	2.330	—	IW clusters	[149]
PAAc–PPy cryogel	—		—	—	1.819 ⁽⁺⁾	1.819	≈100.0%	IW clusters	[112]

(Continued)

Table 1. (Continued).

Structure/materials of evaporator	Enthalpy [J g ⁻¹]	Equivalent enthalpy [J g ⁻¹]		ER [kg m ⁻² h ⁻¹]	η	Water activation	Refs.
		DSC measurement	Dark experiment				
Sea urchin-like carbon from metal-organic frameworks	/2430	–	1810.00	2.070 ⁽⁺⁾	91.5%	IW clusters	[160]
Nitrogen-doped maize straw/graphene aerogel	2417/2444	1659.00	878.00	3.220 ⁽⁺⁾	95.0%	IW clusters	[103]
Bilayered black MoS ₂ @PEI/MCE	2369/2444	1462.00	–	1.000 ⁽⁺⁾	92.0% (3.7 sun)	IW clusters	[195]
Cu ₁ S _x -MoS ₂ -Au (CMA)-PDMS system	–	–	910.00	3.824 ⁽⁺⁾	96.6%	IW clusters	[142]
Expanded graphite (EGr) enmeshed within PU and PSA polymer	–	–	≈1750.00	1.890 ⁽⁺⁾	92.7%	IW clusters	[116]
Wood-based devices by pTsOH-assisted hydrothermal treatment (W-SSGDs)	2444/	1860.00	–	2.200 ⁽⁺⁾	87.0%	IW clusters	[161]
Porous carbon/pulp fiber (PCP-x) hybrid membranes	/2422	–	2087.00	1.800 ⁽⁺⁾	87.6%	IW clusters	[158]
Ag-PSS-AG/AG device	–	–	1591.12	2.100 ⁽⁺⁾	92.8%	IW clusters	[104]
Biomimetic hydrophilic foam with hydrophobic surface	–	–	–	3.090 ⁽⁺⁾	98.0%	IW clusters	[220]
Polyester-derived porous carbon-coated wood evaporator	/2434	–	1427.00	2.380 ⁽⁺⁾	–	IW clusters	[162]
N ₂ O dual-doped carbon foam	/2434	–	1524.00	2.400 ⁽⁺⁾	83.8%	IW clusters	[219]
MoS ₂ @GH photothermal self-pumping system	2394/	2250.00	–	3.200 ⁽⁺⁾ (0.9 sun)	–	IW clusters	[207]
Wood-based 3D solar evaporator	2444/	1769.00	–	1.930 ⁽⁺⁾	–	Capillary water	[222]
Carbonized cattail (CCT) evaporator	2458/2444	1545.00	–	4.120 ⁽⁺⁾	105.8%	Capillary water	[166]
Hollow carbonized cotton microfibers (HCMFs)	/2256	–	1066.32	2.170-	92.0%	Capillary water	[221]
Injection control technique for carbon-based material	–	–	≈1800.00	2.400 ⁽⁺⁾	99.4%	Capillary water	[54]

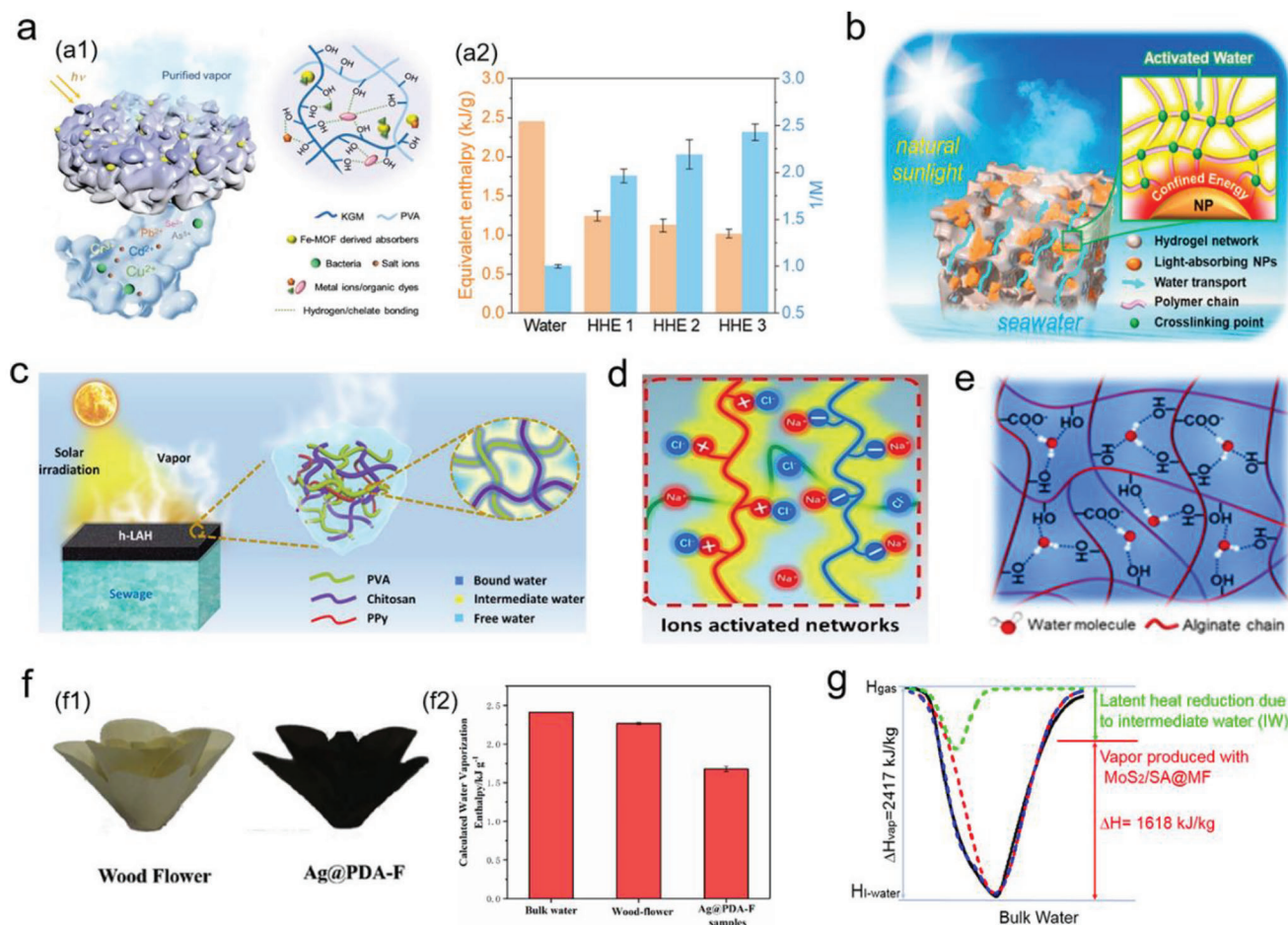


Figure 10. Polymer hydrogel/foam. a1) Schematic diagram depicting the functional mechanism of hybrid hydrogel evaporators (HHEs) and adsorption of ions. a2) The water vaporization rate ratio ($1/M$) of HHEs under dark conditions and corresponding equivalent enthalpy. Reproduced with permission.^[134] Copyright 2020, Wiley-VCH. Schematic illustration of the functional mechanism of b) the LASH evaporator comprising Ti_2O_3 nanoparticles and PVA and c) the h-LAH-based evaporator consisting of PPy absorbers and PVA-chitosan matrix. Reproduced with permission.^[131] Copyright 2019, American Chemical Society. Reproduced with permission.^[91] Copyright 2019, American Association for the Advancement of Science. d) Three states of water in hierarchical porous hydrogel (HPH) marked with different colors. Reproduced with permission.^[145] Copyright 2020, Royal Society of Chemistry. e) Schematic diagram of hydrogen bonding between functional groups and water molecules in hypercrosslinked polymeric networks (HPN). Reproduced with permission.^[79] Copyright 2022, Wiley-VCH. f1) Photographs of untreated pure wood flowers and plasma wood flowers, and f2) equivalent enthalpy of evaporation obtained under dark experimental conditions. Reproduced with permission.^[141] Copyright 2020, Elsevier. g) Differential scanning calorimetry (DSC) curve and fitting curve of $\text{MoS}_2/\text{SA}@\text{MF}$ hybrid sponge. Reproduced with permission.^[57] Copyright 2021, Elsevier.

the aggravation of heat diffusion loss due to polymer absorbers, they proposed the replacement of dispersive polymers with Ti_2O_3 nanoparticles as the solar absorber and fabricated a sponge-like gel, denoted as LASH (Figure 10b).^[131] The design presented in the LASH gave full play to the synergistic effect of energy management and water regulation because it confined the heat energy on the surface, decreased the content of heated bulk water, and lowered the equivalent enthalpy values to 1553 kJ kg^{-1} (as per the DSC method). Therefore, the evaporation rate of this system increased to $3.6 \text{ kg m}^{-2} \text{ h}^{-1}$, which was more prominent than that of other SVG evaporators. In addition, a hybrid hydrogel evaporator named HHE with excellent performance was developed (Figure 10a).^[134] The $-\text{OH}$ of PVA and konjac glucomannan matrix in the HHE can not only improve the hydration ability and further reduce latent heat of evaporation, but also excess $-\text{OH}$

can form chelate bonds with heavy metal ions, thus realizing the removal of heavy metal ions and the degradation of organic dyes.

Recently, various hydrophilic polymers such as chitosan,^[135–138] SA,^[57,79,139] AG,^[104] polyacrylamide (PAM),^[139] isopropyl acrylamide (PNIPAM),^[140] polydopamine (PDA),^[138,141] polyacrylic acid (PAAc),^[112,142] poly sodium acrylate (PSA),^[116] etc.^[143,144] have been used to adjust the state of water. Xiao et al. prepared $\text{MoS}_2/\text{SA}@\text{melamine foam}$ ($\text{MoS}_2/\text{SA}@\text{MF}$) hybrid sponge (Figure 10g),^[57] in which SA hydrogel firmly fixed MoS_2 nanoflowers on the MF even after the flushing-through test for 30 days and improves hydrophilicity; its inherent $-\text{OH}$ and $-\text{COOH}$ groups increased the IW ratio of the skeleton and reduced the latent heat of water. Inspired by the fact that the $-\text{COOH}$ groups of PAAc can activate water

molecules, PAAc-PPy cryogel, a low-temperature gel, was developed by He's team.^[112] This cryogel generated higher levels of IW, which made evaporation easier. Moreover, its $-\text{COOH}$ groups could form hydrogen bonds with polar functional groups of photothermal materials, ensuring uniform distribution and good combination of photothermal materials. Chen et al. loaded silver nanoparticles coated with dopamine on wooden flowers (Figure 10f) and fabricated an evaporator material called Ag@PDA-F, which exhibited high efficiency of 97.0% and an evaporation enthalpy of $1678.09 \text{ kJ kg}^{-1}$; this can be attributed to polar groups of PDA. Similarly, Zhou's group fabricated a light-absorbing hybrid polymer hydrogel, termed h-LAH, using chitosan and PVA as the hydration skeleton (Figure 10c).^[91] h-LAH5 exhibited minimum latent heat, but its evaporation rate and efficiency were lower than those of h-LAH4 because otopot saturated water content increased energy demand for heating bulk water instead of evaporating interface water. Subsequently, the surface temperature of h-LAH5 rose slowly. Thus, they established that only evaporation enthalpy could not be considered a standard to measure vaporization performance of the WEER system. Other factors, such as the saturated water content of samples and surface temperature response time, should be comprehensively discussed.

It is worth mentioning that polyelectrolyte gels with ionizable groups are also used in SVG systems. Taking advantage of its ability to capture counter ions in the solution, Zhu et al. complexed negatively charged poly(sodium *p*-styrenesulfonate) (PNaSS) and positively charged poly(3-(methacryloylamino)propyltrimethylammonium chloride) (PMPTC) into a polyion composite gel (PIC hydrogel).^[145] Then, the polyaniline (PAni) absorber was polymerized in situ and crosslinked by acrylic acid to prepare hierarchical porous hydrogel (HPH). The interaction between oppositely charged polyions and mobile ions in the brine regulated the state of water (Figure 10d), endowing PICs with admirable hydration ability, thus increased amount of IW was generated. The IW:FW of HPH in 3.5 wt% brine was approximately 0.5, whereas the ratio in bulk water was only 0.21. Raman spectroscopy elucidated that under different salt concentrations, water is activated on the basis of the ions trapped by a polymer with opposite charge, but the degree of activation is distinct. This is because the ion-modified hydration property of the gel depends on the competitive interactions between PIC-water and ion-water. As the salt concentration increases, the ion-water interactions become dominant, and IW content slightly decreases. Recently, Yu's team proposed a super water-extracting gel (SWEG) for removing VOCs, which was fundamentally different from traditional hydrogels.^[79] The SWEG could directly separate VOCs and water at the molecular level to regulate the water content of the gel, thus high content of FW could be avoided and energy requirement for water evaporation can be lowered. This was because the gel is rich in $-\text{OH}$ and $-\text{COOH}$ groups, which could form strong hydrogen bonds with water molecules; therefore, the water molecules formed weak hydrogen bonds with their adjacent water molecules (Figure 10e). These examples demonstrate that polymer gels can produce higher amount of activated water and accelerate liquid dynamics, thus provide a new way to develop next generation SVG systems in possession of enhanced desalination performance.

4.1.2. Carbon-Based Materials

Several types of carbon-based materials have been developed due to the abundance of carbon in nature; different types of carbon-based materials with high sunlight absorption ability and low cost are available. These properties of carbon-based materials enable SVG systems to achieve high evaporation rates. Therefore, they have been used in solar-powered interfacial desalination systems (Figure 11a–e). To date, many relevant comprehensive reviews are present on this topic.^[146–148] Similar to hydrophilic gels, carbon-based materials (especially reduced graphene oxide (rGO); Figure 11b) can facilitate IW formation due to their $-\text{OH}$ and $\text{C}=\text{O}$ polar groups and can reduce the evaporation energy demand. rGO hydrogels,^[149] rGO/PVA composite gels,^[51] and rGO/MXene hybrid gels^[150] also reduce the evaporation enthalpy of water. For instance, Zang et al. developed a hybrid membrane based on nanofibrous hydrogel-rGO (NHRG) by mixing rGO flakes in the nanofiber network instead of depositing them on the surface of the membrane (Figure 11a).^[99] They observed that the ratio of IW in the NHRG membrane gradually increased because of the presence of oxygen-containing functional groups of GO and the narrow surface area of rGO sheets. Moreover, with increased GO loading, more oxygen-containing groups become available and form weakly hydrogen-bonded water molecules, thus lowering the evaporation enthalpy of the hybrid film. Furthermore, the introduction of rGO nanosheets produced a more limiting surface, reduced the size of large cavities and created a usable nano space, which contributed to the generation of IW. To understand the underlying mechanisms responsible for regulating interfacial vaporization, Zang *et al.* investigated the functional relationship between saturated water content in the membrane and the change in evaporation enthalpy; if IW and FW had an equal chance of evaporation at the interface of the membrane, the measured enthalpy of evaporation should increase as the saturated water content of the membrane increases. However, the evaporation enthalpy basically remained unchanged for 10–90% saturated water content, but varied with GO loading in the NHRG membrane, and was lower than that of bulk water. Thus, IW evaporation has higher priority than FW evaporation. Additionally, carbon nanotubes (CNTs) have been extensively investigated because of their particular photothermal conversion ability and large specific surface area. Although CNTs do not possess $-\text{OH}$ groups on their surface, they exhibit the absorbance ability of light-thermal materials and expose more channels for evaporation (by reason of a larger effective area), which reduces the challenges faced in water evaporation in SVG systems. Han and co-workers developed a sandwiched GO/CNT@PIL (GCP) membrane (Figure 11c1), demonstrating the great potential to interlink CNTs and GO.^[151] Compared to that in bulk water, the number of hydrogen bonds in the GCP membrane decreased, and the distance between the bonds increased (Figure 11c2,c3). CNTs also provided more evaporation space for water fluid. Moreover, the energy demand was 20% lesser than that of vaporization energy typically required in bulk water in the GCP membrane.

Recently, 0D carbon dots (CDs) with multiple oxygen-related groups on the surface, fabricated by selective etching of warm coal pitch ultrafine powder, have attracted attention. Unlike 2D graphene and CNTs, CDs possess specific structural defects and heteroatoms that endow them with lower thermal conductivity,

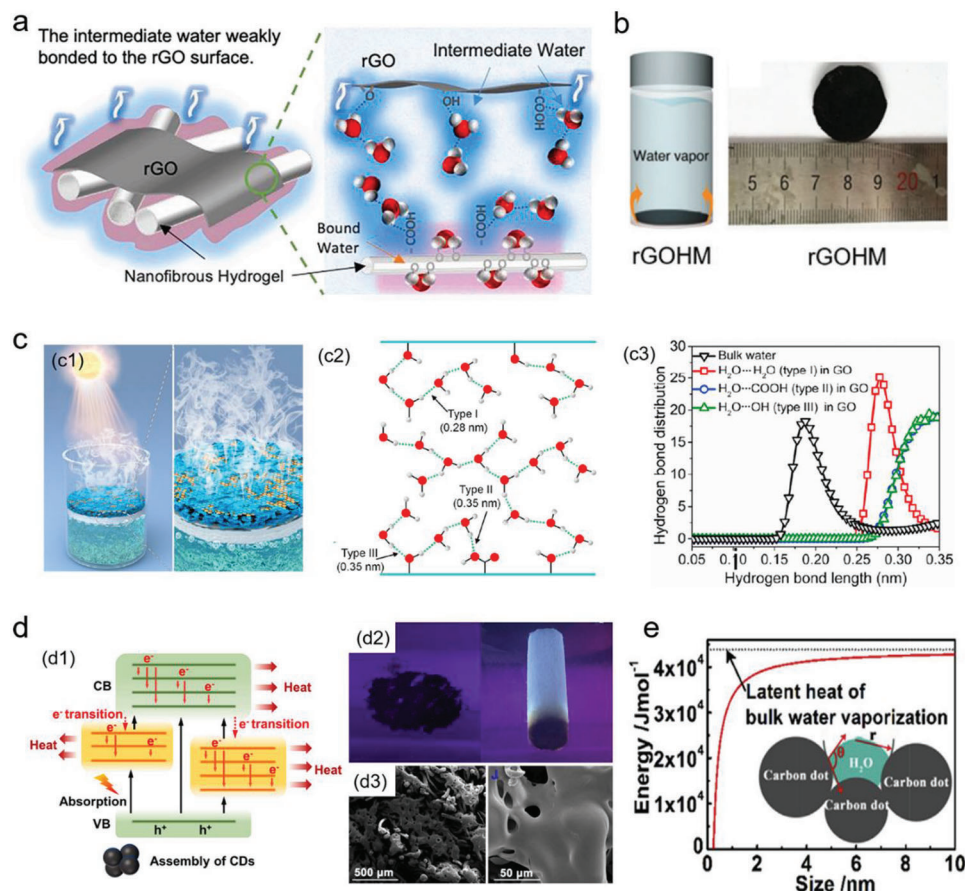


Figure 11. Carbon-based materials. a) Structure of NHRG membrane and its water activation mechanism. Reproduced with permission.^[99] Copyright 2021, Elsevier. b) Image of rGO hydrogel membrane. Reproduced with permission.^[149] Copyright 2020, Wiley-VCH. c) Activation mechanism of c1) GCP-x interfacial evaporation membranes, c2) hydrogen bonding configurations between GO nanosheets, and c3) radial distribution functions of different types of hydrogen bond lengths. Reproduced with permission.^[151] Copyright 2021, Elsevier. d) Schematic illustrations of d1) electronic-level structures of CD assemblies, d2) CDs and VAAFs@CDs under UV lamp, and d3) top view of VAAFs@CDs-T using scanning electron microscopy (SEM). Reproduced with permission.^[156] Copyright 2021, Elsevier. e) Latent heat curve with respect to pore size. The inset shows that the water around CD is confined in a narrow nano space. Reproduced with permission.^[155] Copyright 2019, Elsevier.

which can be exploited to minimize heat conduction losses in SVG systems. The photothermal principle of CDs resembles that of semiconductor quantum dots. During the assembly of CDs, a series of new sub-energy levels are generated at the interface due to the interaction between oxygen-containing groups on the surface. Electrons are induced to produce non-radiative recombination centers that quench fluorescence and release energy, thus successfully realizing photothermal conversion.^[152–154] Hou et al. assembled CDs with processed wood to prepare CDs@wood evaporator.^[155] The surface of the CDs contains polar groups such as $-\text{OH}$, $-\text{COOH}$, and $\text{C}=\text{O}$, and the rough surface inside the wood was beneficial for the adhesion of the CDs. The evaporator was equipped with a double-layered thermal insulation, water transmission path, and could synchronously achieve efficient photothermal conversion rate of carbon spots. Another research group exploited benzoic anhydride (BA), phenyl hydrazine (PH), and 2-bromo-1-phenylethanone (BrPE) to selectively remove $-\text{OH}$, $\text{C}=\text{O}$, and $-\text{COOH}$ groups, respectively, to investigate the effect of different oxygen-containing groups on minimizing the vaporization enthalpy. They reported that the mass

change of the CDs/BA after removing the $-\text{OH}$ groups could be more obviously compared with that of CDs/PH and CDs/BrPE, which validated that $-\text{OH}$ groups played an indispensable role in evaporation. Ulteriorly, oxygen atoms were eliminated from disparate oxygen-related functional groups using deoxidizer N_2H_4 , and it was found that the mass change was more significant. Therefore, the content of oxygen atoms in $-\text{OH}$ groups acted as a determinant of evaporation performance of a material. Besides, in line of the classical phase transition theory of surface tension-guided pressure, the team considered additional pressure of nano-size induced droplets passing through the curved interface. CDs induced the formation of smaller pore diameter (as indicated in Equation 18 in Section 3.1) and decreases evaporation enthalpy (Figure 11e). In 2021, Hua's team made use of the hydration structure of acetate fiber and the shell composed of oxygen-containing groups around the surface of CDs, which led to increased formation of weakly hydrogen-bonded IW, and the evaporation enthalpy was only 1301 kJ kg^{-1} under dark experiments (Figure 11d).^[156] However, very less attention has been paid to the application of CDs in lowering the vaporization

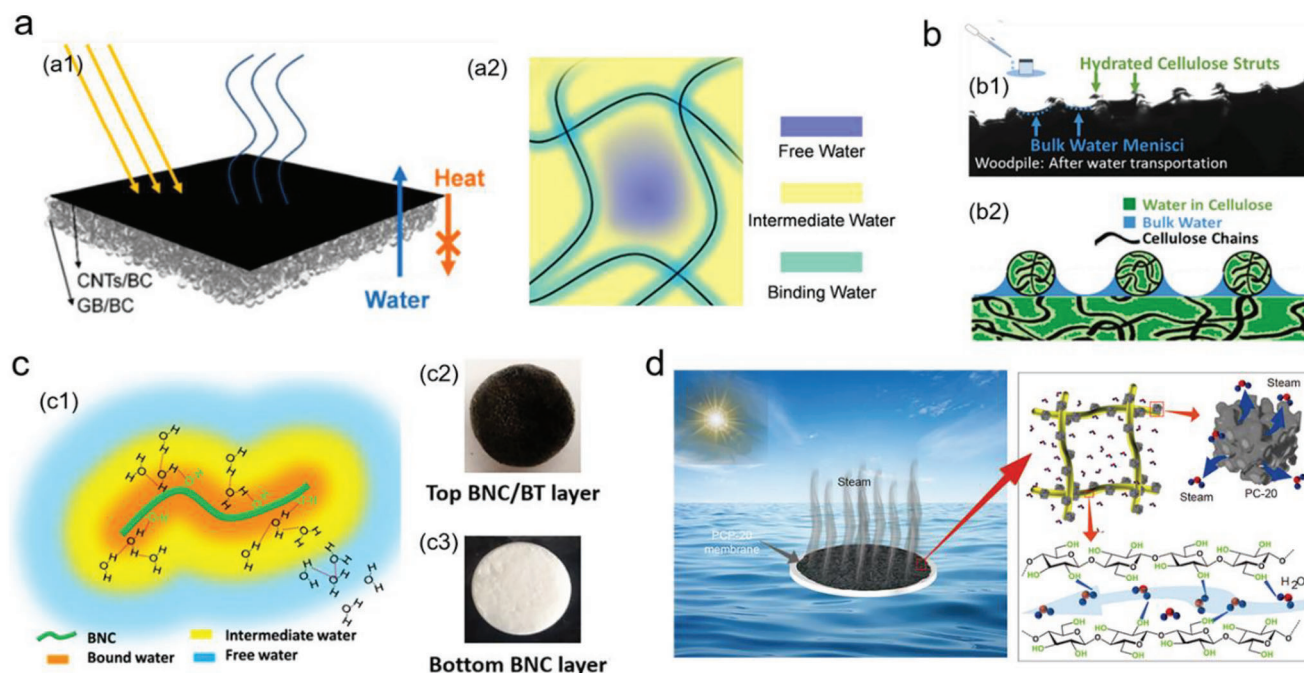


Figure 12. Cellulose hydrated membrane. a) Schematic illustration of a) HSSG device and a2) different states of water molecules and their modes of bonding in the CNTs/BC network. Reproduced with permission.^[108] Copyright 2020, American Chemical Society. b) Horizontal view of Woodpile's surface b1) after absorbing water and b2) after water transportation. Reproduced with permission.^[22] Copyright 2020, Elsevier. c) Diagram of c1) water activation mechanism for IW generation in BNC hydrogel, c2) top BNC/black titania (BNC/BT) composite layer for light absorption, and c3) bottom pure BC layer. Reproduced with permission.^[157] Copyright 2021, American Chemical Society. d) Schematic representation of vapor generation system of porous carbon/pulp fiber-20 (PCP-20) membrane and connection between water molecule and paper pulp fiber. Reproduced with permission.^[158] Copyright 2022, Springer Nature.

enthalpy triggered by $-\text{OH}$ and $-\text{COOH}$ groups; therefore, further comprehensive investigation is required to exploit the advantages of CDs in developing efficient SVGs.

4.1.3. Cellulose Hydrated Membrane

Previous sections establish that the major focus in this field is on modifying hydrophilic polymer gel/foam; however, cellulose membranes (Figure 12a–d) have not been sufficiently investigated. Similar to porous polymer hydrogel, fibrous hydration materials (such as acetate fibers) are inherently highly hydrated. In detail, a myriad of scientists has proposed that more $-\text{OH}$ groups can be obtained from bacterial nanocellulose (BNC) and cellulose acetate to form activated water, which permits water to evaporate at a lower energy cost. Compared with polymers that decompose and wrinkle easily under high solar power density, cellulose has a robust structure with higher mechanical stability, which guarantees the durability of an SVG system. In 2020, Yu's team designed a layered structure called HSSG using the aerosol-assisted biosynthesis method (Figure 12a).^[108] They reported that the introduction of bacterial cellulose (BC) hydrogel could decrease the evaporation enthalpy of water to 997 J g^{-1} , which was 60% lower than that of pure water. Furthermore, the content of weakly hydrogen-bonded IW in BC hydrogel was as high as 69%, which significantly weakened the hydrogen bonds between IW molecules and reduced the overall energy requirement for the water evaporation process. Similarly, Nabeela et al.

embedded black titania into BNC and fabricated a double-layered hydrogel named PTFb (Figure 12c), which reduced the latent heat of evaporation due to the BNC–water interactions.^[157]

Apart from this, Hao et al. developed porous carbon/pulp fiber (PCP- x) hybrid membranes with $-\text{OH}$ group-rich pulp fibers (Figure 12d) and reported that the membrane considerably reduced evaporation enthalpy by virtue of the IW generated via hydrophilic $-\text{OH}$ groups.^[158] Moreover, Koh et al. deacetylated ethyl acetate to obtain regenerated cellulose, which promoted a hydrated structure to produce more $-\text{OH}$ groups (Figure 12b).^[22] The water molecules exhibited more order locally, resulting in higher number of weak hydrogen bonds in the hydrated and regenerated cellulose than in bulk water. Higher number of $-\text{OH}$ hydrophilic surface functionalities made the cellulose network extremely susceptible to becoming hydratable and generated higher IW levels. Moreover, fibrous materials could overcome the disadvantage of poor performance of polymer hydrogel structure under high solar flux; therefore, cellulose hydrated membranes should be the focus of studies on evaporator development in the future.

4.1.4. Biomass-Based Evaporator

In order to settle the challenge of expensive and complicated preparation of photothermal materials, plenty of low-cost materials receive immense interest used as alternatives (Figure 13a–g). Recently, several studies have investigated biomass materials,

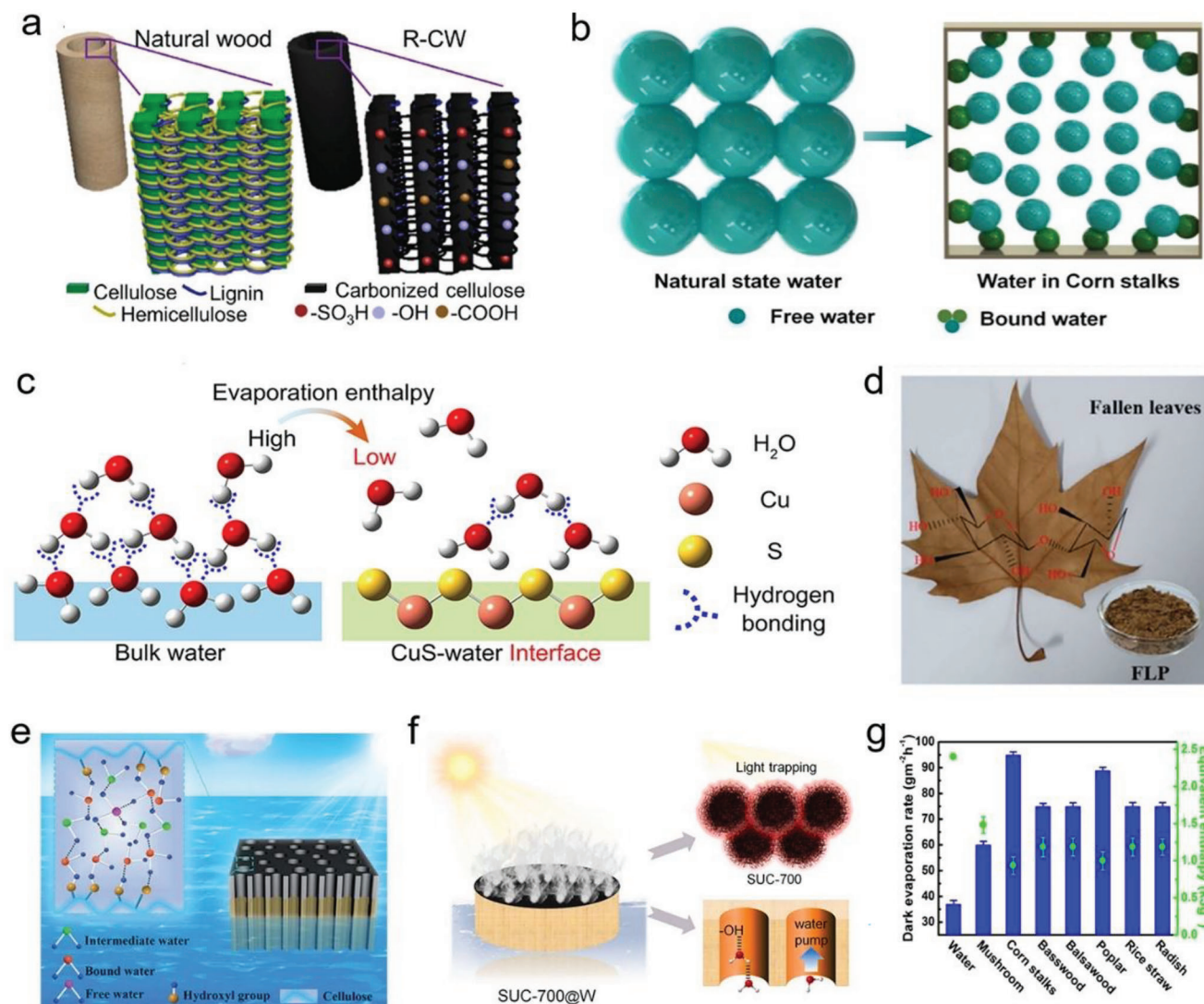


Figure 13. Biomass-based and other skeletal materials for evaporators. a) Diagram of natural wood and p-TsOH-catalyzed wood after hydrothermal treatment. The treated wood contains more hydrophilic functional groups, such as $\text{—SO}_3\text{H}$, —OH , and —COOH , promoting water activation. Reproduced with permission.^[161] Copyright 2020, Elsevier. b) Schematic representation of the existing forms of normal water molecules and activated water molecules in corn stalks, accompanied by the change of distance. Reproduced with permission.^[164] Copyright 2020, Royal Society of Chemistry. c) Evaporation enthalpy reduction mechanism in hierarchical PAN@CuS fabric. Reproduced with permission.^[174] Copyright 2021, American Chemical Society. d) Hydrophilic groups in a leaf. Reproduced with permission.^[165] Copyright 2020, Wiley-VCH. e) Structure of PDMX@DW and its water activation mechanism. Reproduced with permission.^[111] Copyright 2021, Royal Society of Chemistry. f) Schematic diagram of wood-based interfacial water evaporator named SUC-700@W. Reproduced with permission.^[160] Copyright 2021, Elsevier. g) Statistics of equivalent enthalpy and evaporation rate of water in biomass materials under dark evaporation experiment conditions. Reproduced with permission.^[164] Copyright 2020, Royal Society of Chemistry.

including wood (Figure 13f),^[111,159–163] corn stalks (Figure 13b),^[164] leaves (Figure 13d),^[165] cattail,^[166] bones,^[110] cuttlefish ink,^[167] and sucrose,^[168] and other biomass^[169,170] (Figure 13g), which are being used as burgeoning materials. Different types of synthesis methods such as alkali treatment, delignification, carbonation, oxygen plasma catalysis, and acid treatment can be used to enhance the hydrophilic functionalities of the raw material.

Generally speaking, untreated wood is composed of cellulose, hemicellulose, and lignin, where the mutual repulsion of hydrophobic lignin makes it difficult for water to enter the pores of the fibers to form evaporative IW. Therefore, the orig-

inal wood cell wall is delignified using sodium hydroxide solution or by the hydrothermal method to expose hydrophilic —OH— and —COOH— groups containing cellulose, which is beneficial to the formation of weak hydrogen bonds and decreases the water vaporization enthalpy. At this point, Chen et al. integrated PDA, MXene, and delignified wood (DW) with a high-cellulose skeleton to obtain a hierarchical evaporator (PDMX@DW; Figure 13e).^[111] The hydrophilic —OH— polar groups within delignified wood could interplay with water molecules and change the hydrogen-bonded state of water, thus allowing water to evaporate at a lower energy cost. It turned out that easily disconnected hydrogen-bonding IW

triggered by PDMX@DW was the origin of decreasing evaporation enthalpy. In another study,^[161] hydrothermal treatment with p-toluenesulfonic acid (pTsOH) was performed to lower vaporization enthalpy (1860 J g^{-1}) because the treatment exposed several polar hydrophilic functionalities such as $-\text{OH}$, $-\text{SO}_3\text{H}$, and $-\text{COOH}$ (Figure 13a), which directly reduced the water vaporization enthalpy of wood. Besides wood, the combination of $-\text{OH}$ groups of corn stalk (Figure 13b) and water molecules weakened the Van der Waals force between other water molecules and reduced the energy needed to form water vapor. These studies suggest that in future, low-cost, environment-friendly, and easy-to-prepare biomass/biowaste-based materials will be used for reducing the energy required to form water vapor.

4.1.5. Other Skeletal Materials

Other skeletal materials, such as metal-organic frameworks (MOFs), MXene and CuS, also exhibit unique potential in enhancing the performance of SVG systems. MOFs have a typical porous network structure, hydrophilic functional groups, and adjustable compositional/structural properties; they have recently attracted attention in various functional applications because of their vaporization enthalpy.^[171–173] The MOF-based membrane prepared by Dong et al. utilized the $-\text{COOH}$ functional groups of UiO-66-COOH to form interfacial hydrogen bonds with low evaporation energy, which was attributed to the increase in bond length and the decrease in the number of hydrogen bonds.^[106] The vaporization energy required for pure water was 2.4 kJ g^{-1} whereas the latent heat of the evaporator was only 1.3 kJ g^{-1} , indicating that the MOF-based evaporator could activate more water molecules with the same energy input. Additionally, Chen's team skillfully designed a photothermal fabric with low evaporation enthalpy and constructed a heliotropic phototaxis evaporator using CuS nanosheets (Figure 13c).^[174] Specifically, the evaporator was always perpendicular to the incident light, which ensured that the projected area was equivalent to the exposed surface area and increased the sunlight absorption ability of the system. In this core hierarchical photothermal fabric, the insertion of CuS broke the original hydrogen-bond network of water molecules, the sulfur atoms of CuS were exposed at the ridge, and the copper atoms were embedded in the grooves. Compared with the hydrogen bonding among oxygen atoms and water molecules in bulk water, the hydrogen bonding between sulfur atoms and water molecules in this optimized evaporator were weaker, thus reducing the evaporation enthalpy of water to 1956 J g^{-1} , which was 81.5% of that of the bulk water. Molecular dynamics simulation exhibited that the water was trapped in grooves due to electrostatic interactions and interface characteristics. An IW layer was formed above the water-sulfur interface, which further verified the contribution of CuS to lowering evaporation energy. Many other MXene composites contain hydrophilic groups and exhibit the same potential as the above materials.^[175]

Therefore, in this section, we introduce different kinds of materials that can reduce the enthalpy of evaporation and describe some representative studies in detail (as displayed in Table 1). These studies establish that hydrophilic functional groups such as $-\text{OH}$ could regulate the activation energy based on weakly bonded water molecules, thus reducing the energy needed for

evaporation. Furthermore, it is evident that appropriate matrix and the relationship between the matrix and water molecules are essential criteria for improving the evaporation performance of SVG systems. As such, we should pay careful attention to the fact that the material with the lowest evaporation enthalpy may not bring out the most miraculous evaporation performance, and it is impossible to draw a definite and comprehensive conclusion only by the enthalpy of evaporation. Because water evaporation performance of a system depends on several other factors. For example, in case of a hydrogel matrix, the state of water in the gel is dependent on many factors, such as polymer structure, crosslinking density, polymer concentration, and saturated water content.^[97] Therefore, a balance among these parameters should be achieved to ensure high evaporation performance.

Although considerable progress has been made in enhancing the evaporation performance of SVG systems, structural design of these systems needs further research to achieve optimum performance. Here, we briefly analyze representative studies on wettability and surface morphology (Figure 14a–c), which play an essential role in the WEER system. In recent years, inspired by the lotus leaf structure, the effective exploration and practice of Janus wettability configuration has attracted attention. The Janus structure captures solar light and transports water in two different layers. The upper hydrophobic photo-to-thermal layer is used for energy conversion and vapor generation, and the bottom layer continuously pumps bulk water to the confined evaporation surface. By virtue of its hydrophilicity and the double-layered structure, the Janus line was introduced, which is the boundary line between the hydrophilic layer and the hydrophobic layer. According to Wan et al., the length of Janus lines and the capillary size of the hydrophobic layer surface were directly proportional to the water evaporation rate.^[176] Compared with single wettability feature in previous seawater desalination systems, the Janus structure presented higher vaporization rate with the same conversion efficiency and energy input. For example, the bionic Janus evaporator named lotus morphology-inspired biomimetic evaporator (MBE), developed by Yu's team,^[59] combined the Janus wettability design with bimodal porous structure and exhibited low evaporation enthalpy (1846 J g^{-1}). Zhang et al. also developed a Janus membrane in which the molar ratio of IW to FW was as high as 0.84 in the wet state.^[177] The generation of higher levels of activated water lowered the energy required for evaporation. A hydrophilic PDA layer could help the Janus membrane in regulating the state of water confined in the polymer and determining the volume of water to be pumped. Simultaneously, the hydrophobic layer could ensure appropriate vapor flux and exhibit the anti-pollution ability by rectifying the structural parameters (tortuosity, thickness, porosity, pore diameter). The synergistic effect of the Janus configuration maintained the equilibrium between water replenishment and vapor production, which was of great importance for maximizing the evaporation rate. Therefore, the design of the Janus structure separates water evaporation and water supply processes. The addition of a hydrophobic layer not only served as a valve for water supply, but also played an anti-pollution role, which was indirectly conducive to the evaporation rate. In addition to the advanced Janus wettability design, Yu's team modified local trichlorosilane (OTS) on the basis of a previous study on PVA hydrogel and designed a special island-like inhomogeneous wetting surface with hydrophobic patches

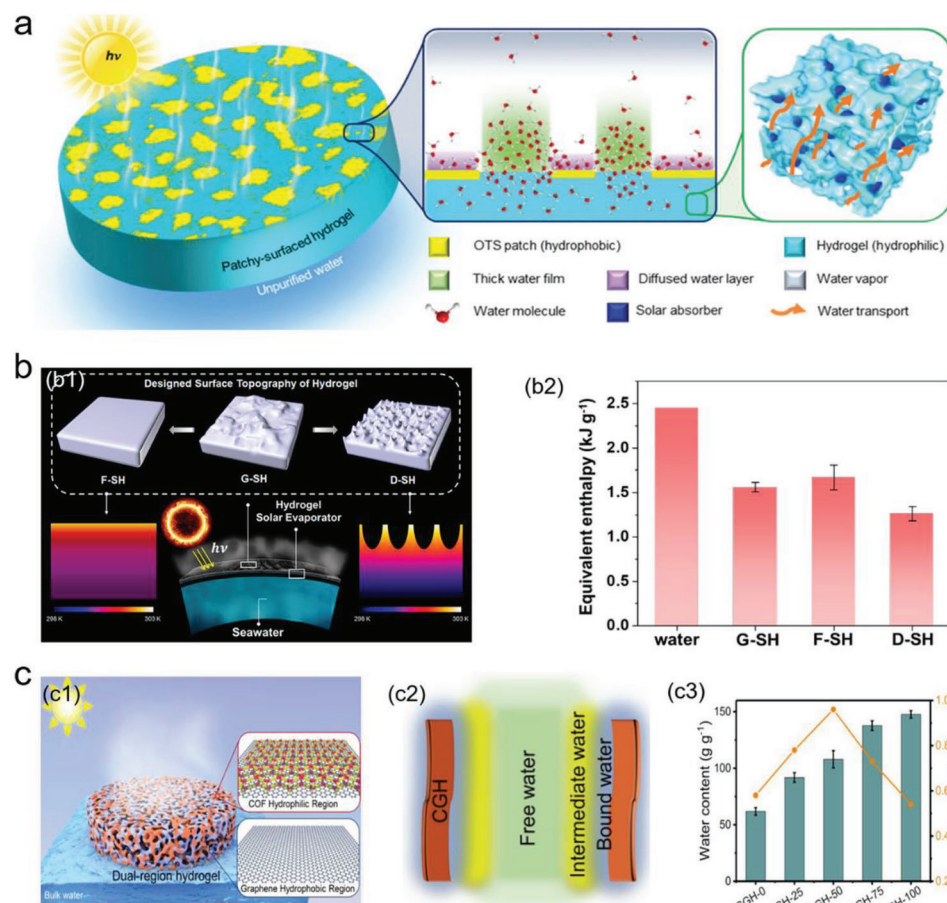


Figure 14. Special structural designs. a) Schematic diagram of solar steam generation, water transportation, and water layer distribution in patch-shaped gels. Reproduced with permission.^[52] Copyright 2020, Royal Society of Chemistry. b) Surface topography-tailored hydrogel: b1) solar vapor generation mechanism and b2) comparison of equivalent enthalpy of bulk water and activated water confined in flat-surface, grooved-surface, and dimpled-surface hydrogels. Reproduced with permission.^[179] Copyright 2019, American Chemical Society. c) COF/graphene dual-region hydrogel: c1) schematic diagram of solar-powered water evaporation and internal structure, c2) three states of water, c3) water content and the ratio of IW and FW in COF/graphene dual-region hydrogels. Reproduced with permission.^[178] Copyright 2022, American Chemical Society.

(Figure 14a).^[52] The hydrogel was called patchy-surface hydrogels (PSHs), and its latent heat value was $<1000 \text{ J g}^{-1}$, which was lower than the evaporation enthalpy of pure water (about 2400 J g^{-1}). The significantly reduced energy requirements could be explained by the following two points: First, as described in the previous Chapter 4.1.1, PVA hydrogel contains several hydrophilic $-\text{OH}$ functional groups, which can form easily evaporated IW. Second, the structural design of OTS. As shown in the Figure 14a, OTS provides the finishing point so that evaporated water can originate from the water layer located in the hydrophilic region as well as the diffused water layer in the contact zone of the hydrophilic/hydrophobic region; most of the water is confined to the hydrophilic area, increasing the thickness of the outermost water film. This causes the diffusion of water molecules to the water contact line with low interfacial energy. The number of water molecules on the elongated contact line increases, making it easier to form water vapor. In this unique wetting surface, the constant adjustment among water film thickness, hydrophilic area, and contact line length produces high evaporation rate (approximately $4.0 \text{ kg m}^{-2} \text{ h}^{-1}$). Recently, Li et al. devel-

oped a dual-region hydrogel evaporator based on covalent organic framework (COF)/graphene using the green synthesis method (in-situ growth). The hydrogel consisted of a hydrophilic COF-loaded rGO (COF@rGO) region and a hydrophobic pure rGO region (Figure 14c1).^[178] The hydrophilic $-\text{SO}_3\text{H}/-\text{SO}_3^-$ functionalities of the COF in the dual-region hydrogel network (denoted as CGH-based hydrogel) enabled the regulation of water content. Increase in COF@rGO content not only enhanced hydrophilicity to produce more IW, but also extended the macropore size to generate high amount of FW (Figure 14c2,c3). Therefore, the systematic optimization of the proportion of these two regions was responsible for adjustable capillary channel size and the wettability feature of this gel. Thus, the hydrogel could further optimize the water content and regulate the state of water to realize low energy expenditure of water evaporation (1043 J g^{-1} in the dark evaporation test).

Recently, the focus on wettability designs has increased; however, the use of surface topography design to significantly reduce the enthalpy of evaporation needs further elucidation. For example, the sharply dimpled surface topography proposed by

Guo et al. (Figure 14b1) could centralize solar energy to increase heat flux and reduce energy loss,^[179] which was unlike that observed for flat and grooved surfaces. Most importantly, the dimpled topography exhibited reduced equivalent enthalpy of evaporation (1250 J g^{-1} ; Figure 14b2). Therefore, evaporator surface morphology and their wetting properties need to be further explored, as the optimization of these two parameters is emerging as an innovative and advantageous way to overcome the existing stagnant low evaporation rate bottlenecks of SVG systems.

4.2. Clustered Water

Porosity is an essential parameter of SVG systems, and many researchers have developed porous materials with lower latent heat of evaporation than the theoretical value. These materials include treated porous melamine foam,^[180,181] polyurethane sponge,^[182] polyimide sponge,^[183] porous nickel foam,^[184] copper foam,^[185,186] bio-carbon foam,^[60,187–190] fiber membrane,^[91,106,169,191–196] mesoporous glass,^[197] hydrogels,^[91,104,136,149,198–200] and others.^[201–204] In accordance with the water cluster theory,^[100,101] a water cluster surrounded by several water molecules is susceptible to escape from the surrounding liquid water for evaporation. It is owing to the fact that the average energy required by each molecule in the water cluster is lower than that of a single water molecule when evaporating the multi-molecule water cluster. The evaporation process of water clusters with low energy requirements involves the breakage of only the adjacent hydrogen bonds with the surrounding liquid. Therefore, water clusters exhibit significantly reduced vaporization enthalpy compared with pure water. Porous structure not only provides a favorable water transport channel in the SVG system, but also increases the effective evaporation surface area and allows the formation of large-size water clusters with low evaporation enthalpy. At present, several researchers have designed multi-scale pore assemblies of micropores/mesopores/macropores or narrow restricted pore spaces.^[162] Hao and his collaborators reported a bio-carbon/pulp fiber hybrid membrane with multi-scale pore,^[158] which divided bulk water into many small clusters by taking advantage of the confined space effect in the porous structure. During the formation process, the micro/medium/large pores were constructed by mixing the coacervation salt as a pore-forming agent. Hence the pore formation and surface area were regulated by regulating the amount of salt. The results of this study elucidated that these clusters lowered the density of hydrogen bonds, which in turn reduced the overall energy requirement in vapor generation.

In this section, we summarize two strategies for forming clusters, namely, constructing bimodal/multi-scale hierarchical pores and creating confined nanospace. Based on these two strategies, some remarkable works have been explored and developed.

4.2.1. Hierarchical Pores

Hierarchical pores suggest that the pores have changed from single-size structure to bimodal or multi-scale structure. The hierarchical pore-channel comprises 3D tightly connected macropores along with mesopores and nanopores embedded in the

macropores. Such a specific pore structure not only provides more channels for airflow and exhibits good heat regulation, but more importantly, it may exert an influence on the evaporation process by inducing the formation of more water molecular clusters with low latent heat of evaporation, leading to a reduction in evaporation energy (Figure 15a–f).^[205–207] The MBE evaporator (as mentioned in Section 4.1.5) proposed by Yu's team possessed the representative advantages of both Janus wettability surface and double-peaked pores (Figure 15a).^[59] The 3D brush-shaped macropores and lotus root-shaped mesopores arranged in parallel guaranteed adequate transportation of bulk water, rapid overflow of vapor, and facilitated the reduction of water evaporation energy. To elucidate the influence of bimodal porous structure on the state of water, they compared the DSC thermograms of samples under two different wetting modes. One method was continual shaking so that pure water was in complete contact with the sample. The second method was direct dripping into the sample. In this case, due to the distribution of hydrophobic upper layer/hydrophilic lower layer of MBE, a proportion of water did not penetrate into the bimodal hydrophilic pores of the lower layer, but floated independently on the hydrophobic surface of the upper layer. The shaking wetting method led to a lower enthalpy of evaporation due to the differential effects of wetting on the hydrogen bonds of the water clusters. Therefore, this verified that bimodal pores played an important role in lowering the water vaporization enthalpy. Moreover, with the help of the bimodal pores, MBE exhibited increased effective evaporation area, which allowed more energy absorption from the environment for faster evaporation. Similarly, the foam-like porous hydrogel employed by Chen et al. took full advantage of bimodal hydrophilic porous structure for reducing evaporation energy to activate evaporation.^[208] Another design is the multiscale pore channel, which improves the hierarchical porosity. In 2018, Yu's group proposed a PPy/PVA-based hydrogel with multi-scale structure,^[21] which included internal gaps (approximately 150 microns; Figure 15h1) for water pumping, micron channels (several to tens of microns, Figure 15h2) providing branch water diffusion paths, and molecular mesh as evaporation base of small-sized water clusters; this system was the first to present a hierarchical porous nanostructure with a clear division of labor. By regulating the ratio of PPy/PVA, it is possible to determine the nanostructure of the hydrogel and further control saturated water content in the system. They also expounded the reduction of evaporation enthalpy through evaporation experiment, DSC, and thermodynamics analysis. Furthermore, they measured the change in LiCl content in traditional evaporation and HNG-based evaporation systems (as mentioned in Chapter 1) using ICP-MS analysis. Experiments revealed that the lithium ion concentration in the non-volatile electrolyte was different before and after evaporation. Moreover, based on the theory of molecular clusters, several water molecular clusters evaporated in this HNG-based evaporator. Wang et al. fabricated a similar structure utilizing the gas-foaming method (Figure 15g),^[142] which promoted the production of abundant IW and water clusters; this system also exhibited low evaporation enthalpy. Therefore, when water is confined in porous hierarchical structure, it is more likely to evaporate as small clusters of molecules containing small amounts of water instead as individual water molecules directly, which is accordance with the main goal of WEER systems.^[209–211]

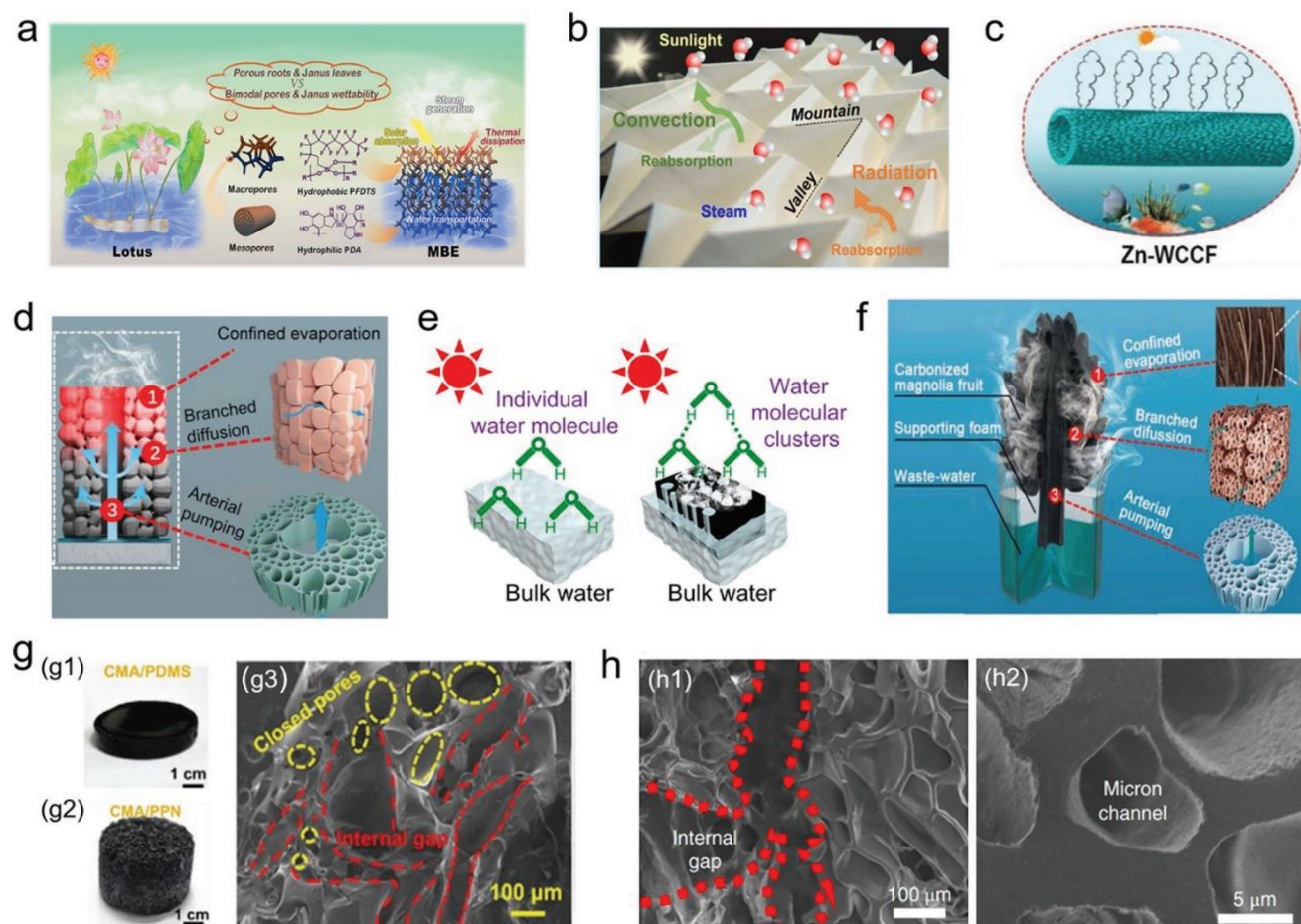


Figure 15. Hierarchical pore configurations for formation of clustered water. a) Lotus morphology-inspired evaporator for accelerating solar water evaporation. Reproduced with permission.^[59] Copyright 2020, Elsevier. b) Origami-structured evaporator for vapor generation. Reproduced with permission.^[209] Copyright 2018, American Chemical Society. c) Zn-decorated hollow carbon fiber containing molecular clusters in pores. Reproduced with permission.^[210] Copyright 2021, Wiley-VCH. d) Carbonized bamboo evaporator for rapid evaporation. The hierarchical pore structure can be used for replenishing water clusters. Reproduced with permission.^[211] Copyright 2019, Wiley-VCH. e) Schematic diagram of evaporation of single water molecule and clustered water molecules in treated wood. Reproduced with permission.^[161] Copyright 2020, Elsevier. f) Schematic representation of carbonized melamine foam-based evaporator with hierarchical pores. Reproduced with permission.^[107] Copyright 2019, Wiley-VCH. g) Photographs of g1) $\text{Cu}_7\text{S}_4\text{-MoS}_2\text{-Au/polydimethylsiloxane}$ (CMA/PDMS), and g2) CMA/porous photothermal nanostructure (CMA/PPN) using gas-foaming preparation methods, g3) SEM images of CMA/PPN. Reproduced with permission.^[142] Copyright 2020, Wiley-VCH. h) The internal gap and micron channel of HNG-based evaporator. Reproduced with permission.^[21] Copyright 2018, Springer Nature.

4.2.2. Confined Nanospace

Some other materials based on nanospace confinement also play a major role in the formation of water molecular clusters (Figure 16a–h).^[210] In nature, plants are the best example of this process. The hierarchical structure, pits, and directional pore-channels of bamboo can provide excellent advantages for water delivery, and the formed bamboo mesh after high-temperature carbonization can evaporate water molecules as a cluster in the molecular mesh.^[211] Magnolia, known as a mini tree, also produces a fruit mesh after carbonization. Water molecules are confined in the fruit mesh, thus several molecular clusters containing water molecules of a few to tens are formed.^[107] As such, the wood that exhibited smaller lumens after treatment also activated the formation of IW and water clusters,^[161] thus developed narrow nano-confined spaces (Figure 16c).

The nanospace or nanocracks generated among nanosheets (Figure 16f),^[209,212,213] nanowires,^[214] nanopores,^[113,215] and nanotube arrays (Figure 16d)^[216] can reduce the evaporation enthalpy. The nanocellulose@MOFs developed by Zhou et al. could also reduce the enthalpy of evaporation.^[113] This could be because the nanopores in the layered porous framework provide conditions for water confinement (Figure 16e). Similarly, the cracks formed between nanosheets become essential sites for the generation of water clusters. Lu et al. formed confined water-molecule nanochannels between O-doped MoS_{2-x} nanosheets (called NCWMC system), which were approximately 3.5 nm in space size and could reduce vaporization energy by evaporating water clusters (Figure 16b1).^[213] In molecular dynamics simulation, their NCWMC system evaporated more water molecules at different accelerations (Figure 16b2), which was consistent with the experimental results and reflected the cluster

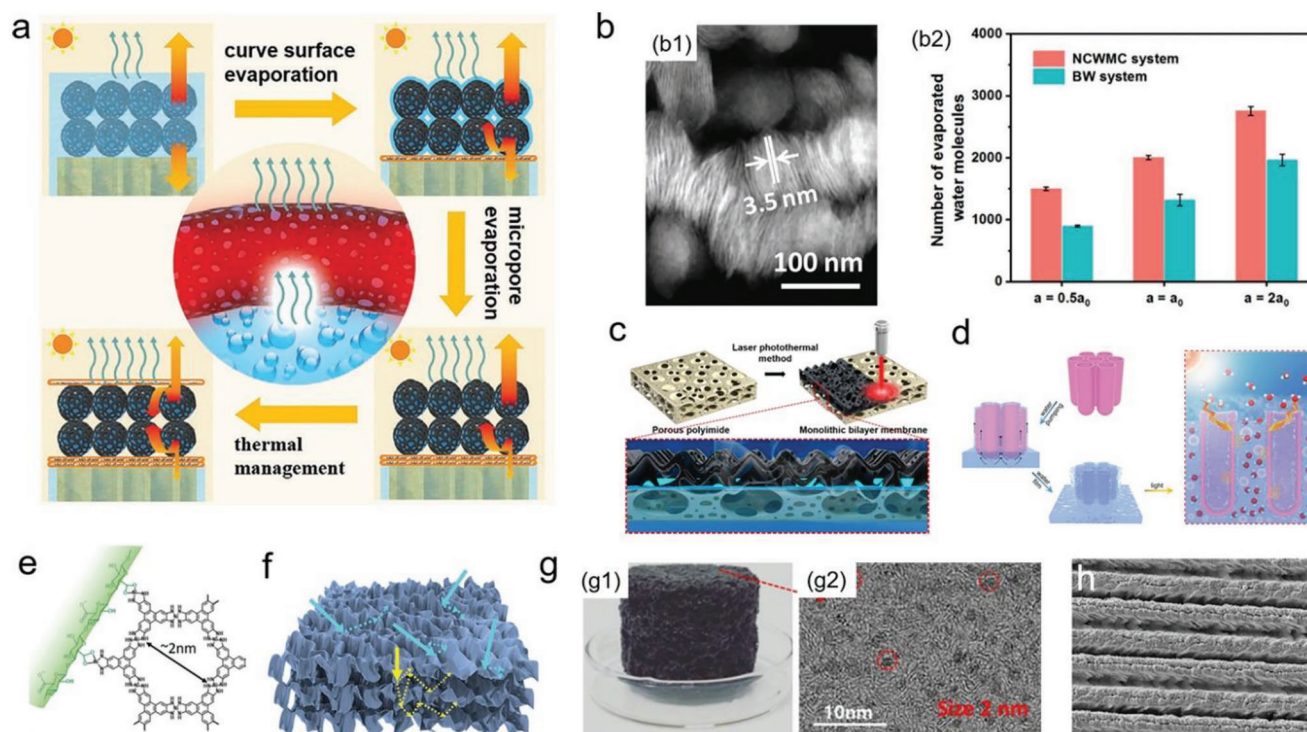


Figure 16. Confined nanospace for accelerating clustered water formation. a) Regulation of evaporation mode of different sandwich membrane structures: change from curved evaporation mode to microporous evaporation mode. Reproduced with permission.^[217] Copyright 2020, Wiley-VCH. b) Nanoconfined water channels: b1) scanning transmission electron microscopy (STEM) image of 1D-OMoSNSA, showing the 3.5 nm nanospace and b2) comparison of the number of evaporated water molecules in molecular dynamics simulations. Reproduced with permission.^[213] Copyright 2020, Wiley-VCH. c) Schematic illustration of the functional mechanism of laser-induced photothermal evaporator with wavelike porous structure. Reproduced with permission.^[183] Copyright 2020, Elsevier. d) 3D water films surrounding Zr(Ti)O₂ nanotube. Reproduced with permission.^[216] Copyright 2019, Royal Society of Chemistry. e) Molecular structure of a membrane composed of MOF and cellulose nanofiber. Reproduced with permission.^[113] Copyright 2021, Royal Society of Chemistry. f) Schematic illustration of functional mechanism of multilayer PPy nanosheets. Reproduced with permission.^[212] Copyright 2019, Wiley-VCH. g1) Photograph of the top position of nitric acid treated black sponge (NBS), and g2) the high resolution transmission electron microscope (HRTEM) images of residual potassium chloride (KCl) in the pores. Reproduced with permission.^[218] Copyright 2019, Royal Society of Chemistry. h) SEM images of the super-light-absorbing (SWSA) sheet with hierarchical structures. Reproduced with permission.^[58] Copyright 2020, Springer Nature.

evaporation pattern of water molecules in this system. In the sandwich membrane structure (Figure 16a) designed by Tian et al.,^[217] the enthalpy of evaporation was approximately 24% lower than that of pure water, which was also due to the change from surface evaporation to micropore evaporation. According to their study, the evaporation enthalpy presented a significant downward trend when the pore size was approximately 2 nm; moreover, they reported that the water content of the evaporator was controlled mainly by adding the upper and lower polyvinylidene fluoride (PVDF) membranes. Enhanced evaporation performance was obtained by optimizing nanopore structure with appropriate water volume. Therefore, the nanopore water effect is essential to reduce evaporation enthalpy. Li's team treated black PVA foam with nitric acid, granting it nanosize super hydrophilic pore structure (Figure 16g), and attained an evaporation enthalpy as low as 1081 J g⁻¹.^[218] In 2020, Singh et al. decorated a super-wicking, super-light-absorbing (SWSA) aluminum surface by femtosecond laser processing of aluminum.^[58] The SWSA surface was composed of layered micro-nano structure based on metal nanoparticles and microgrooves superimposed with nano-scale structure (Figure 16h), which not only generated

light traps to realize high absorption of sunlight due to uneven morphology, but also successfully reduced the enthalpy of evaporation to 1220 J g⁻¹. The reduction of energy requirement was because of the bonding of water molecules with aluminum on the surface of SWSA, which could turn DA-OH (3-molecule water clusters) into DDA-OH and DAA-OH (both 4-molecule water clusters) with more water molecule clusters. Faster evaporation was achieved due to the formation of large-sized clusters. Briefly, the reduction in enthalpy and vapor pressure in tiny nanostructure channels is on account of the change in the mode of water evaporation, i.e., the shift from the evaporation of a single water molecule to the evaporation of whole water clusters. Water confined in a narrow space evaporates more readily than water without any space restrictions; thus, the nano-sized pore structure might facilitate the formation of small-sized water clusters with low hydrogen bond density to reduce vaporization enthalpy.

Combined optimization of nanospace and hydrophilic functional groups can further regulate the formation of IW and water clusters, and alter the hydrogen bond of adjacent water molecules, thus lowering the energy required for vapor generation.^[219,220] For example, the PCP- α hybrid membranes

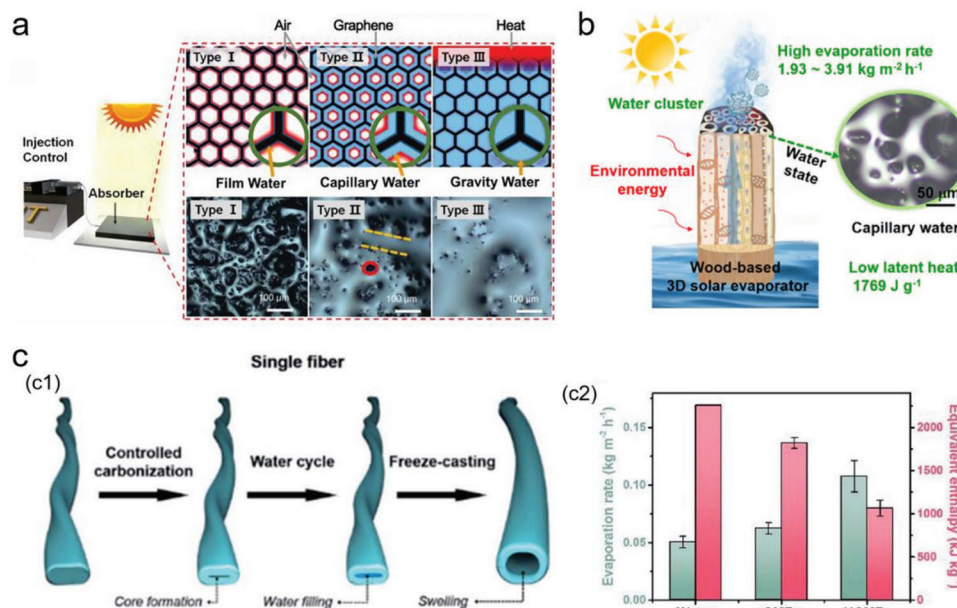


Figure 17. Schematic diagram and photos of a) water in different states including film water, capillary water, and gravitational water obtained by ICT. Reproduced with permission.^[54] Copyright 2019, Wiley-VCH. b) Capillary water in wood-based evaporator for generating steam. Reproduced with permission.^[222] Copyright 2020, American Chemical Society. c1) Schematic diagram of single fiber evolving into a hollow fiber with layered water path. c2) Comparison of equivalent enthalpy and dark evaporation rate of different samples. Reproduced with permission.^[221] Copyright 2021, Royal Society of Chemistry.

mentioned in Section 4.1.3 not only increase the IW content through the —OH of the pulp, but also divide the bulk water into clusters in the confined space.^[158] The activated IW and water clusters act synergistically to minimize the energy used for evaporation. Moreover, the HNG system of Yu et al.,^[21] which had the hydrophilic functional groups of PVA along with multi-scale nanostructures, exhibited an evaporation rate of $3.2 \text{ kg m}^{-2} \text{ h}^{-1}$. Thus, synergistic relationship between the two properties facilitates should be explored further to enhance water vapor production.

Porous structure gives rise to more clustered water. Unlike the evaporation of individual water molecules, clustered water presents lower hydrogen bond density per unit water molecule when evaporating because it only breaks the hydrogen bonds on the surface, thus requiring low latent heat of evaporation. Moreover, porosity leads to larger and more efficient evaporative surface area, promoting sufficient and rapid water evaporation. It doubly leads to a reduction in the enthalpy of evaporation. Further, molecular meshes for evaporation with abundant pore channels are created in this structure. The mesh can form and act as several dispersed local evaporation regions, which are beneficial for the formation of several photothermal reaction sites. The abovementioned three properties improve steam generation performance. Therefore, the micro-pore structure design can be considered new direction in the field of seawater desalination systems.

4.3. Capillary Water

Water replenishment is one of the most important parameters during the development of various SVG systems. At present, dif-

ferent materials exhibit sufficient or in some cases excess water supply. However, excess water supply causes heat loss, blocks the channels, and hinders the water evaporation process. Therefore, capillary water is an important breakthrough in the evaporation process (Figure 17a-c); it reduces the energy barrier to accelerate water vaporization and exposes a larger evaporation area and more steam escape space, which lowers the evaporation energy demand. Therefore, increased formation of capillary water should be targeted to lower the current enthalpy of vaporization during steam generation.

Recently, Qu et al. reported high evaporation performance by their SVG system, using appropriate water regulation methods such as ICT (as mentioned in Section 2.4).^[54] They directly and effectively adjusted the injection rate through ICT to control the water content injected into the rGO foam and to ensure that the water supply rate equals the evaporation rate (Figure 17a). They demonstrated that their system generated a large amount of capillary water in the rGO foam, which not only prevented the channel from being blocked, but also increased the evaporation area, thus realizing an evaporation rate of $2.4 \text{ kg m}^{-2} \text{ h}^{-1}$. Furthermore, the system exhibited low enthalpy of evaporation (below 1750 J g^{-1}). Moreover, they explored the injection rate and water content of different types of carbon-based materials using the ICT method, which was somewhat generalizable. In contrast, Lei et al.^[221] used carbonization and freeze-casting techniques to obtain a large number of hollow fibers with capillary structure (Figure 17c1), which enabled the generation of high amount of capillary water through the liquid surface film effect, thus promoted water evaporation and reduced energy utilization (Figure 17c2). Moreover, capillary water is commonly found in 3D evaporators. The desired amount of capillary water can be obtained by regulating the position of the sunlight-absorbing layer

above the liquid surface in the 3D structure. For example, a 3D balsa wood-based evaporator was prepared by Tang et al.^[222] In this evaporator, when the light-absorbing layer was located at the same height as the bulk water surface, the pore was completely filled with water, i.e., gravitational water was formed (Figure 17b). Conversely, capillary water was generated (without any restrictions) when the evaporating surface was adjusted above the surface of the bulk water. The water in the wood was kept in the capillary water state. Hence, pore channels were not blocked by water, exposing a larger evaporation space and water vapor escape channels. Similarly, Zhang et al. proposed a 3D evaporator synthesized using carbonized cattails,^[166] which utilized the unique strong capillary action of the cattails, and generated high capillary water content and lowered the latent heat of evaporation. Therefore, researchers have reported high evaporation performance by using appropriate water regulation methods, such as ICT, and regulating the height of the absorber layer above the liquid-gas interface in the 3D evaporator to obtain capillary water. Low dehydration temperature and weak bonding force of capillary water promote steam generation. Coupled with the fact that capillary water does not block the pore channels and exposes a larger evaporation area, the effect of reducing the enthalpy of evaporation is significantly achieved.

5. Conclusions and Perspectives

The advancements in the field of SVG technology offer valuable opportunities for access to clean water. This review provides a chronological overview of the milestone work in the field of solar interfacial evaporation systems since 2012, based on the following crucial parameters: heat management, mass control, water state adjustment, and multifunctional applications. Through this integrated approach, it is hoped to quickly understand the development of the field of interfacial water evaporation who are just stepping into SVG research. Although several materials and structures have been reported for improving the efficiency of SVG systems, further research is required for increasing their evaporation rates; this can be achieved by lowering the evaporation enthalpy of water. Reduced evaporation enthalpy can lead to a higher evaporation rate with the same energy input. To understand the underlying reasons behind the mechanism of the WEER system, we have discussed theoretical derivations, mechanisms, and characterization tests to demonstrate that water evaporation is linked to the interactions between water molecules. To achieve fast and efficient evaporation, it is necessary to reduce the energy barrier faced by water molecules, which is the evaporation enthalpy of water. This can be achieved when the concentration of water molecules with weak hydrogen bonds is increased or easy-to-evaporate water molecule skeletons are developed. Thus, we summarize several parameters for water activation: 1) Generation of IW in a hydratable network; IW forms weak hydrogen bonds with the surrounding water molecules and requires less energy to leave the surface of the liquid when evaporating. 2) Formation of large-sized water clusters should be targeted instead of a single water molecule; clustered water evaporation also only disconnects the hydrogen bonds on the surface to achieve overall evaporation. 3) Formation of capillary water; capillary water can expose a larger evaporation space for water evaporation and vapor spillage. Thus, all three strategies offer unlimited possibilities

for water activation. Our review also discusses these three mechanisms in detail with respect to material selection, hierarchical pores/nano-scale pores, and structural design (Figure 18). Many hydrophilic networks, including polymers, carbon materials, biomass, fibers, and emerging materials (MOFs, MXene) provide a variety of hydrophilic functional groups to harvest a higher amount of IW and to lower the latent heat of evaporation. We have also discussed designs such as bimodal pores, multi-scale pores, and nano-gaps that generate large amount of clustered water. The capillary water generated using various methods replaces gravitational water and achieves a faster evaporation effect.

It is worth emphasizing that these three mechanisms do not exhibit antagonistic relationships; IW and clustered water are usually present together in a system. The mechanisms behind both IW and clustered water generation are on a molecular scale, whereas that of capillary water is on a macroscopic scale. Therefore, these three mechanisms are classifications for different observational scales. Moreover, each mechanism exhibits both advantages and disadvantages. The IW mechanism is the most widely used for water activation and much subsequent research work has been conducted based on this mechanism. It focuses on the synthesis and preparation of materials. The formation of capillary water requires precise control of the water supply; therefore, a device based on this mechanism would be complex and expensive. However, capillary water can be obtained without extra modulation of hydrophilic groups; thus material synthesis using this mechanism is easy and increases the variety of potential material candidates. The current characterization of clustered water and its evaporation mechanism are poorly understood; capillary water can be observed using an optical microscope, and IW can be qualitatively and quantitatively characterized using advanced techniques as Raman spectroscopy and FTIR. Compared to traditional freshwater acquisition technologies, the advantage of interfacial water evaporation lies in completely passive evaporation, i.e., no additional energy supply and parts for transportation are required. Therefore, the IW mechanism is more competitive.

This review provides a systematic summary of water activation for future studies. Moreover, this review is expected to extend the application of photothermal interface evaporation to multidisciplinary fields, so as to develop a more efficient and reasonable method to use water resources. An interdisciplinary approach will help in establishing theoretical and practical significance of the evaporation process and laws, exploring the ecological cycle of nature, and protecting and utilizing nature. Although several breakthroughs have been made in solar-powered water evaporation systems, several challenges are yet to be overcome; a few are listed below.

- 1) Along with the in-depth study of water evaporation, the emergence of equivalent enthalpy of evaporation breaks the traditional concept that the water vaporization enthalpy is a fixed value (about 2.4 kJ g^{-1}) when the external temperature and pressure conditions are fixed. However, this concept requires further investigation, and the enthalpy can only be roughly estimated based on dark evaporation experiments and the integrated area of DSC curves. Even though plentiful studies have demonstrated the effect of IW and water clusters on lowering the enthalpy of evaporation, the exact mechanisms and

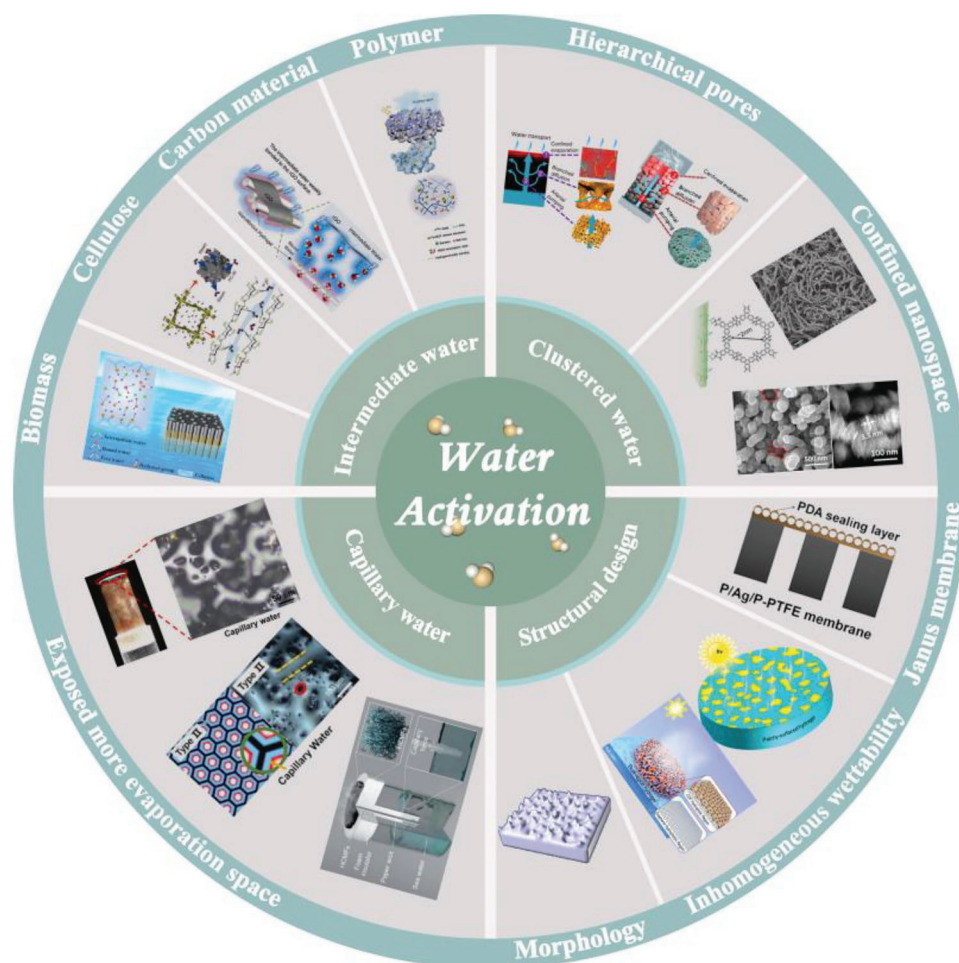


Figure 18. Summary of water activation mechanisms discussed in the review. Intermediate water. Reproduced with permission.^[134] Copyright 2020, Wiley-VCH. Reproduced with permission.^[99] Copyright 2021, Elsevier. Reproduced with permission.^[158] Copyright 2022, Springer Nature. Reproduced with permission.^[111] Copyright 2021, Royal Society of Chemistry. Clustered water. Reproduced with permission.^[21] Copyright 2018, Springer Nature. Reproduced with permission.^[211] Copyright 2019, Wiley-VCH. Reproduced with permission.^[113] Copyright 2021, Royal Society of Chemistry. Reproduced with permission.^[213] Copyright 2020, Wiley-VCH. Capillary water. Reproduced with permission.^[222] Copyright 2020, American Chemical Society. Reproduced with permission.^[54] Copyright 2019, Wiley-VCH. Reproduced with permission.^[221] Copyright 2021, Royal Society of Chemistry. Structural design. Reproduced with permission.^[179] Copyright 2019, American Chemical Society. Reproduced with permission.^[178] Copyright 2022, American Chemical Society. Reproduced with permission.^[52] Copyright 2020, Royal Society of Chemistry.

degree of energy reduction are unknown. Furthermore, the advantages and disadvantages of different hydrophilic functional groups with respect to reduction in enthalpy of an SVG system are unclear. There are still many deficiencies in exploring these issues, expecting more researchers to solve them together. In addition, the relationship between enthalpy and the freezing-melting process is complex and unclear, all of which are full of challenges.

- 2) Although DSC analysis, Raman spectroscopy, LiCl measurement using ICP-MS validate the concept of the enthalpy of evaporation and the presence of IW and water clusters in the WEER system, these concepts should be further analyzed. Moreover, the water content in each state (BW, IW, and FW) cannot be quantitatively measured in materials with different water content. Therefore, a consensus is required between theoretical analyses and various analytical methods. Moreover, IW and water clusters are hard to manufacture and char-

acterize independently, let alone to determine their sizes and distributions by means of spectra.

- 3) Misconceptions regarding evaporation enthalpy and the measurement of evaporation performance should be clarified. For example, it has not been proven that the energy input between water and the sample is equivalent in the estimation of evaporation enthalpy using Equation 25 (Section 3.5.1). The calculation method of equivalent evaporation enthalpy is not accurate and needs further improvement. Additionally, the most critical indicator of evaporation performance should be determined because it is possible that evaporation rate is a significant criterion for evaluating seawater desalination performance but not for high efficiency of an evaporator. Currently, the criteria to calculate evaporation rate have not been established. Moreover, the scientific community has different views regarding projected area/actual evaporation area and whether dark evaporation rate should be subtracted.

The evaporation efficiency is affected by many complex factors, with the main being optical and thermal losses. Moreover, it is of no practical significance to use the equivalent enthalpy of evaporation to calculate the efficiency. A few advanced 3D evaporators harness additional energy from the external environment; however, the extra energy cannot be considered while calculating the equivalent enthalpy of evaporation. Therefore, the current method to calculate the equivalent evaporation enthalpy as the standard of evaporation efficiency of a system will not be rigorous. Hence, smaller enthalpy of evaporation does not indicate higher efficiency. The evaporation capability of a system cannot be decided using only the enthalpy of evaporation, and other factors, such as saturated water content and temperature response time, should be taken into account to obtain the best evaporation effect.

- 4) Currently, only a few studies have reported increased vapor generation rate using capillary water. Although we have summarized the regulation strategies for different states of water with a focus on three mechanisms to activate water evaporation, the association between the capillary water mechanism and the other two mechanisms is inconclusive. The state of hydrogen bonds in capillary water is unelucidated, which requires the joint efforts of researchers from all walks of life.
- 5) Despite the high efficiency of solar interfacial evaporation systems, their water yield is not satisfactory in practical desalination applications. The water yield of SVG systems is not equal to the evaporation rate. Therefore, the importance of water extraction rate should be considered because it indicates the final yield of water. Moreover, the cold steam obtained by absorbing environmental energy is generated in an open system, but the collection of the condensate requires a closed space.^[223–225] Practical application of SVG systems for access to clean water is yet to be achieved. Therefore, future research should focus on steam generation, condensation cycle, and clean water harvesting, in addition to the evaporation process. A series of feasible methods, such as decoupling the light absorption system from the evaporation system, integrating multi-cooperation system of passive radiative condensation and fog collection technology, and changing the water transportation path, should be continuously researched and improved to increase freshwater output.

Acknowledgements

The authors gratefully acknowledge the financial support of the National Natural Science Foundation of China (No. 52075309), the Youth Innovation Team of Shaanxi Universities (21JY021), the JST-ERATO Yamauchi Materials Space-Tectonics Project (JPMJER2003), and the Science and Technology Department, Shaanxi Province (2021GY-248). This work used the Queensland node of the NCRIS-enabled Australian National Fabrication Facility (ANFF).

Open access publishing facilitated by The University of Queensland, as part of the Wiley - The University of Queensland agreement via the Council of Australian University Librarians.

Conflict of Interest

The authors declare no conflict of interest.

Keywords

evaporation enthalpy, solar-powered vaporization, water activation

Received: December 25, 2022

Revised: May 31, 2023

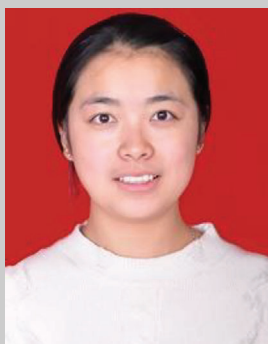
Published online: October 15, 2023

- [1] M. M. Mekonnen, A. Y. Hoekstra, *Sci. Adv.* **2016**, 2, e1500323.
- [2] C. J. Vörösmarty, P. Green, J. Salisbury, R. B. Lammers, *Science* **2000**, 289, 284.
- [3] N. S. Lewis, *Science* **2016**, 351, aad1920.
- [4] M. A. Shannon, P. W. Bohn, M. Elimelech, J. G. Georgiadis, B. J. Mariñas, A. M. Mayes, *Nature* **2008**, 452, 301.
- [5] H. Hertz, *Ann. Phys.* **1882**, 253, 177.
- [6] M. Knudsen, *Ann. Phys.* **1915**, 352, 697.
- [7] O. Knacke, I. N. Stranski, *Prog. Met. Phys.* **1956**, 6, 181.
- [8] G. Chen, *Int. J. Heat Mass Transfer* **2022**, 191, 122845.
- [9] X. Li, R. Lin, G. Ni, N. Xu, X. Hu, B. Zhu, G. Lv, J. Li, S. Zhu, J. Zhu, *Natl. Sci. Rev.* **2018**, 5, 70.
- [10] X. Wu, G. Y. Chen, W. Zhang, X. Liu, H. Xu, *Adv. Sustainable Syst.* **2017**, 1, 1700046.
- [11] C. Li, D. Jiang, B. Huo, M. Ding, C. Huang, D. Jia, H. Li, C.-Y. Liu, J. Liu, *Nano Energy* **2019**, 60, 841.
- [12] F. Yang, J. Chen, Z. Ye, D. Ding, N. V. Myung, Y. Yin, *Adv. Funct. Mater.* **2021**, 31, 2006294.
- [13] N. Xu, X. Hu, W. Xu, X. Li, L. Zhou, S. Zhu, J. Zhu, *Adv. Mater.* **2017**, 29, 1606762.
- [14] Y. Xu, D. Liu, H. Xiang, S. Ren, Z. Zhu, D. Liu, H. Xu, F. Cui, W. Wang, *J. Membr. Sci.* **2019**, 586, 222.
- [15] S. Wu, G. Xiong, H. Yang, B. Gong, Y. Tian, C. Xu, Y. Wang, T. Fisher, J. Yan, K. Cen, T. Luo, X. Tu, Z. Bo, K. Ostrikov, *Adv. Energy Mater.* **2019**, 9, 1901286.
- [16] V. Kashyap, A. Al-Bayati, S. M. Sajadi, P. Irajizad, S. H. Wang, H. Ghasemi, *J. Mater. Chem. A* **2017**, 5, 15227.
- [17] S. Gao, X. Dong, J. Huang, J. Dong, F. D. Maggio, S. Wang, F. Guo, T. Zhu, Z. Chen, Y. Lai, *Global Challenge* **2019**, 3, 1800117.
- [18] L. Wu, Z. Dong, Z. Cai, T. Ganapathy, N. X. Fang, C. Li, C. Yu, Y. Zhang, Y. Song, *Nat. Commun.* **2020**, 11, 521.
- [19] M. Zhu, Y. Li, G. Chen, F. Jiang, Z. Yang, X. Luo, Y. Wang, S. D. Lacey, J. Dai, C. Wang, C. Jia, J. Wan, Y. Yao, A. Gong, B. Yang, Z. Yu, S. Das, L. Hu, *Adv. Mater.* **2017**, 29, 1704107.
- [20] T. Li, Q. Fang, X. Xi, Y. Chen, F. Liu, *J. Mater. Chem. A* **2019**, 7, 586.
- [21] F. Zhao, X. Zhou, Y. Shi, X. Qian, M. Alexander, X. Zhao, S. Mendez, R. Yang, L. Qu, G. Yu, *Nat. Nanotechnol.* **2018**, 13, 489.
- [22] J. J. Koh, G. J. H. Lim, S. Chakraborty, Y. Zhang, S. Liu, X. Zhang, S. C. Tan, Z. Lyu, J. Ding, C. He, *Nano Energy* **2021**, 79, 105436.
- [23] O. Neumann, A. S. Urban, J. Day, S. Lal, P. Nordlander, N. J. Halas, *ACS Nano* **2013**, 7, 42.
- [24] Z. Wang, Y. Liu, P. Tao, Q. Shen, N. Yi, F. Zhang, Q. Liu, C. Song, D. Zhang, W. Shang, T. Deng, *Small* **2014**, 10, 3234.
- [25] H. Ghasemi, G. Ni, A. M. Marconnet, J. Loomis, S. Yerci, N. Miljkovic, G. Chen, *Nat. Commun.* **2014**, 5, 4449.
- [26] L. Zhang, B. Tang, J. Wu, R. Li, P. Wang, *Adv. Mater.* **2015**, 27, 4889.
- [27] Y. Liu, S. Yu, R. Feng, A. Bernard, Y. Liu, Y. Zhang, H. Duan, W. Shang, P. Tao, C. Song, T. Deng, *Adv. Mater.* **2015**, 27, 2768.
- [28] F. Domínguez-Muñoz, B. Anderson, J. M. Cejudo-López, A. Carrillo-Andrés, *Energy Build.* **2010**, 42, 2159.
- [29] H. Masuda, K. Fukuda, *Science* **1995**, 268, 1466.
- [30] J. Q. Xi, M. F. Schubert, J. K. Kim, E. F. Schubert, M. Chen, S.-Y. Lin, W. Liu, J. A. Smart, *Nat. Photonics* **2007**, 1, 176.

- [31] K. Bae, G. Kang, S. K. Cho, W. Park, K. Kim, W. J. Padilla, *Nat. Commun.* **2015**, 6, 10103.
- [32] L. Zhou, Y. Tan, D. Ji, B. Zhu, P. Zhang, J. Xu, Q. Gan, Z. Yu, J. Zhu, *Sci. Adv.* **2016**, 2, e1501227.
- [33] L. Zhou, Y. Tan, J. Wang, W. Xu, Y. Yuan, W. Cai, S. Zhu, J. Zhu, *Nat. Photonics* **2016**, 10, 393.
- [34] M. Zhu, Y. Li, F. Chen, X. Zhu, J. Dai, Y. Li, Z. Yang, X. Yan, J. Song, Y. Wang, E. Hitz, W. Luo, M. Lu, B. Yang, L. Hu, *Adv. Energy Mater.* **2018**, 8, 1701028.
- [35] Y. Shi, R. Li, Y. Jin, S. Zhuo, L. Shi, J. Chang, S. Hong, K.-C. Ng, P. Wang, *Joule* **2018**, 2, 1171.
- [36] G. Ni, G. Li, S. V. Boriskina, H. Li, W. Yang, T. Zhang, G. Chen, *Nat. Energy* **2016**, 1, 16126.
- [37] A. K. Menon, I. Haechler, S. Kaur, S. Lubner, R. S. Prasher, *Nat. Sustainability* **2020**, 3, 144.
- [38] Y. Hu, H. Ma, M. Wu, T. Lin, H. Yao, F. Liu, H. Cheng, L. Qu, *Nat. Commun.* **2022**, 13, 4335.
- [39] T. Gao, Y. Wang, X. Wu, P. Wu, X. Yang, Q. Li, Z. Zhang, D. Zhang, G. Owens, H. Xu, *Sci. Bull.* **2022**, 67, 1572.
- [40] X. Li, W. Xu, M. Tang, L. Zhou, B. Zhu, S. Zhu, J. Zhu, *Proc. Natl. Acad. Sci. USA* **2016**, 113, 13953.
- [41] Y. Liu, J. Chen, D. Guo, M. Cao, L. Jiang, *ACS Appl. Mater. Interfaces* **2015**, 7, 13645.
- [42] W. Xu, X. Hu, S. Zhuang, Y. Wang, X. Li, L. Zhou, S. Zhu, J. Zhu, *Adv. Energy Mater.* **2018**, 8, 1702884.
- [43] G. Ni, S. H. Zandavi, S. M. Javid, S. V. Boriskina, T. A. Cooper, G. Chen, *Energy Environ. Sci.* **2018**, 11, 1510.
- [44] Y. Shi, C. Zhang, R. Li, S. Zhuo, Y. Jin, L. Shi, S. Hong, J. Chang, C. Ong, P. Wang, *Environ. Sci. Technol.* **2018**, 52, 11822.
- [45] Y. Xia, Q. Hou, H. Jubaer, Y. Li, Y. Kang, S. Yuan, H. Liu, M. W. Woo, L. Zhang, L. Gao, H. Wang, X. Zhang, *Energy Environ. Sci.* **2019**, 12, 1840.
- [46] X. Wu, Y. Wang, P. Wu, J. Zhao, Y. Lu, X. Yang, H. Xu, *Adv. Funct. Mater.* **2021**, 31, 2102618.
- [47] S. He, C. Chen, Y. Kuang, R. Mi, Y. Liu, Y. Pei, W. Kong, W. Gan, H. Xie, E. Hitz, C. Jia, X. Chen, A. Gong, J. Liao, J. Li, Z. J. Ren, B. Yang, S. Das, L. Hu, *Energy Environ. Sci.* **2019**, 12, 1558.
- [48] Z. Liu, B. Wu, B. Zhu, Z. Chen, M. Zhu, X. Liu, *Adv. Funct. Mater.* **2019**, 29, 1905485.
- [49] M. Morciano, M. Fasano, S. V. Boriskina, E. Chiavazzo, P. Asinari, *Energy Environ. Sci.* **2020**, 13, 3646.
- [50] Z. Wang, J. Gao, J. Zhou, J. Gong, L. Shang, H. Ye, F. He, S. Peng, Z. Lin, Y. Li, F. Caruso, *Adv. Mater.* **2022**, 35, 2209015.
- [51] X. Zhou, F. Zhao, Y. Guo, Y. Zhang, G. Yu, *Energy Environ. Sci.* **2018**, 11, 1985.
- [52] Y. Guo, X. Zhao, F. Zhao, Z. Jiao, X. Zhou, G. Yu, *Energy Environ. Sci.* **2020**, 13, 2087.
- [53] C. Lei, W. Guan, Y. Guo, W. Shi, Y. Wang, K. P. Johnston, G. Yu, *Angew. Chem., Int. Ed.* **2022**, 61, e202208487.
- [54] H. Liang, Q. Liao, N. Chen, Y. Liang, G. Lv, P. Zhang, B. Lu, L. Qu, *Angew. Chem., Int. Ed.* **2019**, 58, 19041.
- [55] Y. Tu, J. Zhou, S. Lin, M. AlShrah, X. Zhao, G. Chen, *ArXiv* **2022**.
- [56] Y. Tu, G. Chen, *ArXiv* **2022**.
- [57] J. Xiao, Y. Guo, W. Luo, D. Wang, S. Zhong, Y. Yue, C. Han, R. Lv, J. Feng, J. Wang, W. Huang, X. Tian, W. Xiao, Y. Shen, *Nano Energy* **2021**, 87, 106213.
- [58] S. C. Singh, M. ElKabbash, Z. Li, X. Li, B. Regmi, M. Madsen, S. A. Jalil, Z. Zhan, J. Zhang, C. Guo, *Nat. Sustainability* **2020**, 3, 938.
- [59] H.-Y. Zhao, J. Zhou, Z.-L. Yu, L.-F. Chen, H.-J. Zhan, H.-W. Zhu, J. Huang, L.-A. Shi, S.-H. Yu, *Cell Rep. Phys. Sci.* **2020**, 1, 100074.
- [60] Y. Tian, X. Liu, J. Li, Y. Deng, J. A. DeGiorgis, S. Zhou, A. Caratenuto, M. L. Minus, Y. Wan, G. Xiao, Y. Zheng, *Cell Rep. Phys. Sci.* **2021**, 2, 100549.
- [61] Y. Shi, O. Ilic, H. A. Atwater, J. R. Greer, *Nat. Commun.* **2021**, 12, 2797.
- [62] H. Yao, P. Zhang, C. Yang, Q. Liao, X. Hao, Y. Huang, M. Zhang, X. Wang, T. Lin, H. Cheng, J. Yuan, L. Qu, *Energy Environ. Sci.* **2021**, 14, 5330.
- [63] X. Li, G. Ni, T. Cooper, N. Xu, J. Li, L. Zhou, X. Hu, B. Zhu, P. Yao, J. Zhu, *Joule* **2019**, 3, 1798.
- [64] E. Chiavazzo, M. Morciano, F. Viglino, M. Fasano, P. Asinari, *Nat. Sustainability* **2018**, 1, 763.
- [65] Z. Xu, L. Zhang, L. Zhao, B. Li, B. Bhatia, C. Wang, K. L. Wilke, Y. Song, O. Labban, J. H. Lienhard, R. Wang, E. N. Wang, *Energy Environ. Sci.* **2020**, 13, 830.
- [66] P. Yang, K. Liu, Q. Chen, J. Li, J. Duan, G. Xue, Z. Xu, W. Xie, J. Zhou, *Energy Environ. Sci.* **2017**, 10, 1923.
- [67] W. Wang, Y. Shi, C. Zhang, S. Hong, L. Shi, J. Chang, R. Li, Y. Jin, C. Ong, S. Zhuo, P. Wang, *Nat. Commun.* **2019**, 10, 3012.
- [68] T. Li, M. Wu, S. Wu, S. Xiang, J. Xu, J. Chao, T. Yan, T. Deng, R. Wang, *Nano Energy* **2021**, 89, 106338.
- [69] H.-Y. Zhao, C. Shu, P. Min, C. Li, W. Deng, J. Yang, X. Li, Z.-Z. Yu, *J. Mater. Chem. A* **2022**, 10, 22488.
- [70] L. Cui, P. Zhang, Y. Xiao, Y. Liang, H. Liang, Z. Cheng, L. Qu, *Adv. Mater.* **2018**, 30, 1706805.
- [71] X. Zhao, L.-M. Peng, C.-Y. Tang, J.-H. Pu, X.-J. Zha, K. Ke, R.-Y. Bao, M.-B. Yang, W. Yang, *Mater. Horiz.* **2020**, 7, 855.
- [72] Y. Zhang, S. K. Ravi, L. Yang, J. V. Vaghiasia, L. Suresh, I. Tan, S. C. Tan, *ACS Appl. Mater. Interfaces* **2019**, 11, 38674.
- [73] H. Song, Y. Liu, Z. Liu, M. H. Singer, C. Li, A. R. Cheney, D. Ji, L. Zhou, N. Zhang, X. Zeng, Z. Bei, Z. Yu, S. Jiang, Q. Gan, *Adv. Sci.* **2018**, 5, 1800222.
- [74] X. Li, J. Li, J. Lu, N. Xu, C. Chen, X. Min, B. Zhu, H. Li, L. Zhou, S. Zhu, T. Zhang, J. Zhu, *Joule* **2018**, 2, 1331.
- [75] Y. Wang, X. Wu, P. Wu, J. Zhao, X. Yang, G. Owens, H. Xu, *Sci. Bull.* **2021**, 66, 2479.
- [76] P. Wu, X. Wu, Y. Wang, H. Xu, G. Owens, *Water Res.* **2022**, 212, 118099.
- [77] J. Li, M. Du, G. Lv, L. Zhou, X. Li, L. Bertoluzzi, C. Liu, S. Zhu, J. Zhu, *Adv. Mater.* **2018**, 30, 1805159.
- [78] Y. Guo, C. M. Dundas, X. Zhou, K. P. Johnston, G. Yu, *Adv. Mater.* **2021**, 33, 2102994.
- [79] P. Zhang, F. Zhao, W. Shi, H. Lu, X. Zhou, Y. Guo, G. Yu, *Adv. Mater.* **2022**, 34, 2110548.
- [80] W. B. Wang, Y. Shi, C. L. Zhang, R. Y. Li, M. C. Wu, S. F. Zhuo, S. Aleid, P. Wang, *Energy Environ. Sci.* **2022**, 15, 136.
- [81] F. Wang, N. Xu, W. Zhao, L. Zhou, P. Zhu, X. Wang, B. Zhu, J. Zhu, *Joule* **2021**, 5, 1602.
- [82] M. Zhou, H. Song, X. Xu, A. Shahsafi, Y. Qu, Z. Xia, Z. Ma, M. A. Kats, J. Zhu, B. S. Ooi, Q. Gan, Z. Yu, *Proc. Natl. Acad. Sci. USA* **2021**, 118, e2019292118.
- [83] S. Zeng, S. Pian, M. Su, Z. Wang, M. Wu, X. Liu, M. Chen, Y. Xiang, J. Wu, M. Zhang, Q. Cen, Y. Tang, X. Zhou, Z. Huang, R. Wang, A. Tunuhe, X. Sun, Z. Xia, M. Tian, M. Chen, X. Ma, L. Yang, J. Zhou, H. Zhou, Q. Yang, X. Li, Y. Ma, G. Tao, *Science* **2021**, 373, 692.
- [84] J. Mandal, Y. Fu, A. C. Overvig, M. Jia, K. Sun, N. N. Shi, H. Zhou, X. Xiao, N. Yu, Y. Yang, *Science* **2018**, 362, 315.
- [85] M. Cao, J. Xiao, C. Yu, K. Li, L. Jiang, *Small* **2015**, 11, 4379.
- [86] Z. Yu, F. F. Yun, Y. Wang, L. Yao, S. Dou, K. Liu, L. Jiang, *X. Small* **2017**, 13, 1701403.
- [87] M. S. Jhon, J. D. Andrade, *J. Biomed. Mater. Res.* **1973**, 7, 509.
- [88] I. Ohmine, H. Tanaka, *Chem. Rev.* **1993**, 93, 2545.
- [89] Z. Zhang, X. Li, J. Yin, Y. Xu, W. Fei, M. Xue, Q. Wang, J. Zhou, W. Guo, *Nat. Nanotechnol.* **2018**, 13, 1109.
- [90] F. Zhao, Y. Guo, X. Zhou, W. Shi, G. Yu, *Nat. Rev. Mater.* **2020**, 5, 388.
- [91] X. Zhou, F. Zhao, Y. Guo, B. Rosenberger, G. Yu, *Sci. Adv.* **2019**, 5, eaaw5484.

- [92] C. Jia, Y. Li, Z. Yang, G. Chen, Y. Yao, F. Jiang, Y. Kuang, G. Pastel, H. Xie, B. Yang, S. Das, L. Hu, *Joule* **2017**, 1, 588.
- [93] V. Kashyap, H. Ghasemi, *J. Mater. Chem. A* **2020**, 8, 7035.
- [94] J. Wang, T. Hou, *J. Chem. Theory Comput.* **2011**, 7, 2151.
- [95] A. Luzar, D. Chandler, *Nature* **1996**, 379, 55.
- [96] Y. Sekine, T. Ikeda-Fukazawa, *J. Chem. Phys.* **2009**, 130, 034501.
- [97] X. Zhou, Y. Guo, F. Zhao, G. Yu, *Acc. Chem. Res.* **2019**, 52, 3244.
- [98] K. Kudo, J. Ishida, G. Syuu, Y. Sekine, T. Ikeda-Fukazawa, *J. Chem. Phys.* **2014**, 140, 044909.
- [99] L. Zang, L. Sun, S. Zhang, C. Finnerty, A. Kim, J. Ma, B. Mi, *Chem. Eng. J.* **2021**, 422, 129998.
- [100] A. Fujii, K. Mizuse, *Int. Rev. Phys. Chem.* **2013**, 32, 266.
- [101] M. Miyazaki, A. Fujii, T. Ebata, N. Mikami, *Science* **2004**, 304, 1134.
- [102] J. Li, R. Long, B. Zhang, R. Yang, W. Liu, Z. Liu, *J. Phys. Chem. Lett.* **2020**, 11, 9856.
- [103] Y. Kong, H. Dan, W. Kong, Y. Gao, Y. Shang, K. Ji, Q. Yue, B. Gao, *J. Mater. Chem. A* **2020**, 8, 24734.
- [104] Z. Sun, J. Wang, Q. Wu, Z. Wang, Z. Wang, J. Sun, C.-J. Liu, *Adv. Funct. Mater.* **2019**, 29, 1901312.
- [105] X. Luo, J. Shi, C. Zhao, Z. Luo, X. Gu, H. Bao, *Appl. Energy* **2021**, 302, 117581.
- [106] Z. Dong, C. Zhang, H. Peng, J. Gong, Q. Zhao, *J. Mater. Chem. A* **2020**, 8, 24493.
- [107] Y. Bian, Y. Shen, K. Tang, Q. Du, L. Hao, D. Liu, J. Hao, D. Zhou, X. Wang, H. Zhang, P. Li, Y. Sang, X. Yuan, L. Zhao, J. Ye, B. Liu, H. Lu, Y. Yang, R. Zhang, Y. Zheng, X. Xiong, S. Gu, *Global Challenge* **2019**, 3, 1900040.
- [108] Q.-F. Guan, Z.-M. Han, Z.-C. Ling, H.-B. Yang, S.-H. Yu, *Nano Lett.* **2020**, 20, 5699.
- [109] Z. H. Ping, Q. T. Nguyen, S. M. Chen, J. Q. Zhou, Y. D. Ding, *Polymer* **2001**, 42, 8461.
- [110] M. S. Zafar, M. Zahid, A. Athanassiou, D. Fragouli, *Adv. Sustainable Syst.* **2021**, 5, 2100031.
- [111] Y. Chen, J. Yang, L. Zhu, X. Jia, S. Wang, Y. Li, H. Song, *J. Mater. Chem. A* **2021**, 9, 15482.
- [112] J.-Y. Wang, X.-X. Guo, J. Chen, S.-C. Hou, H.-J. Li, A. Haleem, S.-Q. Chen, W.-D. He, *Mater. Adv.* **2021**, 2, 3088.
- [113] S. Zhou, Z. Qiu, M. Stromme, C. Xu, *Energy Environ. Sci.* **2021**, 14, 900.
- [114] P. Król, *Prog. Mater. Sci.* **2007**, 52, 915.
- [115] G. Tedeschi, S. Guzman-Puyol, U. C. Paul, M. J. Barthel, L. Goldoni, G. Caputo, L. Ceseracciu, A. Athanassiou, J. A. Heredia-Guerrero, *Chem. Eng. J.* **2018**, 348, 840.
- [116] S.-L. Loo, L. Vásquez, U. C. Paul, L. Campagnolo, A. Athanassiou, D. Fragouli, *ACS Appl. Mater. Interfaces* **2020**, 12, 10307.
- [117] D. E. Babelo, Y. Ishikawa, *Chem. Phys. Lett.* **2000**, 319, 679.
- [118] X. Li, Z.-Z. Yang, *J. Phys. Chem. A* **2005**, 109, 4102.
- [119] M. T. Rodgers, P. B. Armentrout, *J. Phys. Chem. A* **1997**, 101, 1238.
- [120] G. Chen, *Phys. Chem. Chem. Phys.* **2022**, 24, 12329.
- [121] H.-Y. Zhao, J. Huang, J. Zhou, L.-F. Chen, C. Wang, Y. Bai, J. Zhou, Y. Deng, W.-X. Dong, Y.-S. Li, S.-H. Yu, *ACS Nano* **2022**, 16, 3554.
- [122] S. Meng, X.-J. Zha, C. Wu, X. Zhao, M.-B. Yang, W. Yang, *Nano Lett.* **2021**, 21, 10516.
- [123] Y. Liang, Y. Bai, A.-Q. Xie, J. Mao, L. Zhu, S. Chen, *Sol. RRL* **2022**, 6, 2100917.
- [124] C. Ma, Q. Liu, Q. Peng, G. Yang, M. Jiang, L. Zong, J. Zhang, *ACS Nano* **2021**, 15, 19877.
- [125] L. Hao, N. Liu, H. Bai, P. He, R. Niu, J. Gong, *J. Colloid Interface Sci.* **2022**, 608, 840.
- [126] C. Li, B. Zhu, Z. Liu, J. Zhao, R. Meng, L. Zhang, Z. Chen, *Chem. Eng. J.* **2022**, 431, 134224.
- [127] J. Su, Q. Chang, C. Xue, J. Yang, S. Hu, *Carbon* **2022**, 194, 267.
- [128] Z. Xu, N. Rao, C.-Y. Tang, W.-C. Law, *Micromachines* **2020**, 11, 867.
- [129] H. Zhang, X. Shen, E. Kim, M. Wang, J.-H. Lee, H. Chen, G. Zhang, J.-K. Kim, *Adv. Funct. Mater.* **2022**, 32, 2111794.
- [130] Z. Yu, P. Wu, *Adv. Mater. Technol.* **2020**, 5, 2000065.
- [131] Y. Guo, X. Zhou, F. Zhao, J. Bae, B. Rosenberger, G. Yu, *ACS Nano* **2019**, 13, 7913.
- [132] B. Wen, X. Zhang, Y. Yan, Y. Huang, S. Lin, Y. Zhu, Z. Wang, B. Zhou, S. Yang, J. Liu, *Desalination* **2021**, 516, 115228.
- [133] Y. Lu, D. Fan, Y. Wang, H. Xu, C. Lu, X. Yang, *ACS Nano* **2021**, 15, 10366.
- [134] Y. Guo, H. Lu, F. Zhao, X. Zhou, W. Shi, G. Yu, *Adv. Mater.* **2020**, 32, 1907061.
- [135] W. Wang, J. Niu, J. Guo, L. Yin, H. Huang, *Sol. Energy Mater. Sol. Cells* **2019**, 201, 110046.
- [136] M. S. Irshad, X. Wang, M. S. Abbasi, N. Arshad, Z. Chen, Z. Guo, L. Yu, J. Qian, J. You, T. Mei, *ACS Sustainable Chem. Eng.* **2021**, 9, 3887.
- [137] X. Liu, Y. Tian, Y. Wu, A. Caratenuto, F. Chen, S. Cui, J. A. DeGiorgis, Y. Wan, Y. Zheng, *J. Mater. Chem. A* **2021**, 9, 22313.
- [138] Y. Liu, H. Liu, J. Xiong, A. Li, R. Wang, L. Wang, X. Qin, J. Yu, *Chem. Eng. J.* **2022**, 427, 131539.
- [139] J. He, Y. Fan, C. Xiao, F. Liu, H. Sun, Z. Zhu, W. Liang, A. Li, *Compos. Sci. Technol.* **2021**, 204, 108633.
- [140] S. Cao, J. Jiang, Q. Tian, C. Guo, X. Wang, K. Dai, Q. Xu, *Green Energy Environ.* **2022**, 7, 1006.
- [141] S. Chen, Z. Sun, W. Xiang, C. Shen, Z. Wang, X. Jia, J. Sun, C.-J. Liu, *Nano Energy* **2020**, 76, 104998.
- [142] H. Wang, R. Zhang, D. Yuan, S. Xu, L. Wang, *Adv. Funct. Mater.* **2020**, 30, 2003995.
- [143] X. Zhou, Y. Guo, F. Zhao, W. Shi, G. Yu, *Adv. Mater.* **2020**, 32, 2007012.
- [144] Y. Chen, J. Yang, G. Jinsong, F. Fang, R. Bao, L. Xu, **2022**, <https://doi.org/10.21203/rs.3.rs-1489297/v1>.
- [145] F. Zhu, L. Wang, B. Demir, M. An, Z. L. Wu, J. Yin, R. Xiao, Q. Zheng, J. Qian, *Mater. Horiz.* **2020**, 7, 3187.
- [146] W. He, L. Zhou, M. Wang, Y. Cao, X. Chen, X. Hou, *Sci. Bull.* **2021**, 66, 1472.
- [147] W. Guan, Y. Guo, G. Yu, *Small* **2021**, 17, 2007176.
- [148] X. Li, B. Zhu, J. Zhu, *Carbon* **2019**, 146, 320.
- [149] P. Zhuang, D. Li, N. Xu, X. Yu, L. Zhou, *Global Challenge* **2021**, 5, 2000053.
- [150] W. Li, X. Li, W. Chang, J. Wu, P. Liu, J. Wang, X. Yao, Z.-Z. Yu, *Nano Res.* **2020**, 13, 3048.
- [151] J. Han, Z. Dong, L. Hao, J. Gong, Q. Zhao, *Green Energy Environ.* **2023**, 8, 151.
- [152] L. Cao, M. J. Meziani, S. Sahu, Y.-P. Sun, *Acc. Chem. Res.* **2013**, 46, 171.
- [153] L. Bao, C. Liu, Z.-L. Zhang, D.-W. Pang, *Adv. Mater.* **2015**, 27, 1663.
- [154] S. Hu, A. Trinch, P. Atkin, I. Cole, *Angew. Chem., Int. Ed.* **2015**, 54, 2970.
- [155] Q. Hou, C. Xue, N. Li, H. Wang, Q. Chang, H. Liu, J. Yang, S. Hu, *Carbon* **2019**, 149, 556.
- [156] H. Zhou, C. Xue, Q. Chang, J. Yang, S. Hu, *Chem. Eng. J.* **2021**, 421, 129822.
- [157] K. Nabeela, M. N. Thorat, S. N. Backer, A. M. Ramachandran, R. T. Thomas, G. Preethikumar, A. P. Mohamed, A. Asok, S. G. Dastager, S. Pillai, *ACS Appl. Bio Mater.* **2021**, 4, 4373.
- [158] L. Hao, N. Liu, R. Niu, J. Gong, T. Tang, *Sci. China Mater.* **2022**, 65, 201.
- [159] L. Song, X.-F. Zhang, Z. Wang, T. Zheng, J. Yao, *Desalination* **2021**, 507, 115024.
- [160] P. He, L. Hao, N. Liu, H. Bai, R. Niu, J. Gong, *Chem. Eng. J.* **2021**, 423, 130268.
- [161] X. Zhang, L. Yang, B. Dang, J. Tao, S. Li, S. Zhao, W. Li, J. Li, Z. Chen, S. Liu, *Nano Energy* **2020**, 78, 105322.

- [162] N. Liu, L. Hao, B. Zhang, R. Niu, J. Gong, T. Tang, *Energy Environ. Mater.* **2022**, 5, 617.
- [163] Z. Hu, L. Hao, N. Liu, P. He, H. Bai, R. Niu, J. Gong, *Mater. Today Commun.* **2021**, 28, 102636.
- [164] Z. Sun, W. Li, W. Song, L. Zhang, Z. Wang, *J. Mater. Chem. A* **2020**, 8, 349.
- [165] X. Shan, M. Xiong, Y. Sheng, A. Zhao, Y. Di, C. Liu, Z. Gan, *Adv. Energy Sustainability Res.* **2020**, 1, 2000034.
- [166] C. Zhang, B. Yuan, Y. Liang, L. Yang, L. Bai, H. Yang, D. Wei, W. Wang, H. Chen, *Sol. Energy Mater. Sol. Cells* **2021**, 227, 111127.
- [167] Y. Xu, X. Xiao, X. Fan, Y. Yang, C. Song, Y. Fan, Y. Liu, *J. Mater. Chem. A* **2020**, 8, 24108.
- [168] J. Lee, K. Kim, S. H. Park, G. Y. Yoon, J. Kim, S. J. Lee, *Nano Energy* **2020**, 77, 105130.
- [169] W. Zhang, Q. Chang, C. Xue, J. Yang, S. Hu, *Sol. RRL* **2021**, 5, 2100133.
- [170] T. T. Pham, T. H. Nguyen, T. A. H. Nguyen, D. D. Pham, D. C. Nguyen, D. B. Do, H. V. Nguyen, M. H. Ha, Z. H. Nguyen, *Desalination* **2021**, 518, 115280.
- [171] Z. Dong, C. Zhang, H. Peng, J. Gong, H. Wang, Q. Zhao, J. Yuan, *Mater. Horiz.* **2020**, 7, 2683.
- [172] F. He, X. Wu, J. Gao, Z. Wang, *J. Mater. Chem. A* **2021**, 9, 27121.
- [173] Y. Lu, D. Fan, Z. Shen, H. Zhang, H. Xu, X. Yang, *Nano Energy* **2022**, 95, 107016.
- [174] Z. Liu, Z. Zhou, N. Wu, R. Zhang, B. Zhu, H. Jin, Y. Zhang, M. Zhu, Z. Chen, *ACS Nano* **2021**, 15, 13007.
- [175] X.-P. Li, X. Li, H. Li, Y. Zhao, J. Wu, S. Yan, Z.-Z. Yu, *Adv. Funct. Mater.* **2022**, 32, 2110636.
- [176] R. Wan, C. Wang, X. Lei, G. Zhou, H. Fang, *Phys. Rev. Lett.* **2015**, 115, 195901.
- [177] Y. Zhang, F. Shen, W. Cao, Y. Wan, *Desalination* **2020**, 491, 114561.
- [178] C. Li, S. Cao, J. Lutzki, J. Yang, T. Konegger, F. Kleitz, A. Thomas, *J. Am. Chem. Soc.* **2022**, 144, 3083.
- [179] Y. Guo, F. Zhao, X. Zhou, Z. Chen, G. Yu, *Nano Lett.* **2019**, 19, 2530.
- [180] F. Gong, H. Li, W. Wang, J. Huang, D. Xia, J. Liao, M. Wu, D. V. Papavassiliou, *Nano Energy* **2019**, 58, 322.
- [181] Y. Shi, C. Zhang, Y. Wang, Y. Cui, Q. Wang, G. Liu, S. Gao, Y. Yuan, *Desalination* **2021**, 507, 115038.
- [182] Y. Sui, D. Hao, Y. Guo, Z. Cai, B. Xu, *J. Mater. Sci.* **2020**, 55, 298.
- [183] M. Kim, K. Yang, Y. S. Kim, J. C. Won, P. Kang, Y. H. Kim, B. G. Kim, *Carbon* **2020**, 164, 349.
- [184] Z. Li, R. Xu, N. Wei, X. Song, E. Yang, Q. Liu, Y. Sui, H. Cui, *Sol. Energy Mater. Sol. Cells* **2020**, 217, 110593.
- [185] Y. Guo, Y. Sui, J. Zhang, Z. Cai, B. Xu, *J. Mater. Chem. A* **2020**, 8, 25178.
- [186] T. Zhu, Z. He, Y. Ren, W. Zeng, J. Mao, L. Zhu, *Sol. RRL* **2021**, 5, 2100021.
- [187] L. Sun, J. Liu, Y. Zhao, J. Xu, Y. Li, *Carbon* **2019**, 145, 352.
- [188] X. Zhang, G. Wu, X.-C. Yang, *ACS Appl. Nano Mater.* **2020**, 3, 9706.
- [189] Y. Sun, Z. Zhao, G. Zhao, L. Wang, D. Jia, Y. Yang, X. Liu, X. Wang, J. Qiu, *Carbon* **2021**, 179, 337.
- [190] M. Khajevand, S. Azizian, R. Boukherroub, *ACS Appl. Mater. Interfaces* **2021**, 13, 31680.
- [191] Y. L. Wang, G. J. Li, K. C. Chan, *Sol. Energy Mater. Sol. Cells* **2020**, 218, 110693.
- [192] R. Cui, J. Wei, C. Du, S. Sun, C. Zhou, H. Xue, S. Yang, *J. Mater. Chem. A* **2020**, 8, 13311.
- [193] F. Chen, L. Xu, Y. Tian, A. Caratenuto, X. Liu, Y. Zheng, *ACS Appl. Nano Mater.* **2021**, 4, 5230.
- [194] X. Ma, Z. Li, Z. Deng, D. Chen, X. Wang, X. Wan, Z. Fang, X. Peng, *J. Mater. Chem. A* **2021**, 9, 9048.
- [195] Y. Li, M. Zhao, Y. Xu, L. Chen, T. Jiang, W. Jiang, S. Yang, Y. Wang, *J. Mater. Chem. A* **2019**, 7, 26769.
- [196] X. Chen, N. Yang, Y. Wang, H. He, J. Wang, J. Wan, H. Jiang, B. Xu, L. Wang, R. Yu, L. Tong, L. Gu, Q. Xiong, C. Chen, S. Zhang, D. Wang, *Adv. Mater.* **2022**, 34, 2107400.
- [197] H. Zhang, Y. Wang, Y. Liu, M. Zhao, C. Liu, Y. Wang, M. K. Albolqany, N. Wu, M. Wang, L. Yang, B. Liu, *ChemSusChem* **2020**, 13, 2945.
- [198] N. Hu, Y. Xu, Z. Liu, M. Liu, X. Shao, J. Wang, *Carbohydr. Polym.* **2020**, 243, 116480.
- [199] Z. Guo, F. Yu, Z. Chen, Z. Shi, J. Wang, X. Wang, *Sol. Energy Mater. Sol. Cells* **2020**, 217, 110531.
- [200] C. Wen, H. Guo, J. Yang, Q. Li, X. Zhang, X. Sui, M. Cao, L. Zhang, *Chem. Eng. J.* **2021**, 421, 130344.
- [201] V. Mazzone, M. Bonifazi, C. M. Aegerter, A. M. Cruz, A. Fratalocchi, *Adv. Sustainable Syst.* **2021**, 5, 202100217.
- [202] J. Tang, Z. Song, X. Lu, N. Li, L. Yang, T. Sun, Y. Wang, Y. Shao, H. Liu, G. Xue, *Chem. Eng. J.* **2022**, 429, 132089.
- [203] Z. Chen, Y. Lin, Q. Qian, P. Su, Y. Ding, P. D. Tuan, L. Chen, D. Feng, *Desalination* **2022**, 528, 115561.
- [204] C. Kim, D. Shin, M. N. Baitha, Y. Ryu, A. M. Urbas, W. Park, K. Kim, *ACS Appl. Mater. Interfaces* **2021**, 13, 29602.
- [205] Y. Xu, J. Xu, J. Zhang, X. Li, B. Fu, C. Song, W. Shang, P. Tao, T. Deng, *Nano Energy* **2022**, 93, 106882.
- [206] Y. Chen, H. Qiu, X. Li, Q. Tong, M. Jensen, Q. Li, N. Wang, *Appl. Surf. Sci.* **2022**, 582, 152483.
- [207] Y. Li, X.-l. Shi, L.-j. Sun, M. Zhao, T. Jiang, W. Jiang, M. Deng, S. Yang, Y. Wang, *Desalination* **2021**, 515, 115192.
- [208] X. Chen, Z. Wu, D. Lai, M. Zheng, L. Xu, J. Huo, Z. Chen, B. Yuan, M.-L. Fu, *J. Mater. Chem. A* **2020**, 8, 22645.
- [209] S. Hong, Y. Shi, R. Li, C. Zhang, Y. Jin, P. Wang, *ACS Appl. Mater. Interfaces* **2018**, 10, 28517.
- [210] X. Suo, J. Yang, Y. Zhang, Y. Hao, J. Yang, H. Qiao, *Adv. Sustainable Syst.* **2021**, 5, 2100122.
- [211] Y. Bian, Q. Du, K. Tang, Y. Shen, L. Hao, D. Zhou, X. Wang, Z. Xu, H. Zhang, L. Zhao, S. Zhu, J. Ye, H. Lu, Y. Yang, R. Zhang, Y. Zheng, S. Gu, *Adv. Mater. Technol.* **2019**, 4, 1800593.
- [212] X. Wang, Q. Liu, S. Wu, B. Xu, H. Xu, *Adv. Mater.* **2019**, 31, 1807716.
- [213] Q. Lu, W. Shi, H. Yang, X. Wang, *Adv. Mater.* **2020**, 32, 2001544.
- [214] P. Ren, J. Li, X. Zhang, X. Yang, *Mater. Today Energy* **2020**, 18, 100546.
- [215] Y. Yang, Y. Sui, Z. Cai, B. Xu, *Global Challenge* **2019**, 3, 1900004.
- [216] Y. Zhao, K. Zhao, J. Yin, J. Yang, J. Xu, Y. Gu, L. Liu, J. Luo, Y. Li, L. Sun, *J. Mater. Chem. A* **2019**, 7, 24311.
- [217] C. Tian, J. Liu, R. Ruan, X. Tian, X. Lai, L. Xing, Y. Su, W. Huang, Y. Cao, J. Tu, *Small* **2020**, 16, 2000573.
- [218] X. Bai, Y. Li, F. Zhang, Y. Xu, S. Wang, G. Fu, *Environ. Sci.* **2019**, 5, 2041.
- [219] H. Bai, N. Liu, L. Hao, P. He, C. Ma, R. Niu, J. Gong, T. Tang, *Energy Environ. Mater.* **2022**, 5, 1204.
- [220] Y. Li, X. Jin, W. Li, J. Niu, X. Han, X. Yang, W. Wang, T. Lin, Z. Zhu, *Sci. China Mater.* **2022**, 65, 1057.
- [221] S. Lei, D. Huang, S. Liu, M. Chen, R. Ma, M. Zeng, D. Li, W. Ma, L. Wang, Z. Cheng, *J. Mater. Chem. A* **2021**, 9, 15346.
- [222] J. Tang, T. Zheng, Z. Song, Y. Shao, N. Li, K. Jia, Y. Tian, Q. Song, H. Liu, G. Xue, *ACS Appl. Mater. Interfaces* **2020**, 12, 18504.
- [223] E. Chiavazzo, *Nat. Commun.* **2022**, 13, 5813.
- [224] Z. Deng, L. Miao, P.-F. Liu, J. Zhou, P. Wang, Y. Gu, X. Wang, H. Cai, L. Sun, S. Tanemura, *Nano Energy* **2019**, 55, 368.
- [225] S. Jiang, Z. Zhang, T. Zhou, S. Duan, Z. Yang, Y. Ju, C. Jia, X. Lu, F. Chen, *Desalination* **2022**, 531, 115706.



Dan Wei received her Bachelor's degree from the College of Materials Science and Engineering, Shaanxi University of Science and Technology in June 2021. She is currently pursuing a Master's degree under the supervision of Prof. Chengbing Wang at Shaanxi University of Science and Technology. Her current research focuses on the application of solar steam power generation.



Chengbing Wang is a professor at the School of Materials Science and Engineering, Shaanxi University of Science and Technology, China. He obtained his Ph.D. degree from Lanzhou Institute of Chemical Physics of the Chinese Academy of Sciences in 2008. His research interests are in the areas of nanostructured functional materials and their applications in solar steam generation and concentrated solar power.



Xingtao Xu is currently a full professor of Marine Science and Technology College, Zhejiang Ocean University. He received his Bachelor's degree (2012) from Shandong University, and Ph.D. degree (2017) from the East China Normal University. He was awarded a JSPS research fellowship in 2020. In 2023, he moved to Zhejiang Ocean University as a group leader. His research focuses on the synthesis, characterization, and application of nanoporous materials for energy-water nexus applications.



Yusuke Yamauchi received his Bachelor degree (2003), Master degree (2004), and Ph.D. degree (2007) from Waseda University, Japan. Then, he joined NIMS to start his own research group, and moved from NIMS to Nagoya University since April of 2023. In 2016, he joined the University of Wollongong as a full professor. He is currently a full professor at the School of Chemical Engineering and Australian Institute for Bioengineering and Nanotechnology, The University of Queensland, Australia. He concurrently serves as a distinguished full professor of Nagoya University, a visiting professor at several universities.